Copepod Response Behavior in Turbulence

A Thesis
SUBMITTED TO THE FACULTY OF THE
UNIVERSITY OF MINNESOTA
BY

Daniel Krizan

IN PARTIAL FULFILLMENT OF THE REQUIREMENTS
FOR THE DEGREE OF
MASTER OF SCIENCE

Ellen Longmire, Adviser

September 2014

Acknowledgements

Working on this thesis been a very rewarding experience and would not have been possible without the help of many people. First, I would like to thank my advisor Dr. Ellen Longmire. She was extremely helpful throughout every point along the research. I have learned so much about the scientific research process through her teachings. She gave me great insight in problem solving and always helped me strive for the best results possible. I would like to thank Dr. Filippo Coletti and Dr. Miki Hondzo for serving on my committee. I would like to thank Dr. Zhengzhong Sun for everything he taught me and all of his help with setup of tomographic PIV and data processing. I would like Dr. Deepak Adhikari for all of his help setting up experiments and giving such great insight with many aspects throughout the project. I would also like to thank all lab mates for helping whenever needed, having insightful discussions, and the camaraderie: Alonso Alvarado, Ankur Bordoloi, Jeshwanth Kundem, Yan Ming Tan, Michael Voller, and Kyle Winters. Finally, I would like to thank my parents for the inspiration and support. I would not be where I am today without them. Also, the author acknowledges funding from the National Science Foundation – IDBR Grant No #0852875.

Dedication

To my parents and sister for all of their love and support over the years

Abstract

The objective of this thesis is to determine copepod response to turbulence generated by obstacles in cross flow. Mainly, flow and copepod response downstream a square fractal grid is examined but experiments downstream a cylinder provides comparison. This is done by simultaneously measuring the copepods position and velocity using 3D-PTV in a measurement volume and measuring the two dimensional three component velocity vectors of the flow using stereo PIV. These measurements are done in a way that does not elicit copepod response. Tomographic PIV is done downstream the square fractal grid without copepods to gain volumetric velocity knowledge of the flow in the measurement volume.

Copepods are known to execute sudden high speed jumps (or escapes) in response to sensed hydrodynamic signals. The fractal grid was shown to elicit copepod escape, specifically directly downstream with escape frequency decreasing further downstream where turbulence levels were much lower. It was found that at a slower freestream speed copepods exhibited jumps not in reaction to flow disturbances but to reorient themselves (cruise swimming). There was almost no copepod response in the wake of a cylinder, but copepods again exhibited cruise swimming behavior at a slower freestream speed. In regions with high maximum principal strain rate (MPSR) downstream of the fractal grid, copepods were observed to exhibit multiple escapes. Moreover, copepods were observed to jump towards regions of lower turbulence and against the freestream direction. From stereo PIV, instantaneous 2D MPSR values of less than $3s^{-1}$ were shown to create escape in 60% of copepod escapes analyzed. Finally, it was found that on average larger MPSR resulted in larger jumps from copepods.

Table of Contents

List of Tables

List of Figures

Nomenclature

Abbreviations

MPSR	maximum principal strain
PIV	particle image velocimetry
PPIV	planar particle image velocimetry
PTV	particle tracking velocimetry
SPIV	stereo particle image velocimetry
TPIV	tomographic particle image velocimetry

Greek Symbols

α	change in copepod trajectory from dot product angle
α'	change in copepod trajectory from dot product angle with averaging
β	camera angle to the spanwise direction
δt	time between cross correlated frames
Δt	time between measurements for independent samples
δu	bias uncertainty of velocity measurement
δ_{99}	overall boundary layer thickness
θ	copepod wall-normal and spanwise position change angle
ν	kinematic viscosity of fluid
ρ	density of fluid
$\sigma_{\Delta x}$	displacement uncertainty
ϕ	copepod wall-normal position change angle
ψ	copepod spanwise position change angle
ω	local vorticity
$\mathbf{\Omega}$	Anti-symmetric rotation tensor

Roman Symbols

a	distance from flow obstacle to center of measurement volume
d_c	cylinder diameter
d_i	bar thickness of i iteration in square fractal grid
D_i	dimension of non-overlapping interrogation domain
dx	streamwise change in copepod trajectory

dy	wall-normal change in copepod trajectory
dz	spanwise change in copepod trajectory
$\boldsymbol{D}$	symmetric deformation tensor
h	height measured from bottom of water channel
i	bar iteration in square fractal grid
L_i	bar length of i iteration in square fractal grid
M	magnification of measurement
MT	momentum thickness of boundary layer
n	current time step
p	forward time step number
Re	Reynolds number
t	time
TI	turbulence intensity
u	local instantaneous streamwise velocity
U	local mean streamwise velocity
u_{rms}	local average of root mean square streamwise velocity fluctuation
u_c	copepod streamwise velocity
u_{diff}	copepod streamwise velocity difference to mean
U_0	freestream velocity
v	local instantaneous wall-normal velocity
v_c	copepod wall-normal velocity
$\left\|\overrightarrow{v_{c,slip}}\right\|$	copepod slip velocity magnitude calculated from mean flow
V	local mean wall-normal velocity
v_{rms}	local average of root mean square wall-normal velocity fluctuation
v_{diff}	copepod velocity magnitude difference between time steps
$\overrightarrow{v_c}$	instantaneous copepod velocity vector
w	local instantaneous spanwise velocity
w_c	copepod spanwise velocity
W	local mean spanwise velocity

w_{rms}	local average of root mean square spanwise velocity fluctuation
x	streamwise direction
y	wall-normal direction
z	spanwise direction
X	horizontal image direction
Y	vertical image direction

Chapter 1: Introduction

1.1. Motivation

There are three important components to the aquatic ecosystem, as is seen in Figure 1-1. On the lowest level are phytoplankton, which are photosynthesizing micro-organisms that are the primary carbon producers. Zooplankton at the second level of this food chain, feed on phytoplankton. The root 'plankton' refers to an organism that drifts with the flow. Phytoplankton and zooplankton both drift with currents and are found abundantly in freshwater and saltwater. Fish, whales and other larger organisms feed on zooplankton, which makes zooplankton a key organism in aquatic ecosystems.

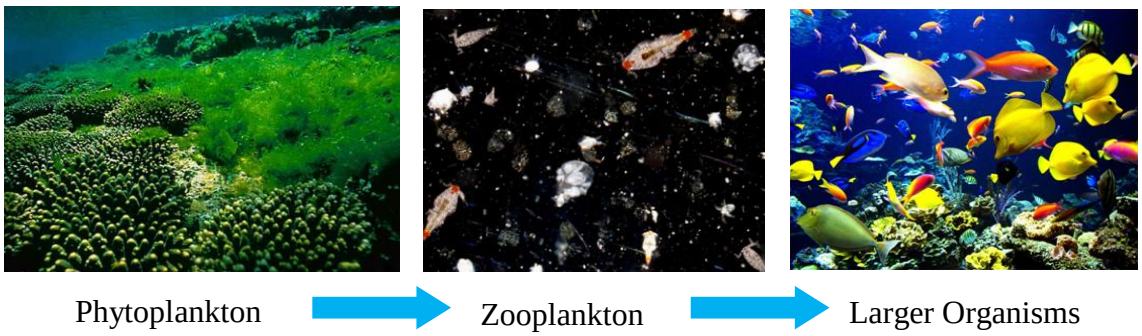

Figure 1-1: Food chain of typical aquatic ecosystem

Copepods are a type of zooplankton that belong to the phylum called crustaceans, which mean they have an exoskeleton that is molted during growth. Copepods are considered to be one of the most numerous multicellular organisms on earth. Copepods also represent a large portion of plankton collected in regions varying from the Antarctic Oceans to freshwater lakes (Mauchline 1998). A calanoid copepod, thought to be one of the most abundant zooplankton, is shown in Figure 1-2. This species is called *Calanoida Diaptomus*, which are found in freshwater lakes and are the species investigated in this study. These copepods have an oval shaped body, usually 0.5-2mm long, with two antennae extending in the lateral direction off the head. These antennae have smaller setae, small hair like receptors, that can detect small flow disturbances (Yen and Fields 1992). Copepods also have swimming legs on their body that can be deflected rapidly,

which results in a sudden high speed 'jump' like motion. Using the setae to detect flow disturbances, copepods can detect when predators are near and escape rapidly through locomotion of their swimming legs (Lenz and Yen 1993).

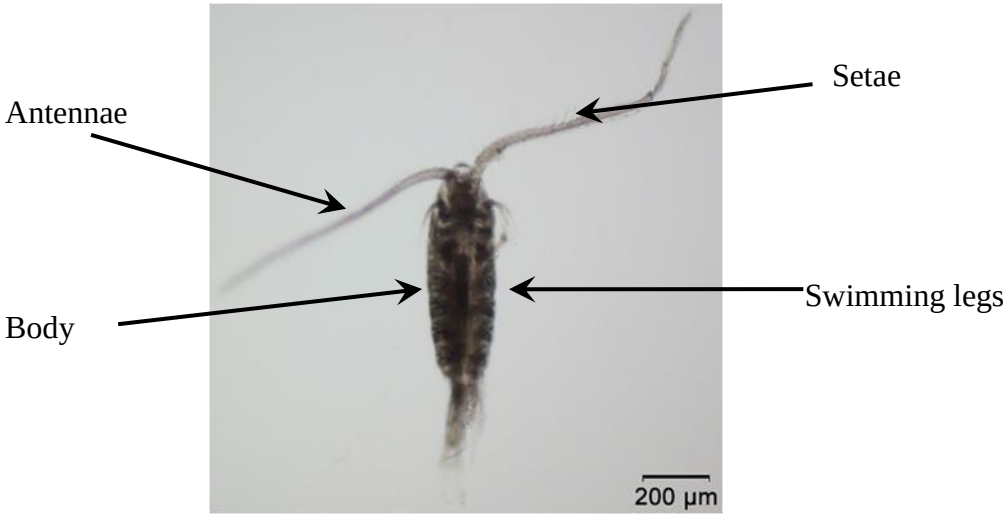

Figure 1-2: Image of Copepod (Calanoida Diaptomus). Reproduced from cfb.unh.edu

These high speed, accelerated escapes are performed by copepods in response to stimulus detected in the setae from turbulent flow. When copepods are in a turbulent environment they have increased interaction with phytoplankton, so their food intake increases. However, when copepods are consistently in higher turbulent regions they tend to have repeated escape responses demanding more energy. This can lead to a decline in the total population growth of the species (Mauchline 1998). Understanding what causes these responses in copepods is an important aspect of the aquatic ecosystem, as it not only affects the success rate of the large organism consuming the copepod but also affects the eating habits of the copepod on phytoplankton. Therefore, the motivation of this study is to determine copepod response due to the turbulent flow it perceives.

1.2. Previous work

1.2.1. Copepod scaling

To better understand the behavior of the copepod in turbulence, the scaling of the copepod relative to its surroundings must be examined. Copepods, approximately 1mm in body length, have predators such as fish and whale sharks, which can be on the order of 10cm to 10m, respectively. This large size difference seen by the copepod is accounted for by their ability to execute very fast intermittent swims or jumps to escape the predator. The copepod has two swimming regimes. The first occurs in still water during feeding, which is called cruise (~1 mm/s). The second is the previously mentioned jump (~50 cm/s). This large difference in swimming speeds the copepod executes means there is a large range in fluid forces the copepod sees. In fluid mechanics, a simple dimensionless quantity to scale inertial to viscous forces is known as Reynolds number (Re). For this application, Reynolds number is defined as $Re = UL/\nu$, where U is the flow relative to the organism, L is the length of the organism, and ν is the kinematic viscosity of the fluid. The copepod sees a large range in fluid velocities (1-500mm/s) which means the Reynolds numbers it sees are 1-500. This means the flow around the copepod can be strongly affected by viscosity (Re~1) or dominated by inertia (Re>100) (Yen 2000). A small fish that feeds on copepods can have Re up to 10^4, which means fluid motion around the fish will be dominated by inertial forces. This scaling is important in understanding what the copepod senses and how it escapes.

1.2.2. Copepod sensing

In order to execute their quick escapes, copepods must be able to sense hydrodynamic signals precisely. Copepods can sense these signals through the setae which are attached to the antennae. These hydrodynamic signals detected are from the fluid velocity and velocity gradients. It has been found that a copepod's orientation does not necessarily align with a given coordinate system (Catton et al. 2012). Therefore,

when quantifying the hydrodynamic signals perceived by the copepod, it is important to use quantities that are independent of a given coordinate system. A quantity commonly used is the maximum principal strain rate or MPSR. MPSR is useful for this application because it is determined from spatial gradients of the velocity components and does not have a directional preference. MPSR is calculated by finding the eigenvalues of the symmetric portion of the deformation rate tensor, which is

$$\boldsymbol{D}_{ij} = \begin{bmatrix} \frac{\partial u}{\partial x} & \frac{1}{2}\left(\frac{\partial u}{\partial y} + \frac{\partial v}{\partial x}\right) & \frac{1}{2}\left(\frac{\partial u}{\partial z} + \frac{\partial w}{\partial x}\right) \\ \frac{1}{2}\left(\frac{\partial u}{\partial y} + \frac{\partial v}{\partial x}\right) & \frac{\partial v}{\partial y} & \frac{1}{2}\left(\frac{\partial v}{\partial z} + \frac{\partial w}{\partial y}\right) \\ \frac{1}{2}\left(\frac{\partial u}{\partial z} + \frac{\partial w}{\partial x}\right) & \frac{1}{2}\left(\frac{\partial v}{\partial z} + \frac{\partial w}{\partial y}\right) & \frac{\partial w}{\partial z} \end{bmatrix}, \tag{1-1}$$

where u, v, and w are velocity components in the x, y, and z directions, respectively. The eigenvalues, λ_k (k=1,2,3), are then determined by

$$\det\left(\boldsymbol{D}_{ij} - \lambda_k \delta_{ij}\right) = 0, \tag{1-2}$$

where det refers to the determinant of a tensor and δ_{ij} is the Kronecker delta tensor. Finally, the maximum principal strain rate is found by $MPSR = \max(|\lambda_1|, |\lambda_2|, |\lambda_3|)$.

Another quantity that is comprised of spatial gradients of the velocity components and is invariant of a coordinate system is vorticity. Vorticity comes from the anti-symmetric rotation tensor, $\boldsymbol{\Omega}$, which is

$$\boldsymbol{\Omega} = \frac{1}{2}(\nabla \boldsymbol{u} - (\nabla \boldsymbol{u})^T) = \begin{bmatrix} 0 & \frac{1}{2}\left(\frac{\partial u}{\partial y} - \frac{\partial v}{\partial x}\right) & \frac{1}{2}\left(\frac{\partial u}{\partial z} - \frac{\partial w}{\partial x}\right) \\ \frac{1}{2}\left(\frac{\partial v}{\partial x} - \frac{\partial u}{\partial y}\right) & 0 & \frac{1}{2}\left(\frac{\partial v}{\partial z} - \frac{\partial w}{\partial y}\right) \\ \frac{1}{2}\left(\frac{\partial w}{\partial x} - \frac{\partial u}{\partial z}\right) & \frac{1}{2}\left(\frac{\partial w}{\partial y} - \frac{\partial v}{\partial z}\right) & 0 \end{bmatrix} = \frac{1}{2}\begin{bmatrix} 0 & -\omega_z & \omega_y \\ \omega_z & 0 & -\omega_x \\ -\omega_y & \omega_x & 0 \end{bmatrix}, \tag{1-3}$$

where ω_x, ω_y, and ω_z are the x, y, and z components of vorticity, respectfully. The vorticity magnitude is

$$\|\omega\| = \sqrt{\omega_x^2 + \omega_y^2 + \omega_z^2}. \tag{1-4}$$

Researchers have performed a variety of experiments to determine thresholds of the hydrodynamic signals required to elicit escape in copepods. To compare with the copepods used in this study, only copepods of similar size and those in the *Calanoida*

family will be discussed. Murphy (2012) provides tabulated results summarizing previous experiments where thresholds for copepod escape were measured or estimated. In Fields and Yen (1996 & 1997), a siphon tube experiment was performed to simulate feeding from a predator, and escape thresholds of MPSR values were measured as 1.5 - $9.7s^{-1}$. These strain rate values were calculated from averaging results of two perpendicular 2D Particle Tracking Velocimetry (2D-PTV) measurement systems of neutrally buoyant *Artemia* eggs. The recorded escape thresholds were the averaged strain rates at the given escape location. Kiørboe *et al*. (1999) performed multiple experiments with different laminar flow geometries in which they were able to examine the effect of MPSR and vorticity on copepod escape. They found MPSR thresholds of $0.5 – 5s^{-1}$, which were determined from model flow equations for the given experiment. They found that vorticity did not introduce escape response even when vorticity values were greater than the above strain rate thresholds. Viitasalo *et al.* (2001) found threshold strain rates of $3.9 – 10.4s^{-1}$ from a siphon tube experiment. Measurements by Viitasalo *et al.* (2001) were performed in the same way as Field and Yen (1996 & 1997) but neutrally buoyant phytoplankton were used as the tracer particles. Buskey *et al.* (2002) reported MPSR values of $0.4 – 12s^{-1}$ from a vibrating cylinder experiment with high speed video recording. These instantaneous values were calculated from model flow equations based on instantaneous speed and distance from the vibrating cylinder.

Most recently, Adhikari (2013) conducted experiments using volumetric measurements of copepods and predatory fish in still water and turbulent flow, which found that copepods respond to a sudden increase in MPSR rather than a given threshold. The instantaneous MPSR threshold values found were $0.4 - 5s^{-1}$, and it was found that generally copepods did not respond to vorticity. It was also found that copepods rarely responded in the wake of a cylinder in cross flow. Researchers have found that velocity gradients and MPSR result in jump behavior, but the flow conditions studied and measurement techniques used have been limited.

1.2.3. Copepod locomotion

After copepods detect velocity gradients, they execute a sudden high-speed jump. This jump is done in an attempt to escape the predator (Jiang and Kiørboe 2011). During the jump, the copepod will oar its swimming legs very quickly and bring the antennae towards its body. The copepod may carry out multiple oar strokes to move a larger distance (Yen 2000). The time of a given jump is typically 10 – 30ms (Buskey 2002). Researchers have also documented copepod escape speeds for different flows. Viitasalo *et al*. (2001) found escape speeds of 0.04m/s from a siphon tube experiment with video measurement. By contrast, Buskey *et al*. (2002) found escape speeds around 0.4m/s from high-speed video measurement. Similarly, through multiple experiments Kiørboe *et al.* (2010) found an escape speed of 0.378m/s and Jiang and Kiørboe (2011) found an escape speed of 0.333m/s. Both experiments used high-speed digital video measurement. These high-speed jumps make the copepod move from a viscous-dominated regime to an inertia-dominated regime as previously discussed. Although escape speeds have been measured previously, there has not been investigation into the direction of the escape based on the surrounding flow.

1.2.4. Turbulence generated from square fractal grid

In order to investigate escape response by copepods, turbulence must be introduced into the measurement volume, which can be achieved by putting obstacles into cross flow. To have a range of turbulence levels and scales, the obstacle used must generate sustained turbulence. Therefore, a square fractal grid was selected because of the complex wake it introduced. Figure 1-3 shows a square fractal grid with four iterations. For this discussion, it is important to introduce a quantity called turbulence intensity, which measures turbulence and is independent of given coordinate system. This quantity is defined as

$$TI = \frac{\sqrt{\frac{1}{3}\left(u_{rms}^2+v_{rms}^2+w_{rms}^2\right)}}{\sqrt{U^2+V^2+W^2}}, \tag{1-5}$$

where U, V, and W are the local mean velocities and u_{rms}, v_{rms}, and w_{rms} are the local averages of the root mean square velocity fluctuations in the x, y, and z directions, respectively.

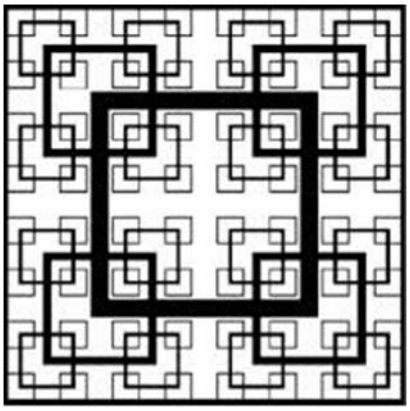

Figure 1-3: Square fractal grid with four iterations

Previous studies on flow behind square fractal grids of different geometries and number of iterations have been performed. A Direct Numerical Simulation (DNS) study was performed by Laizet and Vassilicos (2011), which investigated the evolving turbulent flows generated from a uniform square grid compared to three different geometries of square fractal grids with three iterations. From visualization, the vorticity generated from a square fractal grid is more intermittent and clustered than for a regular grid at the same or even lower blockage ratio. Regular grids can generate high turbulence intensities but only over a short region very close to the grid. However, further downstream fractal grids generate higher vorticity and turbulence intensities than regular grids. Fractal grids have also been found to hold clear geometrical imprints of the grid far downstream. The turbulence generated from a fractal grid is found to have two regions. The first being the production region, which is closer to the grid. Here, turbulence amplifies as downstream distance from the grid increases. The maximum turbulence intensity of streamwise direction, $\sqrt{u_{rms}^2}/U_0$, in the centerline was about 25%. In the near wake of the thickest beam, the turbulence intensity for the streamwise component is found to be greater than 40%. In the second region, the turbulence

progressively decays with increasing distance downstream of the grid. In the production region, the turbulence is generated at the smallest scales near the grid where the smaller wakes are more dominant. Further downstream, this turbulence interacts with the turbulence generated from larger wakes to produce larger scale turbulence.

A PIV study investigating turbulence generated from a square fractal grid with four iterations was performed by Gomes-Fernandes et al. (2012). In this study, the flow facility had non-negligible incoming freestream turbulence, which was found to cause higher rate of growth in the wakes downstream. This two dimensional and two component study was focused on the center plane of the grid. It confirmed the results of Laizet and Vassilicos (2011) of two turbulent regions. These studies show that square fractal grids can generate a range of turbulence that can be used to elicit escape response in copepods.

1.3. Research objectives

The main objective of this thesis is to determine copepod response to turbulence generated by obstacles in cross flow. Specifically, copepod escape frequency, escape direction, and turbulence levels in flow will be investigated. This is done using a controlled, recirculating water channel that propels water in a way that is not detrimental to copepod health. It is required that simultaneous measurements of copepods and flow are done in a way that does not disturb copepod response. This implies careful consideration of each component of the measurement techniques used. A motion tracking velocimetry system must be used to measure the time resolved copepod position during experiments. In this study, three dimensional particle tracking velocimetry (3D-PTV) will be used to track the three dimensional copepod position within the measurement volume along with three dimensional velocity vectors of the copepods. This will give accurate measurement of the copepod in highly complex flows. Also, a measurement system to accurately capture the time resolved velocity and velocity gradients of the flow is needed. In this study, different methods of PIV will be used. These include planar PIV (PPIV), stereo PIV (SPIV), and tomographic PIV (TPIV). SPIV will give two dimensional three component velocity vectors and TPIV will give

three dimensional three component velocity vectors. From both methods, spatial velocity gradients can be found that are necessary to resolve strain rate thresholds for copepod escape.

Chapter 2: Experimental Methodologies

2.1. Experimental design

In this study, all of the experiments were carried out in a closed return water channel at the University of Minnesota. In this section, the major design considerations of the water channel and the geometry of the fractal grid used will be discussed.

2.1.1. Water channel design

A schematic of the water channel used for this study is found in Figure 2-1. Flow is driven by a paddlewheel made of PVC in order to not harm or kill the copepods. The paddlewheel is driven by an electric motor that is connected by a belt. The electric motor has a controller in which the revolutions per minute (RPM) can be set. The straight sections of the channel are made of acrylic, which is beneficial in providing optical access for the measurement system in the test section. The corner sections are made of stainless steel and have three acrylic guide vanes to help turn the flow. The channel has a constant width of 0.15m and water in the channel was always filled to 0.15m. Foam gaskets were placed between the corners and straight sections. After the connections were secured, a thin layer of marine-grade silicone sealant was placed inside the channel to prevent any leaking. The entire channel and paddlewheel is supported with steel Unistrut, which gives a desirable working height of the channel. The support system used gave the ability to mount components of the measurement systems on both sides of the channel. Screens and honeycomb were placed directly after the final corner before the test section. The test section was designed to be far enough downstream (1.25m) of the screens and honeycomb to have copepods unaffected. Honeycomb was also placed further downstream of the test section and closer to the paddlewheel to ensure waves from the paddlewheel were not propagated upstream. This channel was designed by Deepak Adhikari and a more in depth design discussion can be found in Adhikari 2013.

From Figure 2-1 and for the rest of this study, x, y, and z are the streamwise, wall-normal, and spanwise directions, respectively. A picture of the completed water channel with measurement system is seen in Figure 2-2.

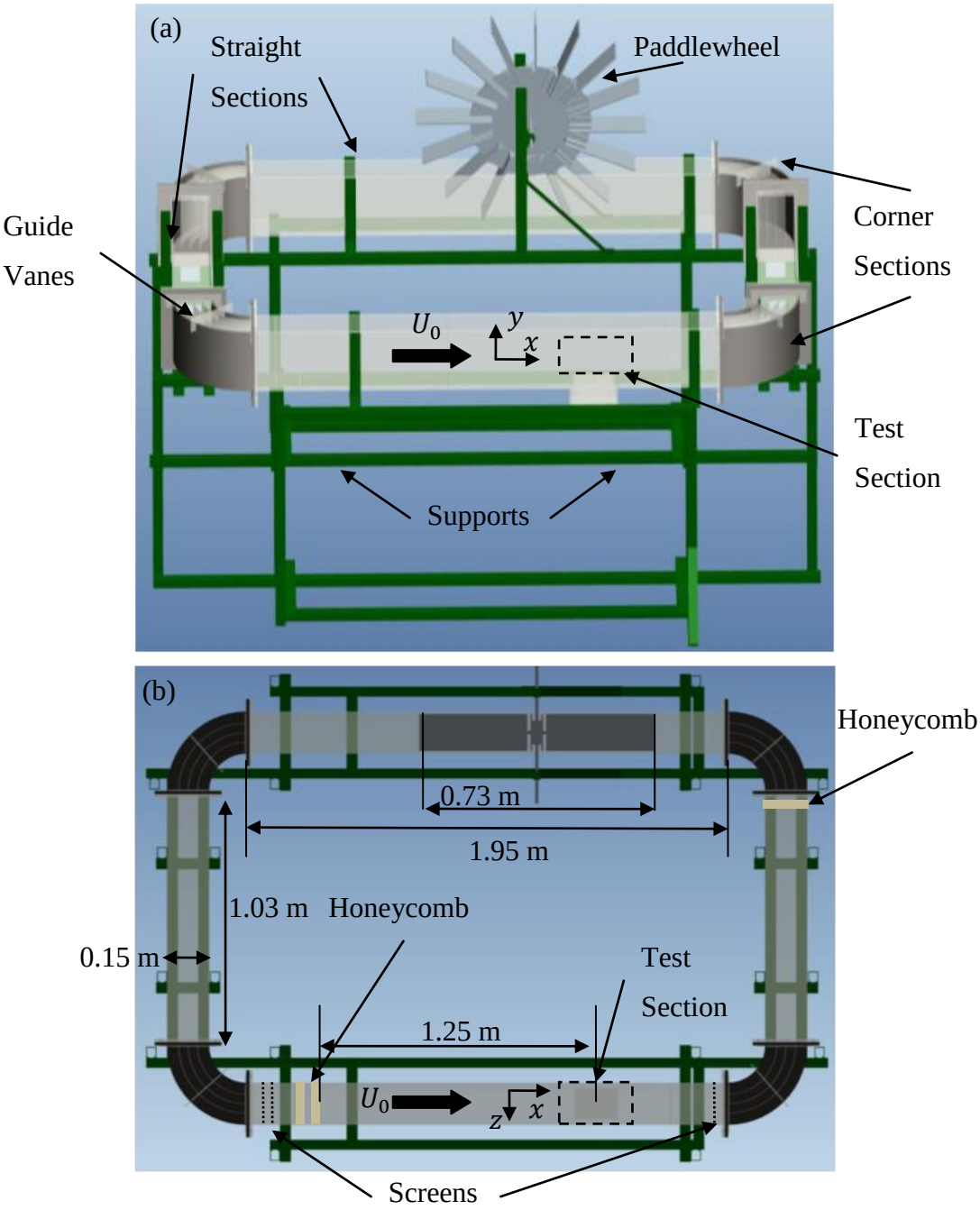

Figure 2-1: Diagram of water channel with side view (a) and top view (b). Credit: Deepak Adhikari

Figure 2-2: Picture of full setup with cameras and laser

2.1.2. Fractal grid design

A schematic of the fractal grid used can be found in Figure 2-3 where the iteration number of each thickness is labeled. The larger the iteration, i, the thinner the bar is. The thickness of each bar, d_i, is given in Table 2-1. In Table 2-1, the length of each iteration, L_i, is the side length of the square centerline to centerline. The grid was designed to have a blockage ratio of 25%. The chord length thickness of the grid is 0.0042m. The fractal grid was fabricated at the research shop in the Mechanical Engineering Department at the University of Minnesota. The fabrication was done by taking a sheet of acrylic 0.0042m thick and removing material to the desired dimensions with a laser cutter. The selected geometry is based off of the SFG8 geometry used in Gomes-Fernandes *et al.* 2012, but modified because of cutting limitations of the laser cutter. The final dimensions of the grid used are found in Table 2-1.

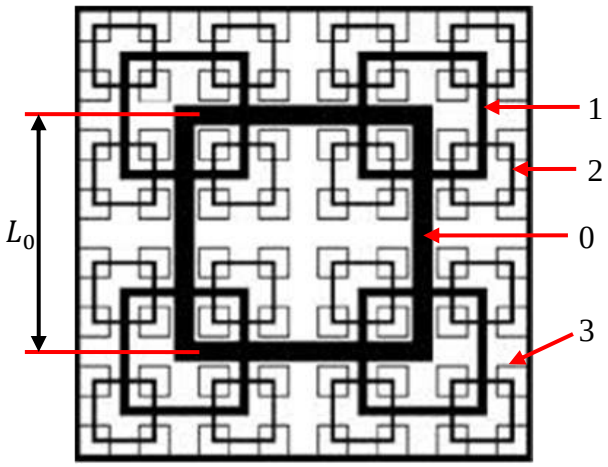

Figure 2-3: Schematic of fractal grid showing iteration number

Table 2-1: Dimension specifications of fractal grid

i	L_i (m)	d_i (m)
0	0.07493	0.004445
1	0.03734	0.002286
2	0.01867	0.001143
3	0.00914	0.000635

2.2. Experimental measurement hardware specifications

Careful considerations of the components for the measurement system must be taken. The measurement system must not affect the natural response behavior or health of the copepods. The measurement system must also be high-speed to capture the copepods sudden jumps and give time resolved fluid vectors.

2.2.1. Laser

There are several considerations to take into account for the laser used to illuminate a measurement volume for the various PIV techniques used. The wavelength of the laser must be invisible to the copepods so behavioral response is to the flow instead of the laser pulse. The laser must be high-powered for proper illumination of the tracer

particles in the measurement volume, especially for TPIV. The laser must be able to have high pulse frequency to resolve the copepod motion.

These parameters can be satisfied by using a near-infrared laser with a wavelength of 808nm. Specifically, an Oxford Laser Firefly 300W laser was used. This wavelength of laser has been shown to prevent unnatural response in the copepod while operating within the range of CMOS cameras (Murphy *et al.* 2012). This laser can emit a pulse frequency up to 10kHz with 1% duty cycle. Another consideration of using a near-infrared laser is that, as compared to visible wavelength illumination, the near-infrared has an increased absorption of the illumination by water. Therefore, the laser must have enough power to overcome this increased absorption, which was satisfied by the Oxford Laser Firefly 300W. Also, the laser must be used with special eye protection because it can damage the human eye with direct exposure. Near-infrared is not visible to the human eye, so special equipment was used to check the location of laser illumination. Another advantage of the Oxford Laser Firefly 300W is the built in optics of the laser head which allowed the illuminated region to be fanned over a volume. However, a cylindrical lens with a focal length of 50.8mm was placed in front of the laser output to evenly distribute illumination in the volume for TPIV.

2.2.2. Cameras

The cameras used must be able to capture the copepod motion and resolve the illuminated tracer particles. Copepods were illuminated with visible light and tracer particles with the near-infrared laser, therefore the cameras must have a high bit-depth for the sensor as they need to capture a broad range of intensity values. The cameras must also have high sensitivity to each spectrum in order to obtain a high signal to noise ratio. In addition, the cameras must be able to capture at high frame-rates to resolve high-speed motion of the copepods.

Six high-speed cameras from Vision Research Inc. were used throughout the various experiments, four Phantom v210 and two Phantom M110. Both types of cameras had 1200 x 800 pixel resolution, 20μm pixels, and 12-bit monochrome CMOS sensors.

At full resolution, the Phantom v210 used can capture at 2190fps and has 8GB of high-speed internal RAM. However, the Phantom M110 used can capture at 1630fps and has 6GB of high-speed internal RAM at full resolution. Both cameras were found to have high signal to noise ratios for both the near-infrared and visible spectrums.

2.2.3. Tracer particles

Tracer particles are illuminated by the laser and used to get fluid velocity vectors from PIV. For the experiments with copepods, the particles must be nontoxic to the copepods. For the experiments with and without copepods, the particles must be neutrally buoyant, effectively scatter near-infrared wavelength from the laser, and must have ideal scatter size for TPIV (Adrian & Westerweel 2011).

For the experiments with copepods, 55μm polyamide (with 11% titanium dioxide) particles were chosen because they are nontoxic to copepods and scatter near-infrared effectively. These particles were also used for TPIV experiments as they were found to have ideal scatter size. For SPIV experiments without copepods, silver coated hollow glass spheres with an average diameter of 13μm were used. These particles were found to not clump together after performing multiple experiments as was sometimes the case for the polyamide particles. Also, the silver coated particles had an image size of 3x3-5x5pixels, where the polyamide particles were larger. However, both particles were found to give good results as will be discussed later.

2.3. Experiments with copepods

All of the experiments involving copepods will be discussed in this section, which include freestream flow, downstream of the square fractal grid, and downstream of a horizontal cylinder. Specifically, the details of copepod collection, set up of the measurement system in the water channel, experimental methodology, error of 3D-PTV measurement system, and image processing methodology for 3D-PTV data will be discussed.

2.3.1. Collection methodology

All of the copepods used in this study were collected at Lake Calhoun, Minneapolis, MN (44°56'53.2"N, 93°18'56.3"W). Populations of copepods were found to be largest at night (9-10pm) or in the morning (7-8am). Collection was done using a 0.25m diameter plankton net with a mesh size of 150μm, which was dragged across the water surface alongside a dock for approximately ten minutes with the entire 0.25m diameter opening in the water. The collected copepods were put into a bucket with approximately10 liters of lake water before being transported back to the laboratory. For a typical collection, four buckets were filled using this method. Upon arrival at the laboratory, aerators were placed into the water of the collected copepods and used for experiments within 24 hours of collection.

To isolate copepods for experiments, the aerators were removed. In still water, a point source white LED light was placed on the side of the bucket. The copepods would swim towards the point source quicker than other collected species (*Daphnia, Leptodora Kindtii*, etc.) and were then scooped with a small beaker (~20mL) to be put into a larger beaker. In an attempt to remove algae and other unwanted species, the contents of the beaker were poured through a 1000μm mesh filter and then placed into the water channel. However, some algae and *Daphnia* were placed into the water channel. To avoid this affecting measurement results in the 3D-PTV system, image processing was performed which will be discussed in section 2.3.5.

2.3.2. Experimental setup

For all experiments with copepods, simultaneous time resolved measurements were performed of SPIV at the center plane of the channel and 3D-PTV to track copepods within a volume. A schematic of the set up can be found in Figure 2-4. The four Phantom v210 cameras with 105mm Nikon Micro-Nikkor lens were used with the f-stop set to *f*/11. All cameras had Scheimpflug adapters mounted to the camera with the

lens attached in order to adjust the plane of focus. All four cameras were tilted approximately 20° to the spanwise direction as seen from Figure 2-4 (b) and parallel to the bottom of the channel. The two PIV cameras have optical filters on the end of the lens to allow illumination from the near-infrared laser sheet to pass. The laser was mounted directly above the measurement volume and the internal optics was adjusted to give a thin sheet (~1mm thick) in the center of the channel. The resulting field of view for SPIV was 6.3cm by 3.9cm in the x and y directions, respectively. The bottom of the field of view was 2.4cm above the bottom of the channel. Copepods were illuminated from two LED lamps (Philips LED 120W lamps) placed on the opposite side of the channel as the measurement cameras with optical filters that only allowed visible illumination to pass. Optimal copepod illumination was found when the lights were placed behind and above the measurement volume as seen from the PTV cameras. The resulting measurement volume for 3D-PTV was 6.4cm by 3.8cm by 2.5cm for x, y, and z, respectively and located 2.4cm above the floor of the channel.

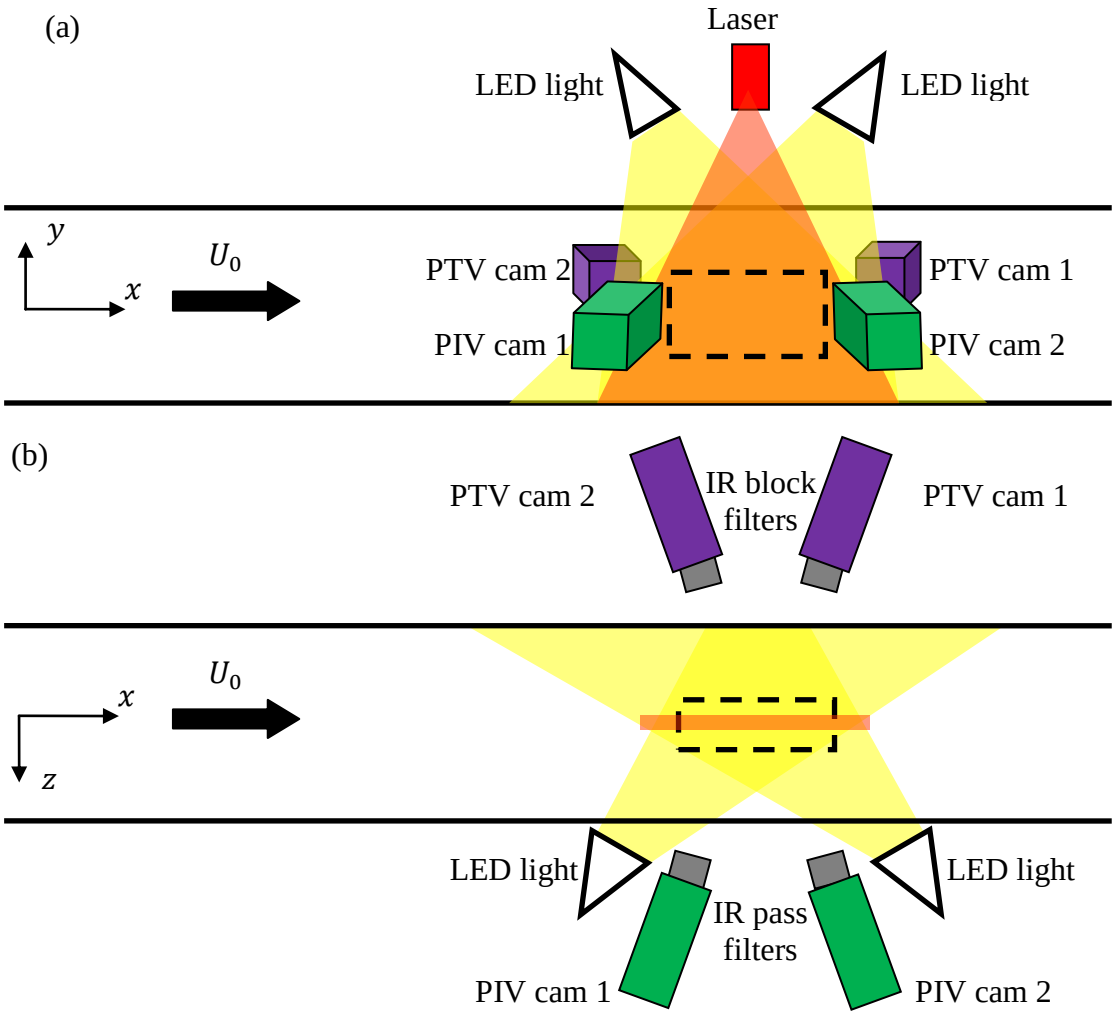

Figure 2-4: Schematic of (a) front and (b) top view of stereo PIV and 3D-PTV measurement systems. The dashed box is the measurement volume. The red area is the infrared illuminated area from the laser, while the yellow area is visible light from LEDs

2.3.3. Experimental procedure

For all experiments with copepods, the channel was filled and then calibration was performed. First, tap water was filled to a height of 0.15m in the channel. While water was filling, 35mL of Aqueon Water Conditioner was mixed into the channel, which made the tap water safe for copepods. The channel was then filled with 55μm polyamide particles by first placing 5-10mL of particles into a smaller container with some water from the channel. The small container was shaken for about a minute before evenly

distributing the particles throughout the channel which reduced clumping of the particles. This was repeated several times until the proper seeding density was reached. Then a LaVision 058-5 double sided stepped calibration plate connected to a traverse was mounted into the channel. For SPIV calibration, one side of the stepped plate was straddled over the laser sheet. For 3D-PTV calibration, the plate was traversed spanwise evenly across eleven locations in the measurement volume. Copepods collected as described in section 2.3.1 were then evenly distributed throughout the channel and experiments were ready to be performed. For all experiments involving copepods, data was collected sequentially in time series with all four cameras having the same simultaneous exposure with a single laser pulse during exposure.

2.3.3.1.Downstream fractal grid

A schematic of the grid location in relation to the measurement volume is shown in Figure 2-5. The distance of the grid to the center of the measurement volume, a, is varied to test copepod response to different turbulence generated by the grid. Experiments were performed at 1RPM and 3RPM settings on the paddlewheel. For experiments at a of 0.12m and smaller, the time between laser pulses, δt, was 0.008s and 0.002667s for 1RPM and 3RPM, respectively. For experiments at a of 0.2m and larger, δt was 0.008696s and 0.002899s for 1RPM and 3RPM, respectively. These times were selected to give an 8-10pixel displacement in the streamwise direction. This was desired as 32x32 pixel cross correlation with a 50% overlap was performed in LaVision's DaVis 8.0 for SPIV. Before vector fields were computed, the average background intensity was subtracted to eliminate background noise. This resulted in a plane of 83x51 three component velocity vectors with a spatial resolution of 1.52mm per vector (32x32 pixels). Some experiments for a at 0.055m were also performed at a δt of 0.001s for 1RPM and 3RPM to resolve copepod acceleration during escape. To increase accuracy of computed PIV vectors, correlations were performed with δt of 0.003s and 0.008s for 1RPM and 3RPM, respectively. 3D-PTV vector calculations with image processing were also performed in LaVision's DaVis 8.0 but the details will be discussed in section 2.3.5.

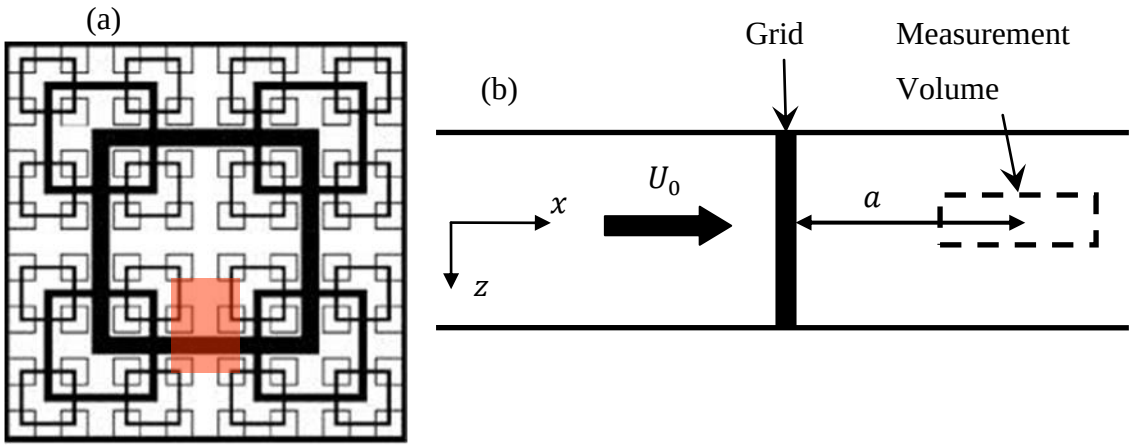

Figure 2-5: In (a), fractal grid with red area showing section of grid upstream of measurement volume. Schematic of grid location to measurement volume in (b)

2.3.3.2.Downstream horizontal cylinder

A schematic of the horizontal cylinder location in relation to the measurement volume is shown in Figure 2-6. The diameter of the cylinder, d_c, was 0.003175m and was chosen because its diameter is similar to the thickness of the thickest beam of the fractal grid. The cylinder was mounted across the entire width of the channel with mounting clay at a height, h, of 0.037m above the bottom of the channel. This was to match the location of the thickest beam of the fractal grid for the same measurement volume as the fractal grid. a was 0.055m and was not varied. The paddlewheel was set to 1RPM and 3RPM. Image processing and vector computation for SPIV was performed with the same method as for downstream of the fractal grid with the same vector spatial resolution. For all experiments, δt was 0.001s where correlations for PIV were performed with δt of 0.003s and 0.008s for 1RPM and 3RPM, respectively. Again, details of 3D-PTV processing methodology will be discussed in section 2.3.5.

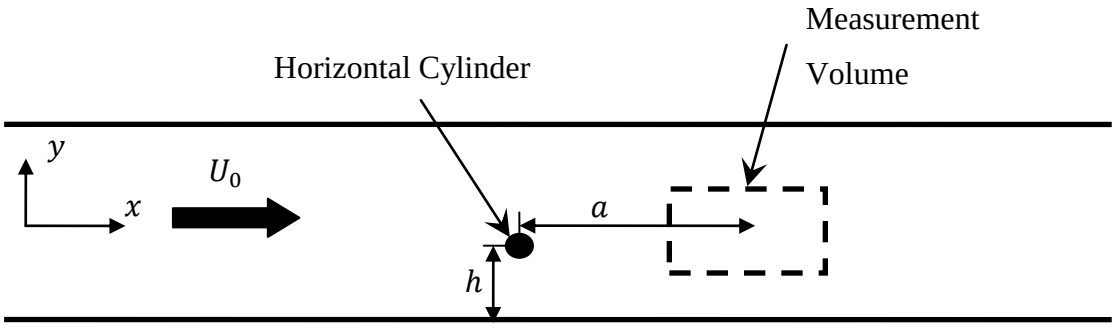

Figure 2-6: Schematic of horizontal cylinder location to measurement volume

2.3.4. Error of camera triangulation in 3D-PTV

A schematic of the camera arrangement as seen by the PTV cameras is shown in Figure 2-7. In this figure, X and Y are the horizontal and vertical image directions, respectively. In general, a two dimensional projection is mapped onto each camera to a X and Y location on the camera array. Then to compute a three dimensional location of the actual object, the X and Y location from camera 1 and camera 2 are used to triangulate the position. The software attempts to locate the centroid of the object by applying a Gaussian fit to sub-pixel accuracy for each of the two images and computes a velocity based on the known time difference between an image pair.

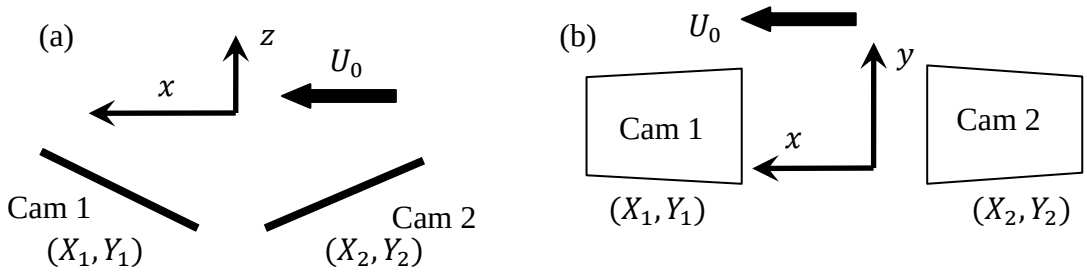

Figure 2-7: Arrangement of copepod tracking cameras in (a) x-z plane and (b) x-y plane

Figure 2-8 shows the pixel displacement in x, y, z, and total magnitude calculated from the measured copepod velocity for each component, u_c, v_c, and w_c in camera 1, camera 2, and both cameras. This is an example track of one copepod which exhibits an

escape where the escape is initiated before 0.02s. This data set was used to analyze how DaVis 8.0 computes velocity vectors for 2D-PTV from each individual camera and 3D-PTV for both cameras. From Figure 2-8 (b), camera 1 and camera 2 have very similar y displacement which results in the triangulated results of both cameras (3D-PTV) also being similar. This makes sense as from Figure 2-7 (b) both cameras have the same orientation in y and therefore the calculated displacement agrees. The x displacement is shown in Figure 2-8 (a), which shows that one camera calculates a smaller x displacement than the other. This makes sense as each camera is at a different angle to the streamwise and spanwise directions, and therefore each camera can see different displacements as the object travels along the streamwise direction, particularly if there is spanwise motion. There is one discrepancy point at 0.032s (shown by the large black arrow) where the calculated displacement for each camera is clearly different.

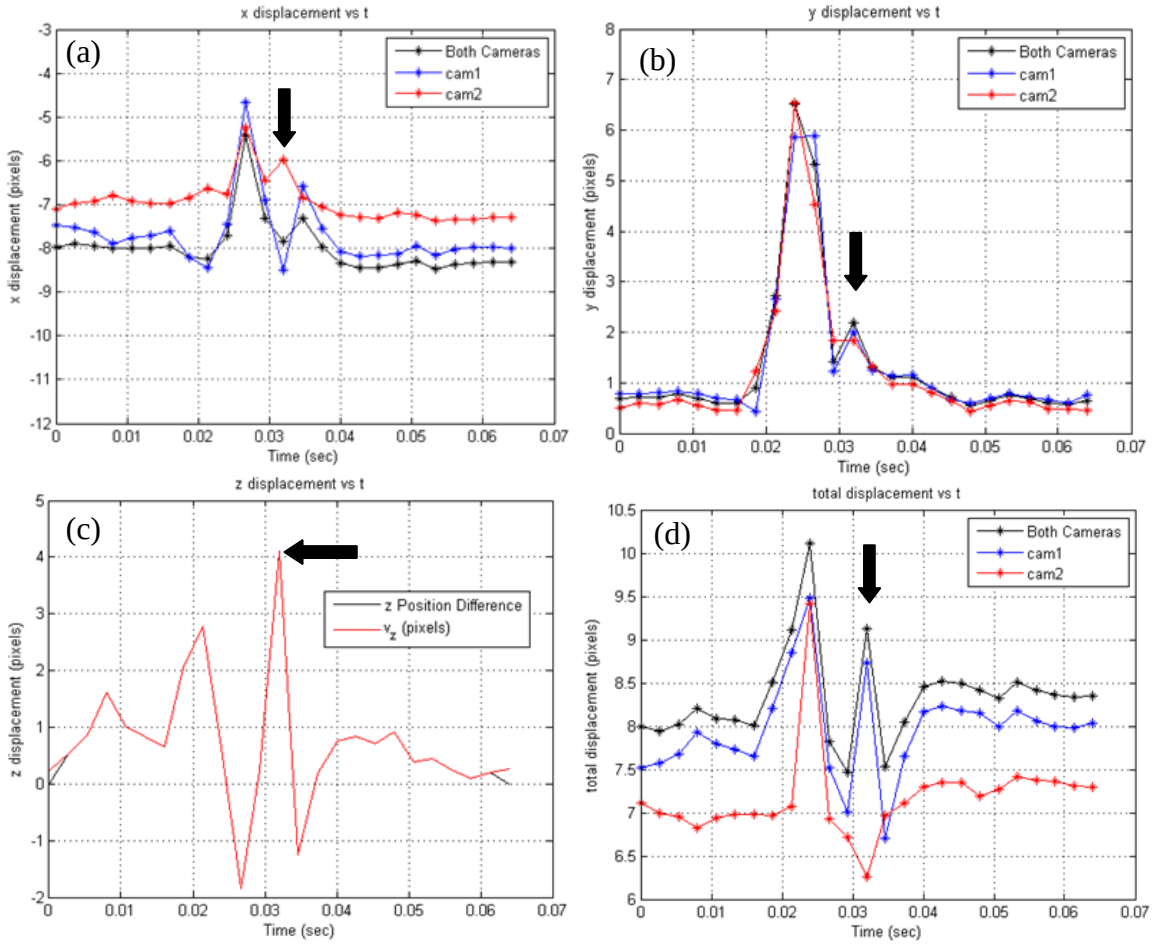

Figure 2-8: Example track comparing individual cameras and 3D triangulation for (a) x displacement, (b) y displacement, (c) z displacement, and (d) total displacement

The zoomed in image from each camera at this discrepancy point is shown in Figure 2-9. These images show a different projection of the copepod onto each image array. In camera 1, the swimming legs are barely seen, while in camera 2, the swimming legs make the copepod appear much larger. This gives a different centroid location in X calculated for each camera which explains the discrepancy point noted in the x displacement. However, the Y centroid appears to be similar for both images. This explains the results of Figure 2-8 (a) and (b). From the arrangement of both cameras, it can be seen that the triangulated z location is most dependent on the X centroid found for both images. Therefore, if there are discrepancies between X centroid calculations of each camera, then there will be resulting inaccuracies of the triangulated z location. This is seen in a large spike in Figure 2-8 (c) at the discrepancy point, again denoted by a large black arrow. Finally, this discrepancy is also seen in the total displacement. This does not represent the physical motion of the copepod but is an error resulting from each camera seeing different projections of the non-spherical copepod. This error can be reduced with image processing as will be discussed in section 2.3.5.

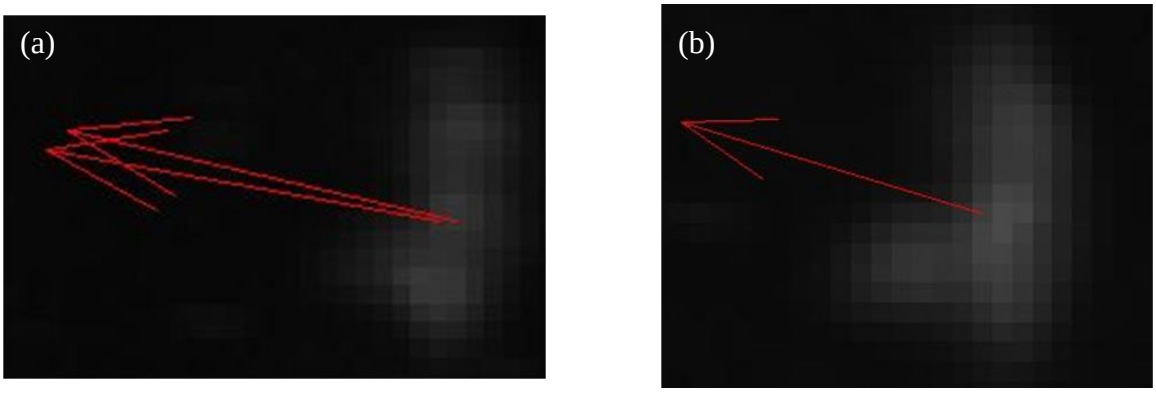

Figure 2-9: Raw images of (a) camera 1 and (b) camera 2 at discrepancy point (0.032 seconds) in Figure 2-8

2.3.5. Image processing methodology for 3D-PTV

As explained in section 2.3.4, the differences in projection of the copepod shape as seen from each camera array can lead to error in the *z* location. This error can be minimized by performing image processing in DaVis 8.0 before performing the 3D-PTV calculation. First, a 9x9 pixel Gaussian smoothing was applied to the raw images which is seen in Figure 2-10 (a) and (b). The images in Figure 2-10 are the results of image processing to the raw images in Figure 2-9. With the 9x9 pixel Gaussian smoothing, a sliding minimum of 11x11 pixels was subtracted and the pixel intensities normalized to a local average. In the image, the copepod was smoothed and had a larger pixel area. Another image processing technique used was an erosion of 5 pixels which can be seen in Figure 2-10 (c) and (d). Along with erosion, the sliding background of the Gaussian average of 10 pixels in the horizontal direction was subtracted. In the resulting image, the copepod takes up a smaller pixel area and the contrast to the background is more defined.

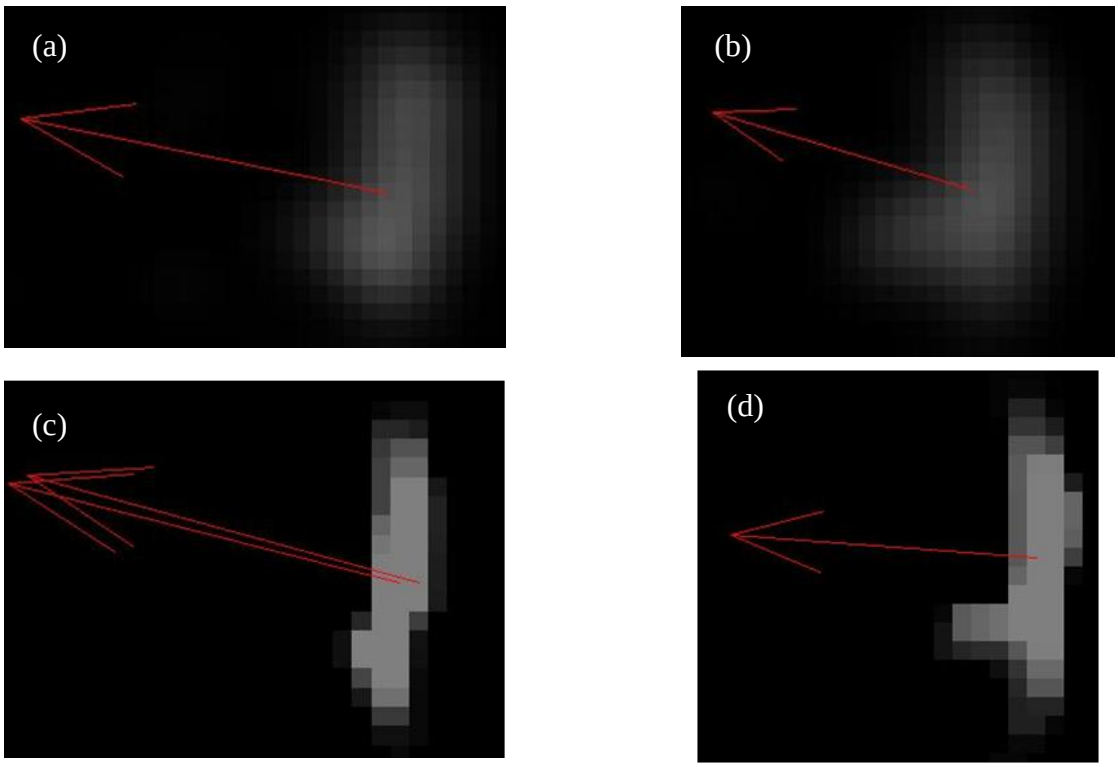

Figure 2-10: Images at discrepancy point (0.032 seconds) with Gaussian smoothing of (a) camera 1 and (b) camera 2 and with erosion of (c) camera 1 and (d) camera 2

From Figure 2-9 (a) and Figure 2-10 (c), it is noted that two vectors were calculated at that discrepancy point for camera 1 in 2D-PTV. When DaVis determines vectors for 3D-PTV the vectors are first calculated for each camera using 2D-PTV. Then from the calibrated volume, the resulting 3D-PTV vector is chosen from the two best matched vectors from each camera. Therefore, the two vectors from camera 1 shown in Figure 2-9 (a) and Figure 2-10 (c) will only result in one vector in the resulting 3D-PTV.

To determine which technique was better, the same data used for Figure 2-8 was processed with both techniques. The same settings for the 3D-PTV vector calculation were used. These included limiting triangulation to a set volume, having a Gaussian fit to best determine the centroid, and having a minimum intensity for the triangulated copepod. These results are found in Figure 2-11. The y displacement for erosion seems to differ slightly in Figure 2-11 (b). However, the x displacement for erosion seems to represent the copepod motion better in Figure 2-11 (a) as the peak at 0.032s is damped. Most importantly, the z displacement at 0.032s for erosion seems to be damped instead of amplified which appears to be the case for Gaussian smoothing. This is most likely due to the copepod taking up a larger pixel area for Gaussian smoothing as seen in Figure 2-10. The overall displacement (Figure 2-11 (d)) for erosion at 0.032s seems to be damped and most accurately captures the physical motion of the copepod. Therefore, the erosion image processing methodology was used for all 3D-PTV data.

It is important that only copepod motion was captured from 3D-PTV. Algae would end up in the water channel and would be recorded in the raw images of the PTV cameras. The erosion image processing methodology removed the algae that were only 1-2 pixels in thickness. The other zooplanktons (i.e. *Daphnia*, etc.) were not triangulated in the 3D-PTV calculations because of the set minimum intensity threshold. The other zooplankton would have a smaller intensity from the LED lights than the copepods. For each data set, it was visually confirmed that only copepods were being triangulated in the 3D-PTV vectors.

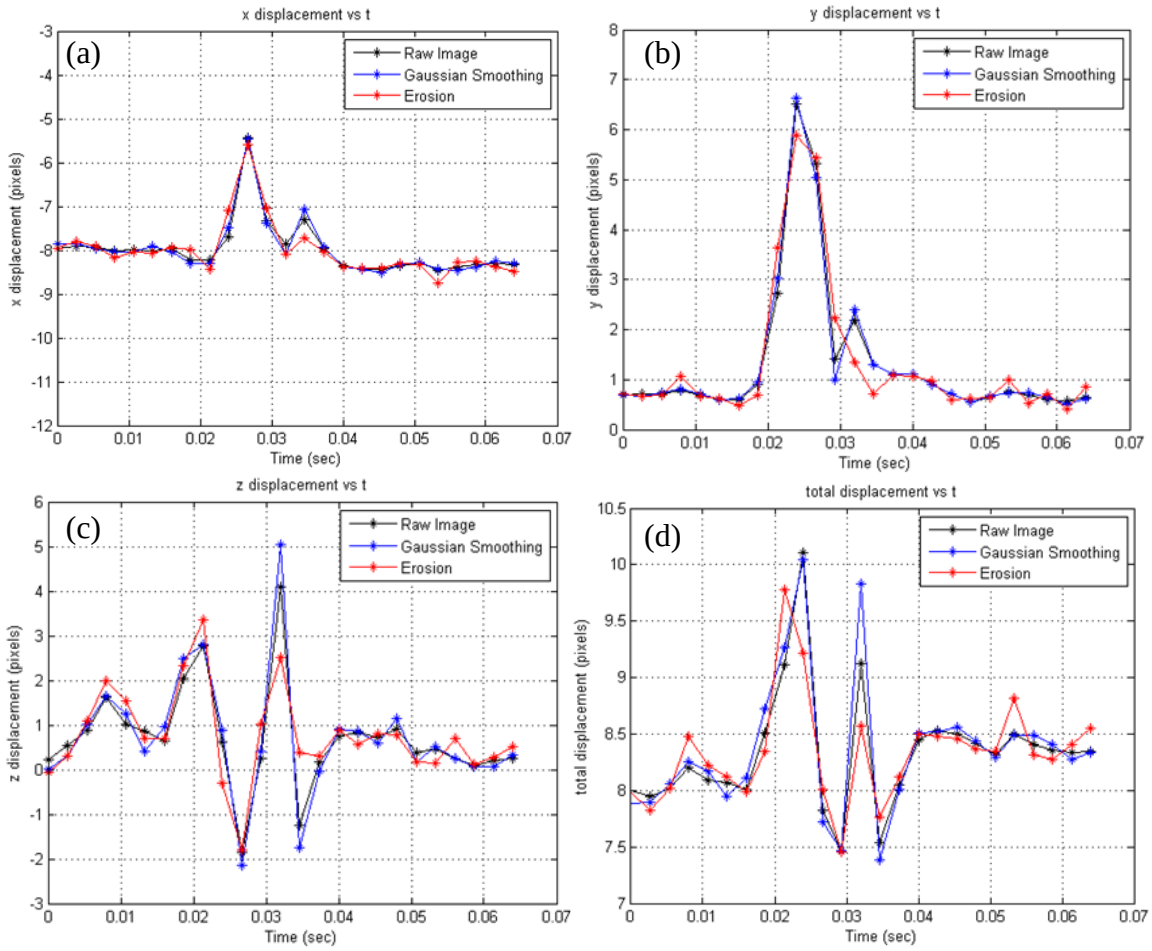

Figure 2-11: Example track comparing raw image (black), Gaussian smoothing (blue), and erosion(red) for (a) x displacement, (b) y displacement, (c) z displacement, and (d) total displacement

2.4. Experiments of fluid measurement

To better understand the flow in which copepods respond to, experiments were performed in which only flow was measured. These experiments were performed to record independent samples that are necessary to properly estimate velocity averages and root mean square velocity fluctuations. These include PPIV measurements of different spanwise locations of the freestream and bottom boundary layer, SPIV measurements downstream of the fractal grid and horizontal cylinder, and TPIV measurements downstream of the fractal grid. For this discussion, it is important to define timing parameters used to acquire independent samples. δt, as previously defined, is the time

between image pairs (i.e. laser pulses) necessary for cross correlation performed in PIV. This was selected so the approximate distance traveled in the streamwise direction by the tracer particles was a quarter of the interrogation window size. Δt is the time between sets of image pairs and is the time needed to have independent samples. To have flexibility in selecting δt and Δt, a programmable timing unit was used to trigger the cameras and laser.

2.4.1. Planar PIV measurements

PPIV was performed using one camera mounted at the test section normal to the streamwise direction. A 1mm thick laser sheet and silver coated particles were used. For PPIV measurements, 32x32pixel cross correlations with a 50% overlap were performed. This resulted in a plane of 80x50 vectors where the resolution of each fluid vector was 1.55mm (32x32 pixels). Experiments were performed with the paddlewheel set to 1RPM, 2RPM, and 3RPM. For 1RPM, δt was 0.00925s and Δt was 1.8s. For 2RPM, δt was 0.0045s and Δt was 0.9s. For 3RPM, δt was 0.003125s and Δt was 0.6s.

Two different experiments all at 1RPM, 2RPM, and 3RPM were performed with PPIV. One was done to quantify freestream flow at the test section. For this experiment, the camera and laser were mounted to be able to traverse to different spanwise locations in the channel. This was performed at three spanwise locations, which were at z locations of -0.035m, 0m, and 0.035m where z=0 is the center plane of the channel. At each location, 1000 independent samples were taken using the above timing conditions. A second experiment was performed to quantify the boundary layer at the center plane of the channel. This was done by focusing the camera and laser at the center plane where the bottom of the camera's field of view was at the bottom of the channel where 1000 independent samples were also taken.

2.4.2. Stereo PIV measurements

SPIV experiments were performed downstream of the fractal grid and horizontal cylinder at 1RPM and 3RPM settings on the paddlewheel. SPIV measurements were done using the setup in Figure 2-4 where only the PIV cameras were used. A 1mm thick laser sheet and silver coated particles were used. As done for experiments with copepods, the average background intensity was subtracted to eliminate background noise and a 32x32pixel cross correlation with a 50% overlap was performed. This resulted in a plane of 83x51 velocity vectors with a spatial resolution of 1.52mm per 32x32 pixel vector. For experiments downstream the fractal grid, Δt was 1.8s and 0.6s for 1RPM and 3RPM, respectively. For experiments at a of 0.12m and smaller, δt, was 0.008s and 0.002667s for 1RPM and 3RPM, respectively. For experiments at a of 0.2m and larger, δt was 0.008696s and 0.002899s for 1RPM and 3RPM, respectively. These times were selected to give an 8-10pixel displacement in the streamwise direction. For experiments downstream the horizontal cylinder, δt was 0.008696s and 0.002899s for 1RPM and 3RPM, respectively. However, for independent samples of the vortices shed off of the cylinder, Δt was 0.609s and 0.2079s for 1RPM and 3RPM, respectively.

2.4.3. Tomographic PIV measurements

TPIV measurements were performed downstream of the fractal grid for 1RPM and 3RPM at a of 0.055m. TPIV was done to provide three component velocity statistics for the entire measurement volume where copepod data was collected. In this section, the experimental setup and procedure will be discussed.

2.4.3.1.Experimental setup

A schematic of the experimental setup for TPIV can be found in Figure 2-12 where all six Phantom cameras were used. All of the cameras were mounted parallel to the bottom of the channel. Cameras 1, 3, 4 and 6 were all angled 20° from the spanwise

direction while cameras 2 and 5 were mounted parallel to the spanwise direction. All cameras had 105mm Nikon Micro-Nikkor lenses with the f-stop set to *f*/11. All cameras had Scheimpflug adapters mounted to the camera with the lens attached to adjust the plane of focus. The resulting measurement volume was 7.9cm in the x direction, 5.2cm in the y direction, and 2.6cm z direction where the bottom of the volume was 2.4cm from the bottom of the water channel. In order to have evenly distributed illumination across the measurement volume, a cylindrical lens was placed approximately 0.06m below the optical output of the laser head. A picture of the setup (without water in channel) with all six cameras, laser head, and cylindrical lens is seen in Figure 2-13.

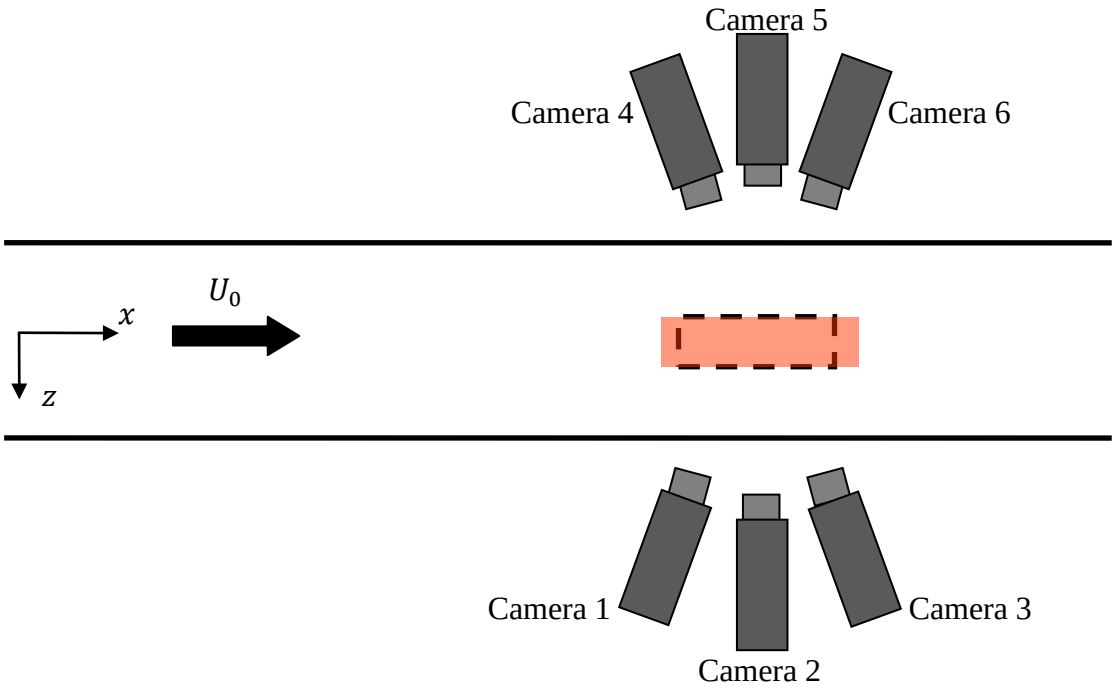

Figure 2-12: Top view schematic of tomographic PIV camera and laser setup. The red area is the illuminated region of laser and the dashed box is measurement volume

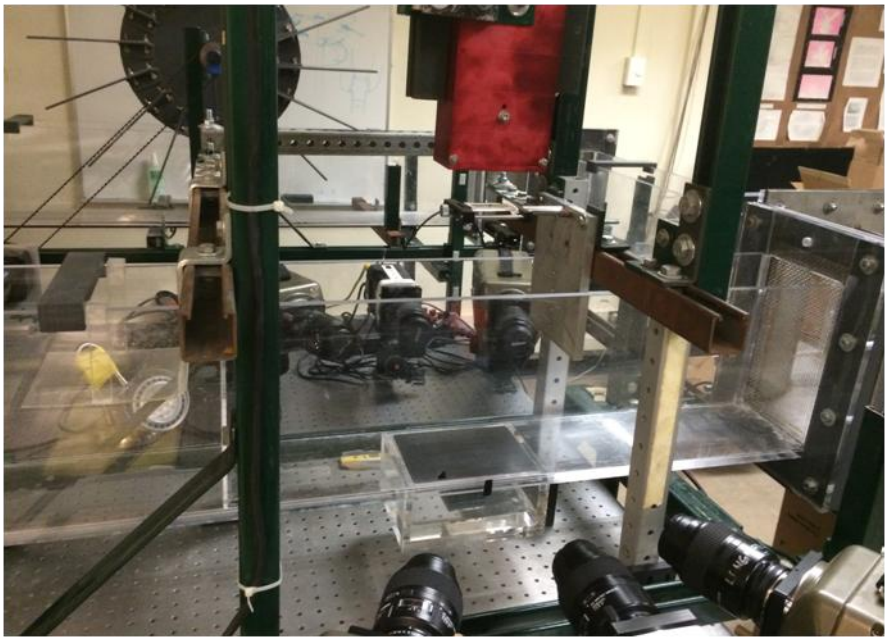

Figure 2-13: Picture of tomographic camera setup with laser

2.4.3.2.Experimental procedure

The channel was filled with water up to a height of 0.15m and seeded with 0.55μm polyamide particles as previously described in section 2.3.3. Calibration was performed with the double sided stepped LaVision 058-5 calibration plate mounted in the center of the channel. The calibration plate was not traversed spanwise across the volume to avoid error associated with traversing. Then self-calibration was performed in DaVis which reduced disparity errors. The minimum background intensity for each camera was subtracted from the images for each camera to eliminate background noise and reduce intensity differences. This also added to the quality of the reconstruction. The Fast MART reconstruction algorithm was implemented in DaVis 8.0. Using six cameras gave the potential for smaller spatial resolution of each vector. An interrogation volume of 32x32x32 voxels with 50% overlap was able to be achieved which gave a spatial resolution of 1.58mm (32x32x32 voxels) in all three directions for each vector. The resulting volume was 100x66x33 vectors. To measure independent samples, Δt was

1.8s and 0.6s for 1RPM and 3RPM, respectively. Also, δt was 0.008s and 0.002667s for 1RPM and 3RPM, respectively.

2.5. Uncertainty

For any experiment, there are two types of uncertainties, bias and random. Random uncertainty is the repeatability of a measurement and the random noise that is present in a measurement. This type of uncertainty uses statistics of many measurements. For PIV and PTV, the random uncertainty can be approximated by

$$\delta u = \frac{\sigma_{\Delta x}}{M\delta t}, \tag{2-1}$$

where $\sigma_{\Delta x}$ is the displacement uncertainty in x and M is the magnification of the measurement (Adrian and Westerweel 2011). Bias uncertainty is how close the measured value is to the 'true' value. This is dependent on calibration and the systematic error that can result from uneven camera focus across the measurement volume. In the experiments performed in this study, bias uncertainty can be estimated from results averaged over planar fields.

2.5.1. PIV

For PPIV and SPIV, bias uncertainty can be approximated by examining the mean velocity magnitude of the freestream for independent samples. Freestream flow is assumed to be uniform across the measurement region; therefore, variance in the mean is likely the result of systematic error. The results from SPIV measurement are shown and discussed in chapter 3. For both PPIV and SPIV, the bias uncertainty was found to be 1% of the freestream velocity. Random uncertainty can be approximated from Equation (2-1) which occurs from the uncertainty of locating the correlation peak in any direction for PIV. In PPIV, the random uncertainty can be calculated by approximating $\sigma_{\Delta x} = \sigma_{\Delta y}$ to be 0.1 pixels and M to be 0.048mm per pixel. However, SPIV has added error due to the cameras mounted at an angle. Adrian and Westerweel (2011) found that $\sigma_{\Delta x} \approx \sigma_{\Delta y}$

and $\sigma_{\Delta z} \cong \sigma_{\Delta x}/\tan(\beta)$ where β is the angle to the spanwise direction. β for the SPIV setup was 20° which gives $\sigma_{\Delta z} \cong 2.75\sigma_{\Delta x}$ or 0.275 pixels. δt was selected based on the freestream velocity which means the random uncertainty in x and y, $\delta u = \delta v$, can be given in terms of the freestream velocity, U_0. PPIV and SPIV have similar M and δt, so therefore the same random uncertainty can be approximated. For PPIV and SPIV in x and y, the resulting random uncertainty was found to be 1.4% of the freestream velocity. This gives a final uncertainty of 1.7% of the freestream velocity or $0.017U_0$. As previously discussed, SPIV has a larger random uncertainty in z which is $\delta w = 0.0385U_0$. This gives a final uncertainty in w of 4% of the freestream velocity or $0.04U_0$.

2.5.2. 3D-PTV

For 3D-PTV, random uncertainty can also be approximated with Equation (2-1) but $\sigma_{\Delta x}$ must be approximated for a Gaussian fit on a copepod. From Marxen *et al.* (2000), $\sigma_{\Delta x}$ can be approximated as 0.2 pixels based off a 10x10 pixel particle (copepod) with high noise level. M is approximated as 0.046mm per pixel throughout the measurement volume, and as discussed previously, δt scales with the freestream velocity. This results in a random uncertainty of $0.03U_0$ or 3% of the freestream. For 3D-PTV, bias uncertainty can be approximated by examining copepods drifting in uniform freestream flow. The copepods that drift through the measurement volume are at different y and z locations but have the same velocity magnitude. Therefore, examining how the velocity magnitude varies with x will give an approximation of the bias uncertainty. It was found for the 3D-PTV measurement set up that as x increased the measured velocity magnitude increased. Using this relation, the bias uncertainty for 3D-PTV was found to be approximately 2% of the freestream. For 3D-PTV, this gives a total uncertainty of 3.6% of the freestream or $0.036U_0$.

2.5.3. Tomographic PIV

For TPIV, data was only taken downstream of the fractal grid. Therefore, the uncertainty will be approximated only from random uncertainty. To determine the displacement uncertainty, $\sigma_{\Delta x}$, Adrian and Westerweel (2011) estimated a relative error distribution for all voxels that can be found from

$$\overline{\left(\frac{\partial u}{\partial x}+\frac{\partial v}{\partial y}+\frac{\partial w}{\partial z}\right)^2} \cong \left(\frac{\sigma_{\Delta x}}{D_I \delta t}\right)^2 \tag{2-2}$$

where D_I is the dimension of non-overlapping interrogation domain in the cross-correlation procedure. From Equation (2-2), the displacement uncertainty, $\sigma_{\Delta x}$, was found to be 0.12 voxels. M is approximately 0.049mm per pixel for TPIV measurements, and δt scales with the freestream velocity. This implies an uncertainty of 2% of the freestream or $0.02U_0$. This small uncertainty shows that the TPIV measurements were very accurate which follows from a six camera setup.

Chapter 3: Results and Analysis

In this chapter, all of the results and corresponding analysis will be discussed. This includes flow qualification, flow field results, copepod escape criteria, copepod escape results, copepod response downstream of fractal grid and horizontal cylinder, and MPSR during escape. Table 3-1 shows all of the experiments that were performed with data set names.

Table 3-1: List of data sets used in this study

Data set name	**Measuring**	**Flow obstacle**	**Flow speed (m/s)**	***a* (m)**	**Measurement type**
F1	Fluid and copepod	None	U_0 =0.039	None	PPIV, SPIV and 3D-PTV
F2			U_0 =0.076		
F3			U_0 =0.115		
BL1	Fluid		U_0 =0.039		PPIV
BL2			U_0 =0.076		
BL3			U_0 =0.115		
FG105	Fluid and copepod	Fractal grid	U_0 =0.039	0.055	SPIV, TPIV and 3D-PTV
FG305			U_0 =0.115		
FG108			U_0 =0.039	0.085	SPIV and 3D-PTV
FG308			U_0 =0.115		
FG112			U_0 =0.039	0.12	
FG312			U_0 =0.115		
FG120			U_0 =0.039	0.20	
FG320			U_0 =0.115		
FG140			U_0 =0.039	0.40	
FG340			U_0 =0.115		
HC105	Fluid and copepod	Horizontal Cylinder	U_0 =0.039	0.055	SPIV and 3D-PTV
HC305			U_0 =0.115		

3.1. Flow qualification

In this section, the freestream characteristics at the test section are analyzed. This includes the mean freestream flow with respect to the paddlewheel RPM, turbulence intensity of freestream, and boundary layer analysis.

3.1.1. Mean streamwise flow w.r.t paddlewheel RPM

As discussed in Chapter 2, PPIV measurements were performed at different spanwise locations for paddlewheel speeds of 1RPM, 2RPM, and 3RPM. The mean streamwise speed is shown in Figure 3-1. These results were computed from 1000 independent samples for each paddlewheel RPM and measurement location. As seen from Figure 3-1, the results are very similar for z=0 (center plane) and z=3.5cm for every paddlewheel RPM. For z=-3.5cm, the mean streamwise velocity is lower than the other two locations. At 1RPM, z=-3.5cm is about 6% lower than the other two locations, while at 2RPM and 3RPM, z=-3.5cm is about 8% lower than the other two locations. This increase in U_0 for increasing z is an artifact of the corners in the closed return water channel. However, this spanwise gradient is small. From this measurement, U_0 at the center plane was found to be 0.039m/s, 0.076m/s, and 0.115m/s for 1RPM, 2RPM, and 3RPM, respectively. These values are used in Table 3-1 to categorize each experiment.

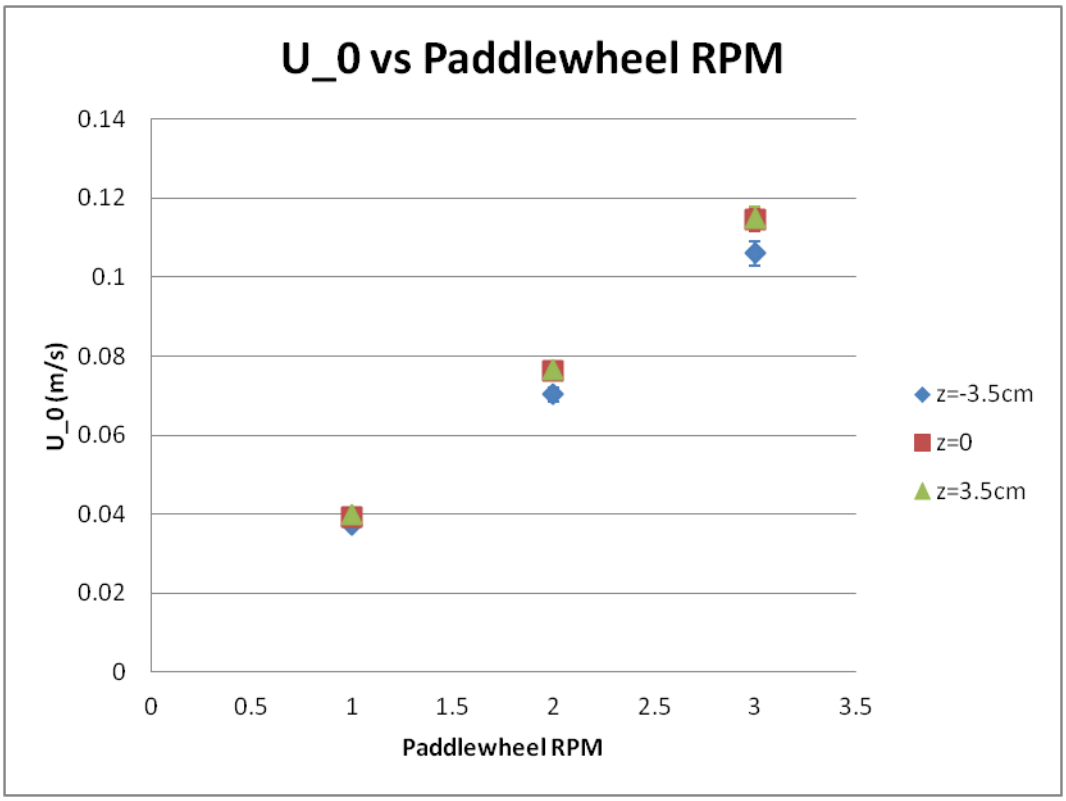

Figure 3-1: U_0 vs Paddlewheel RPM spanwise across channel for F1, F2, and F3

3.1.2. Freestream flow qualification in test section

SPIV experiments with 1000 independent samples were also performed for freestream at the center plane in the measurement volume at 1RPM and 3RPM. Fields of the mean velocity magnitude are shown in Figure 3-2. For both speeds, the variation of the velocity magnitude over the field is about 1% which is small. This small variation seen in Figure 3-2 appears to be from systematic error (calibration) and uneven focus of the images in SPIV. This is seen by the fields of TI shown in Figure 3-3. For both Figure 3-2 and Figure 3-3, the y axis is the distance from the bottom of the channel. This is confirmed by Figure 3-2 (a) where TI contours are spotty which is not representative of the flow but shows small systematic error. The average TI values for F1 and F3 are 2.5% and 2.1%, respectively. In the bottom of the field in Figure 3-2 (b), notice the mean

velocity is less than the rest of the field. At the bottom of the field in Figure 3-3 (b), TI values are larger than the rest of the field. This is an important characteristic for the F3 experiment which will be discussed in more detail in boundary layer analysis.

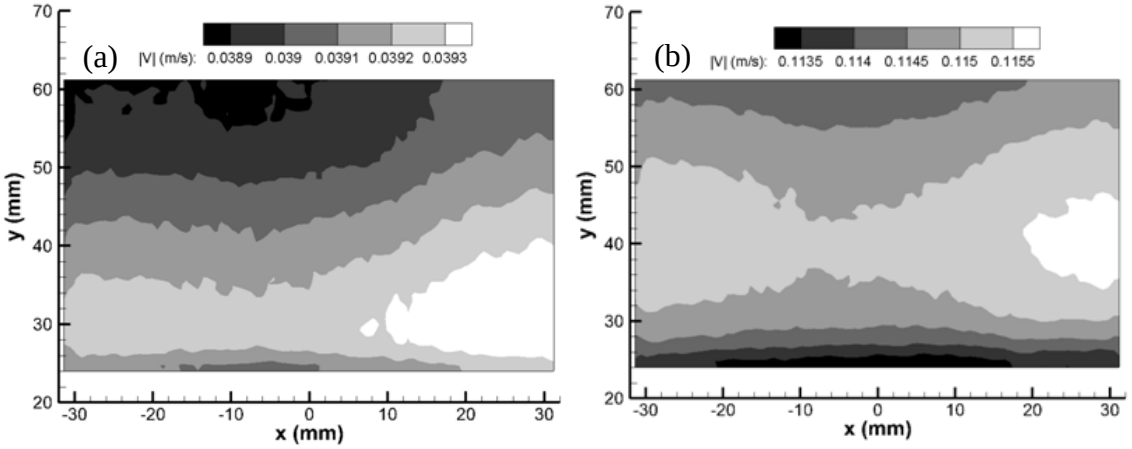

Figure 3-2: Mean velocity of freestream (m/s) flow field for (a) F1 and (b) F3

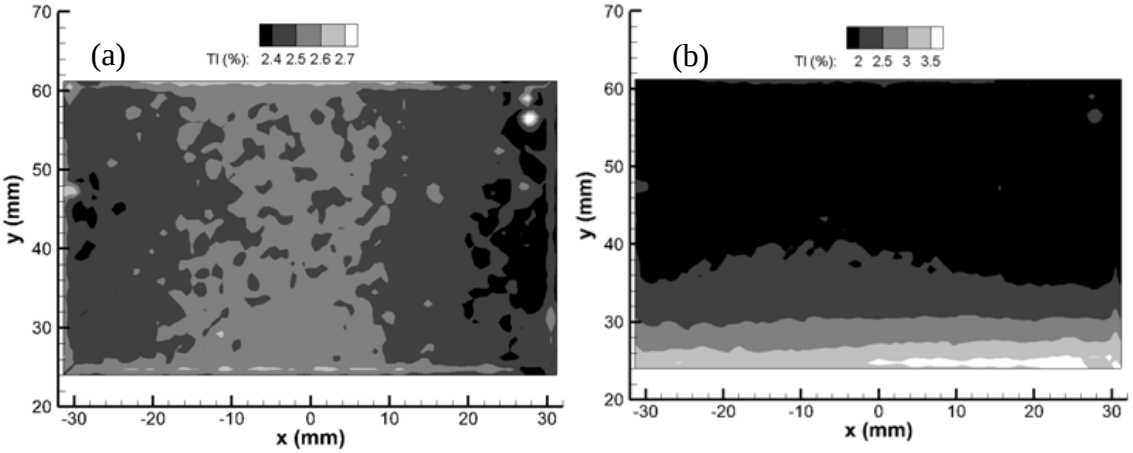

Figure 3-3: TI of freestream flow field for (a) F1 and (b) F3

3.1.3. Boundary layer analysis

PPIV for 1000 independent samples was measured for 3 different speeds at z=0 and bottom of the channel. The resulting boundary layer profiles are seen in Figure 3-4 where U_0 is taken from the results in Figure 3-1. The results $U(y)/U_0$ are found by averaging across x of the field of view. For flat plate boundary layer theory, $U(y)$ will increase for increasing y from y=0 until $U(y)$ converges to U_0. The results for BL1 and BL2 follow this expected trend. Close to y=0, BL3 follows this trend but then appears to

converge slower to U_0 than BL1 and BL2. In Figure 3-2 (b), the bottom of the field of view starts at 0.024m above the bottom of the channel for F3. From Figure 3-2 (b), the mean velocity is also found to be less than U_0 around 0.025m off of the bottom of the channel. This agreement in results from Figure 3-4 and Figure 3-2 (b) shows it is not an artifact of experimental error but a physical characteristic of the channel at this speed.

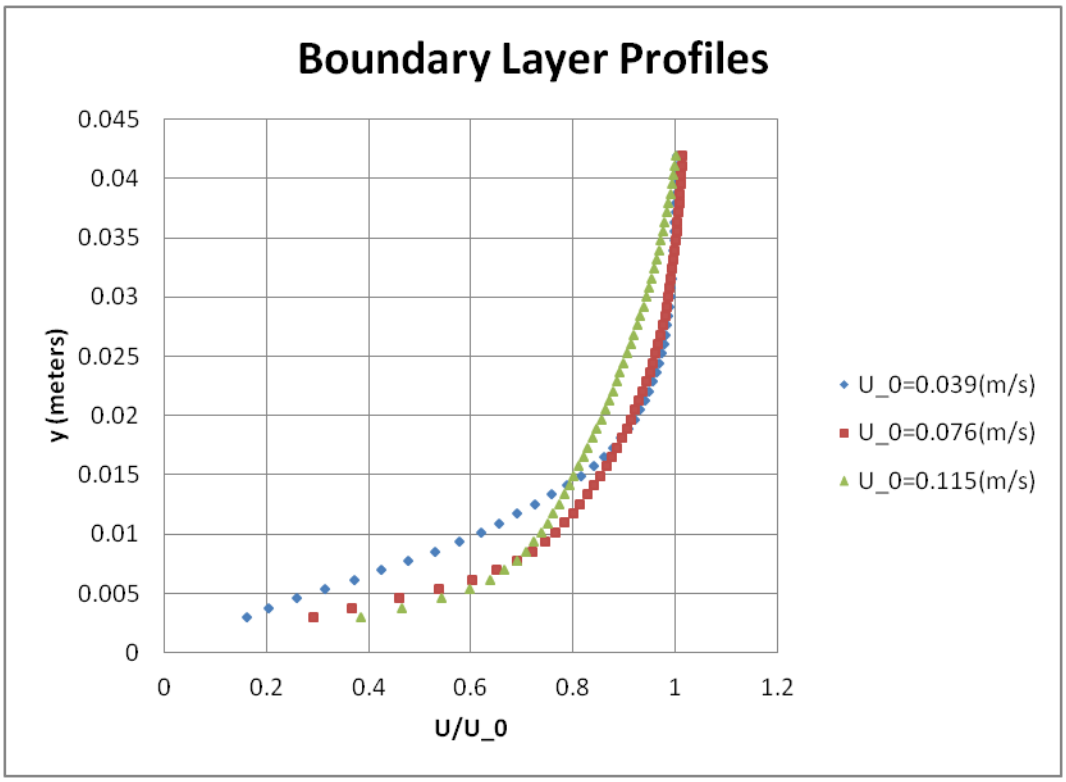

Figure 3-4: Freestream boundary layer profiles for BL1, BL2, and BL3

For further analysis of the boundary layer, the overall boundary layer thickness and momentum thickness are analyzed. The overall boundary layer thickness, δ_{99}, is defined as the distance from the bottom of the channel to where $U(y = \delta_{99}) = 0.99U_0$ (Kundu *et al.* 2012). For a laminar boundary layer on a flat plate, the Blasius solution gives $\delta_{99} = 4.93\sqrt{\nu x/U_0}$ where ν is the kinematic viscosity of the fluid and x is the distance on the plate which will be assumed as the distance from the last honeycomb before the test section (~1.25m). For turbulent flow, $\delta_{99} = 0.382x(U_0 x/\nu)^{-0.2}$ from Schlichting (1979). These solutions are for a flat plate and are therefore an

approximation for this water channel. The results of these approximations and experimental results are found in Figure 3-5. The experimental measurements are similar to the laminar approximation for BL1 and BL2. For BL3, the experimental results are closer to the turbulent approximation which confirms the results of higher TI values at 0.025m in Figure 3-3 (b).

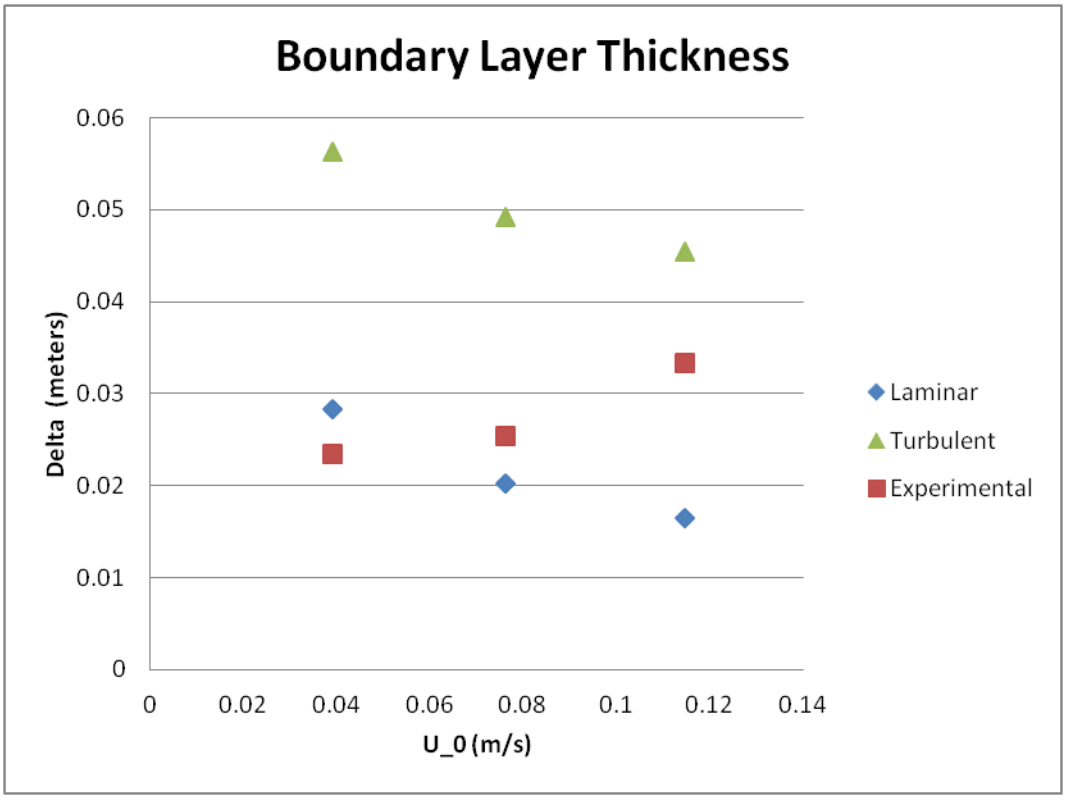

Figure 3-5: Freestream boundary layer thickness from BL1, BL2, and BL3

Another quantity used in analysis of boundary layers is momentum thickness, MT. MT is defined such that $\rho U_0^2 MT$ is the momentum loss in the flow from the boundary layer, where ρ is the density of the fluid. From a control volume calculation,

$$MT = \int_{y=0}^{\infty} \frac{U}{U_0}\left(1 - \frac{U}{U_0}\right) dy. \tag{3-1}$$

For a flat plate, there also exists a Blasius solution for MT for laminar flow, which is $MT = 0.664\sqrt{\nu x / U_0}$. From the experimental results of $U(y)$, Equation (3-1) was performed using the trapezoidal integration approximation. The results of the momentum

thickness are shown in Figure 3-6. Again, there is close agreement to the laminar approximation for BL1 and BL2, but the result for BL3 is greater than the laminar flat plate approximation. Overall, the results for boundary layer thickness and momentum thickness show that at U_0=0.115m/s the boundary layer differs from laminar results and is in transition to turbulence.

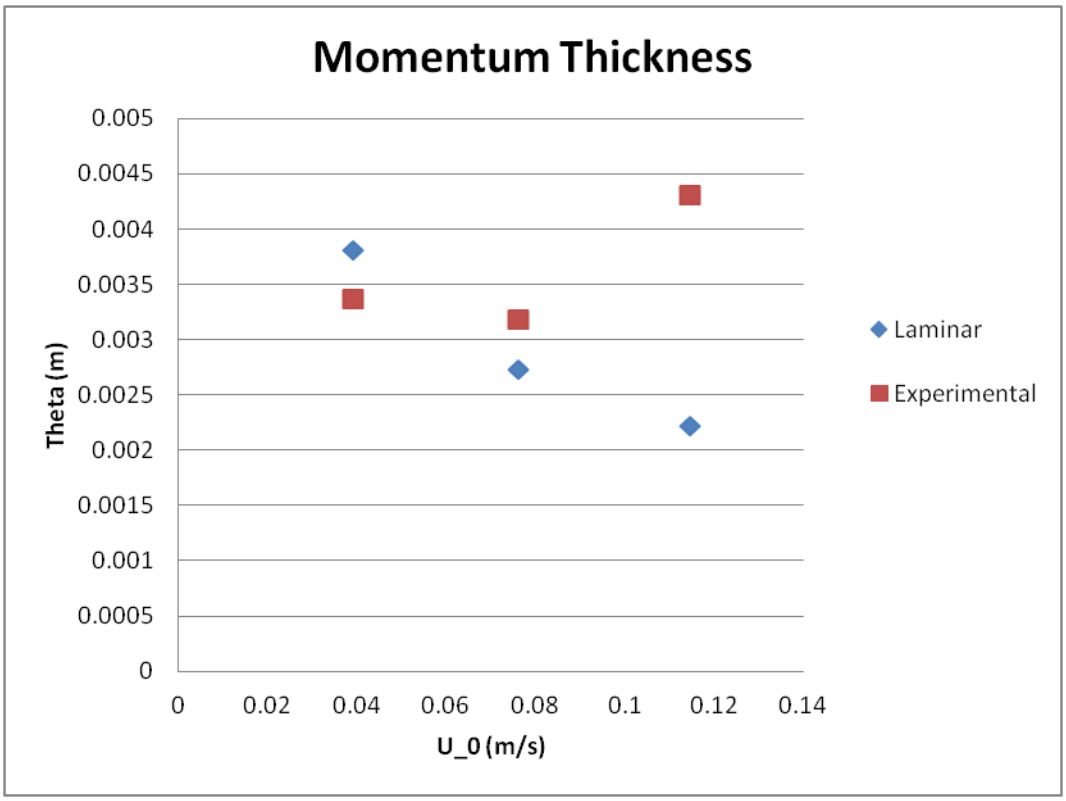

Figure 3-6: Freestream momentum thickness from BL1, BL2, and BL3

3.2. Flow field results

In this section, the flow fields downstream of the fractal grid and horizontal cylinder are analyzed. Specifically for the fractal grid, the flow development from near to far downstream, 3D flow field results for FG105 and FG305, and MPSR results for FG305 are presented in this section.

3.2.1. Downstream fractal grid

3.2.1.1. Flow development

For U_0 =0.115m/s, Figure 3-7 shows the averaged flow field results of each component non-dimensionalised by U_0. Figure 3-8 shows the root mean square fields of each component non-dimensionalised by U_0 and TI field. For both figures, x and y are non-dimensionalised by the thickest beam, d_0, where x=0 is the trailing edge of the grid and y=0 is the center of the thickest beam in the field (see Figure 2-5).

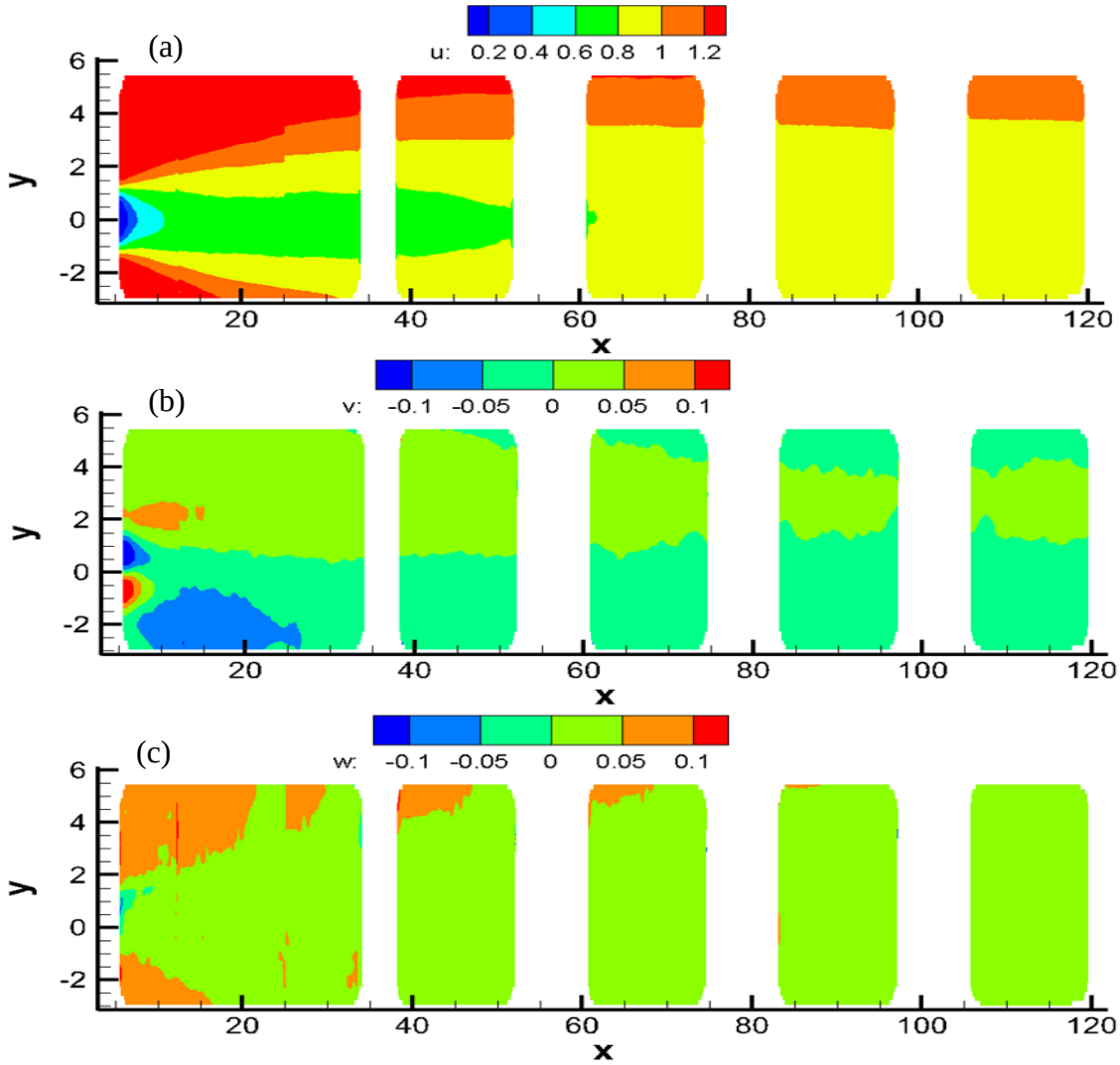

Figure 3-7: Mean flow fields downstream fractal grid at U_0 =0.115m/s of (a) $\frac{U}{U_0}$, (b) $\frac{V}{U_0}$, and (c) $\frac{W}{U_0}$ with the grid at x=0 where x and y are non-dimensionalised by d_0

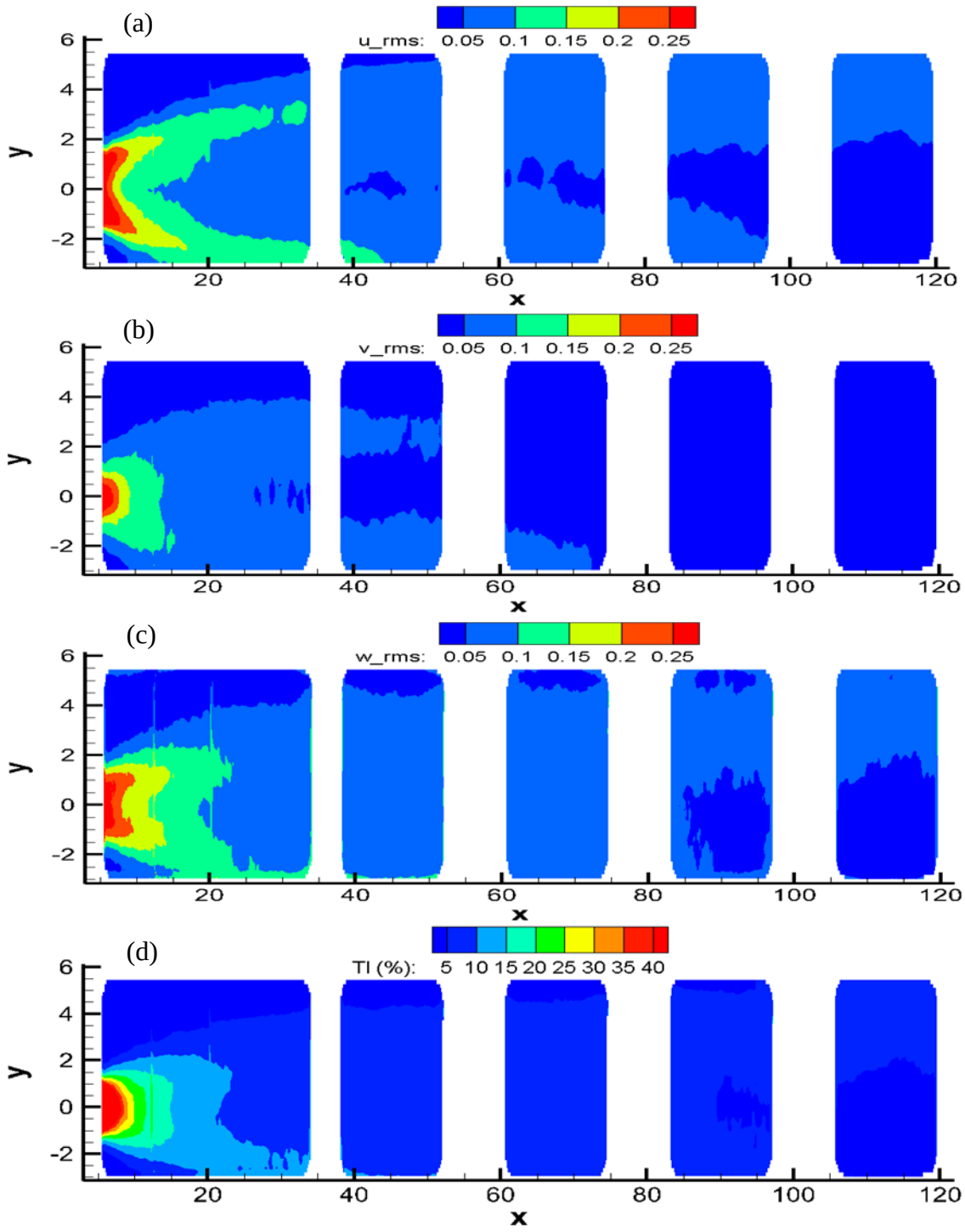

Figure 3-8: Root mean square velocity downstream fractal grid at U_0 =0.115m/s of (a) $\frac{u_{rms}}{U_0}$, (b) $\frac{v_{rms}}{U_0}$, (c) $\frac{w_{rms}}{U_0}$, and (d) TI as percentage with the grid at x=0

The results in Figure 3-7 and Figure 3-8 are from SPIV measurements performed at the center plane of the channel. All of the results are from 1000 independent samples

at each location and plotted together. From Figure 3-7 (a), the red contour indicates that the 25% blockage of the fractal grid causes the flow in the streamwise direction to be accelerated locally to velocities greater than U_0. Only the largest iteration of the fractal grid is directly upstream at z=0 where SPIV was performed, and therefore it is the dominate factor in these measurements. The blue and green contours in Figure 3-7 (a) show the strong wake that is present near the grid. The region where U/U_0 contours vary from yellow to red in y indicates a shear layer. Further downstream, the wake weakens and U converges back to U_0. The near wake is also noted by the red and blue contours in Figure 3-7 (b). This shows the wall-normal velocity converging inward immediately behind the largest grid member and diverging outward at larger y magnitudes. Further downstream, V/U_0 remains close to zero. For z=0, Figure 3-7 (c) shows uniform W/U_0 due to the symmetry of the grid. From Figure 3-7 (c), W/U_0 is almost entirely greater than zero. This is most likely a result of a slight misalignment in the laser sheet and not an accurate representation of what is occurring in the flow. A misalignment of only 1° in the laser sheet could cause these positive values in W/U_0. This will be examined further from the volumetric TPIV results.

In a wake, velocity fluctuations are larger when flow is more turbulent. Figure 3-8 (a)-(c) show higher contour values for each component of the root mean square velocity. In Figure 3-8 (a), u_{rms}/U_0 is large in the near wake and decreases further downstream. The previously mentioned shear layer is seen in Figure 3-8 (a) by the green contour region that separates and extends downstream past x=30. This shear layer is relatively symmetric over y=0. The separation shows weaker streamwise fluctuations in the wake region near y=0 where U/U_0 is smaller in Figure 3-7 (a) (green contour region). In Figure 3-8 (b), the highest fluctuations again occur in the near wake where the positive and negative V/U_0 regions interact in Figure 3-7 (a). v_{rms}/U_0 values drop off quicker than u_{rms}/U_0 with increasing downstream distance. In Figure 3-8 (b), v_{rms}/U_0 values are low in the shear layer. In Figure 3-8 (c), w_{rms}/U_0 values are large in the near wake and again symmetry is observed over y=0. w_{rms}/U_0 fluctuations are approximately 5% larger in the shear layer than v_{rms}/U_0. These larger w_{rms}/U_0 values show there is interaction in the flow from the other iterations of the fractal grid.

The velocity fluctuations of all components can be examined independently of a coordinate system by turbulence intensity. TI is seen in Figure 3-8 (d). The highest values are seen in the near wake and dissipate further downstream. These TI values greater than 40% in the near wake are in close agreement with results from Laizet and Vassilicos (2011). For all of the results in Figure 3-8, the largest fluctuations occur in the near wake of the thickest beam and dissipate downstream. All of the results in Figure 3-7 and Figure 3-8 display symmetric behavior over y=0 which shows iteration 0 of the grid has the largest effect on the flow. The location of the largest velocity fluctuations and resulting turbulence is in the near wake of iteration 0. Therefore, further volumetric analysis in the region of x less than 20 will provide more insight.

3.2.1.2. 3D flow fields for FG305

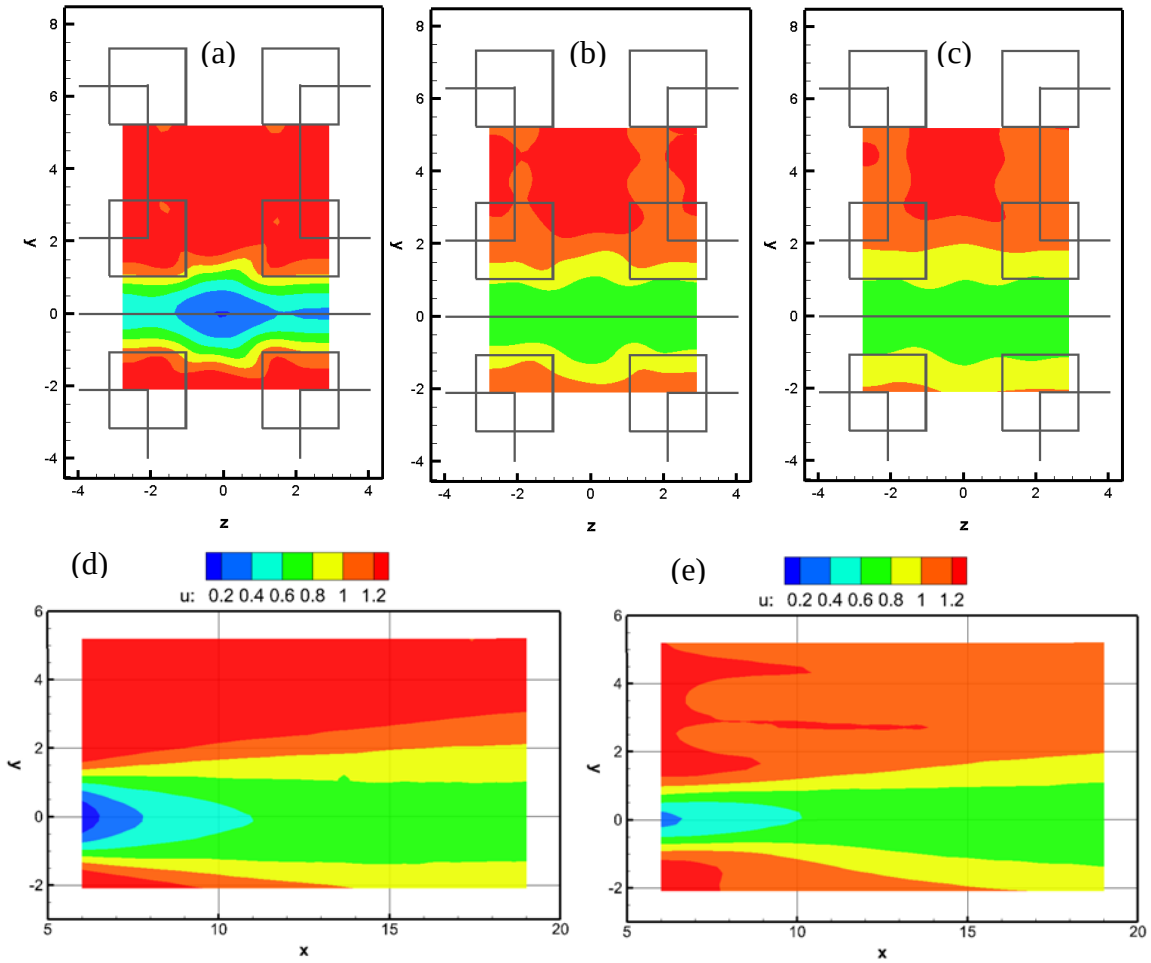

Figure 3-9: $\frac{U}{U_0}$ for FG305 at (a) x=6.5, (b) x=11.5, (c) x=16, (d) z=0, and (e) z=1.4 where x, y, and z are non-dimensionalised by d_0

Figures 3-9 through 3-15 show FG305 results from TPIV. Again, x=0 is the trailing edge of the grid, y=0 is the center of the thickest beam (iteration 0), and z=0 is the center plane of grid. The results in this section are non-dimensionalised by d_0 for x, y, and z. For results plotted in the y-z plane, the centerlines of iterations 0, 2, and 3 of the fractal grid upstream are shown. Results from Figure 3-9 (d) at z=0 and Figure 3-7 (a) show that SPIV and TPIV give similar results. Figure 3-9 (a) shows that the large streamwise flow deficit in the near wake (U/U_0 less than 0.4) is not uniform across the span of the measurement volume. The wake in Figure 3-9 (a) displays symmetry across y=0 and z=0 and the irregular shape implies flow interaction from iterations 1 through 3.

Further downstream in Figures 3-9 (b) and (c), the mean wake retains the symmetric and irregular shape. Additionally in Figures 3-9 (b) and (c), U remains larger than U_0 in the region close to z=0 where $|y|$>2. The streamwise flow deficit caused by iteration 2 is seen. This agrees with a conclusion of Laiset and Vassilicos (2011) where flow was found to hold clear geometrical imprints of the grid. Figure 3-9 (e) as compared to Figure 3-9 (d) shows slower fluid at larger y and not as drastic of a streamwise deficit in the near wake caused by iteration 0.

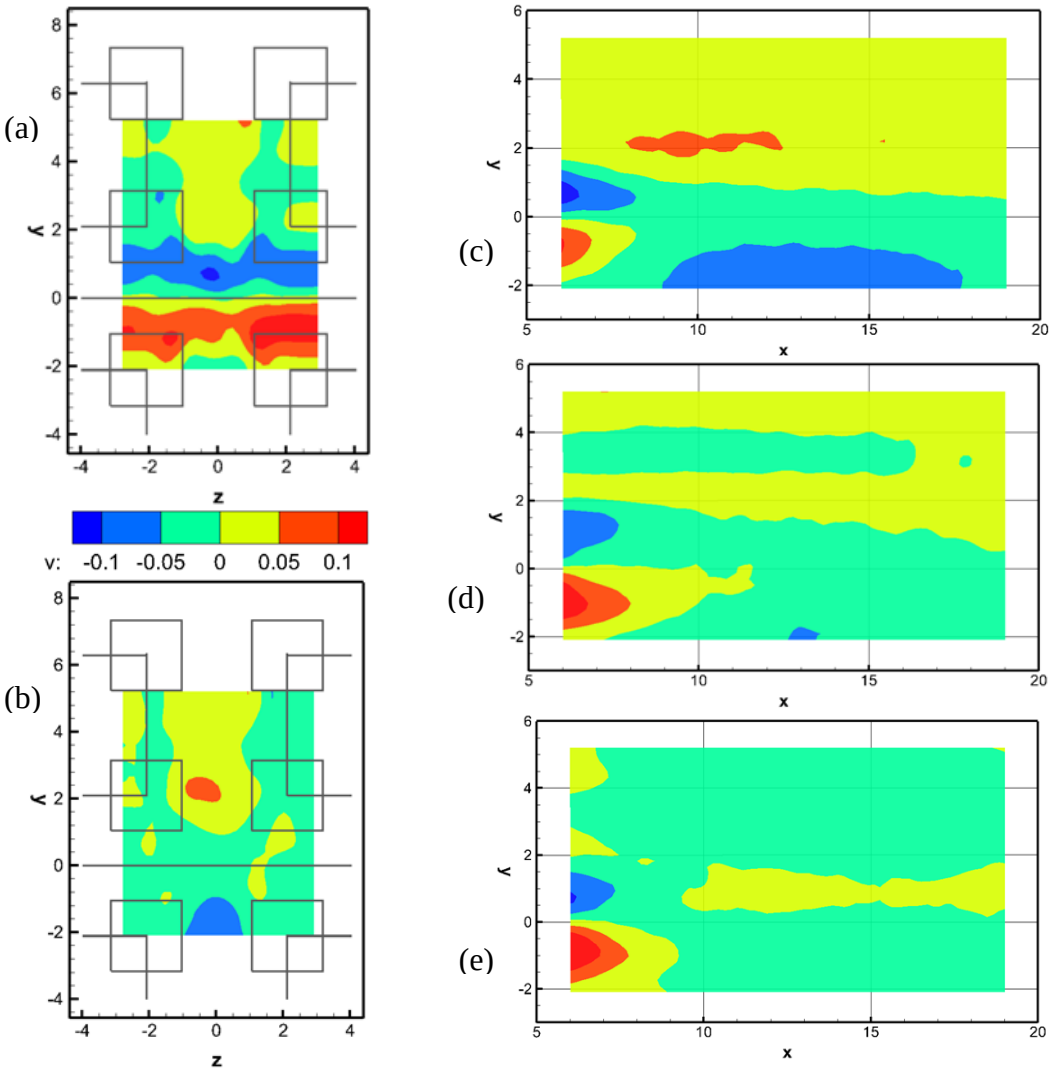

Figure 3-10: $\frac{V}{U_0}$ for FG305 at (a) x=6.5, (b) x=11, (c) z=0, (d) z=1, and (e) z=2

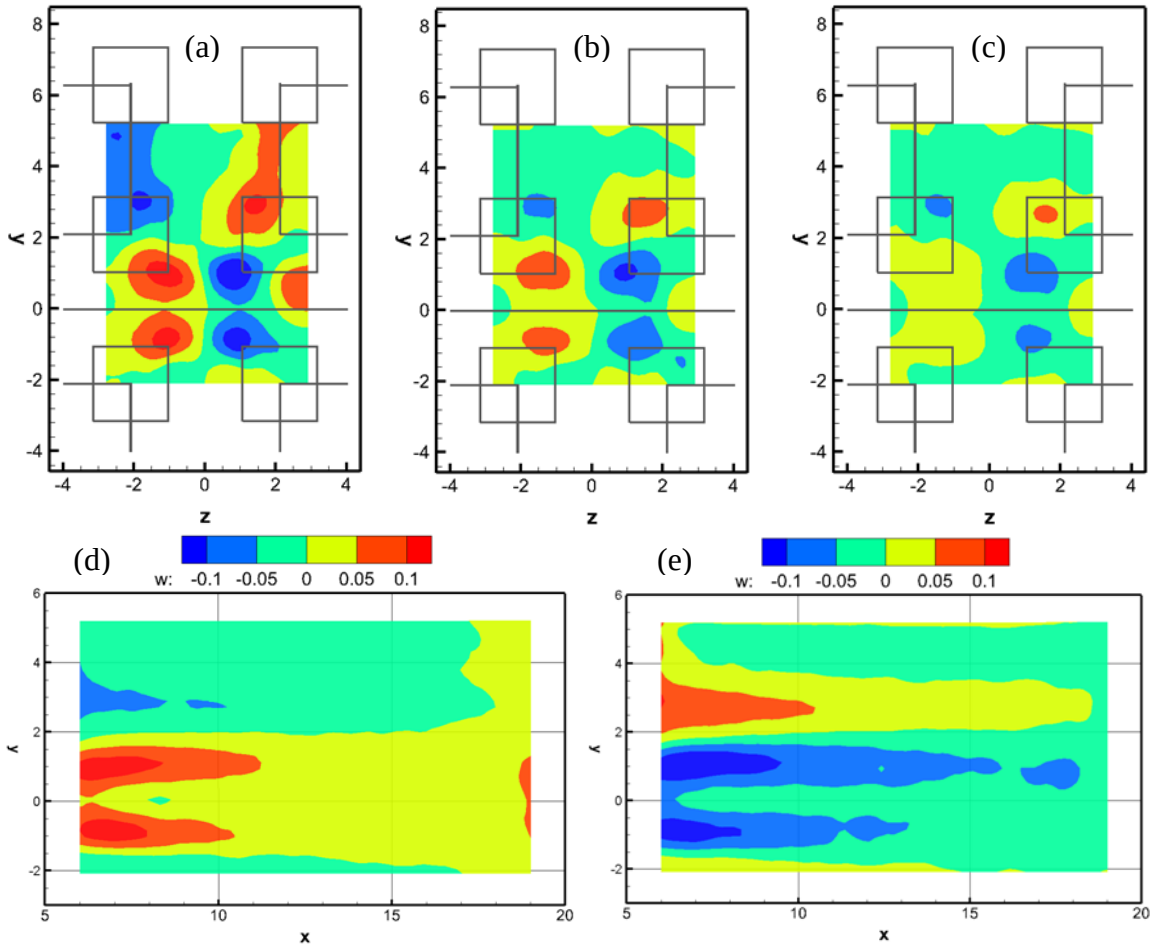

Figure 3-11: $\frac{W}{U_0}$ for FG305 at (a) x=6.5, (b) x=9, (c) x=12, (d) z=-1, and (e) z=1

Results from SPIV and TPIV are in agreement in both vertical and spanwise components, as seen in Figure 3-10 (c) and Figure 3-11 (a)-(c) compared to Figure 3-7 (b) and (c). Figure 3-10 again shows convergence of the wall-normal velocity component in the near wake and V/U_0 values close to zero further downstream. Figure 3-10 (a) shows this convergence is present across the entire span of the measurement volume. Figure 3-11 shows that for y less than 2, W is converging towards z=0 downstream of the fractal grid. For y greater than 2, W is diverging away from the center plane. This contrast shows the crucial role iterations 1 through 3 have on the flow. In Figure 3-11 (a) for y less than 2, iteration 0 and 3 seem to give clear geometrical imprint, while for y greater than 2, iteration 2 and 3 seem to give geometrical imprints. Results in Figure 3-7 (c) from SPIV show slightly larger values in W/U_0 than observed in Figure 3-11 at z=0 which confirms the previously discussed slight misalignment of the laser sheet for SPIV.

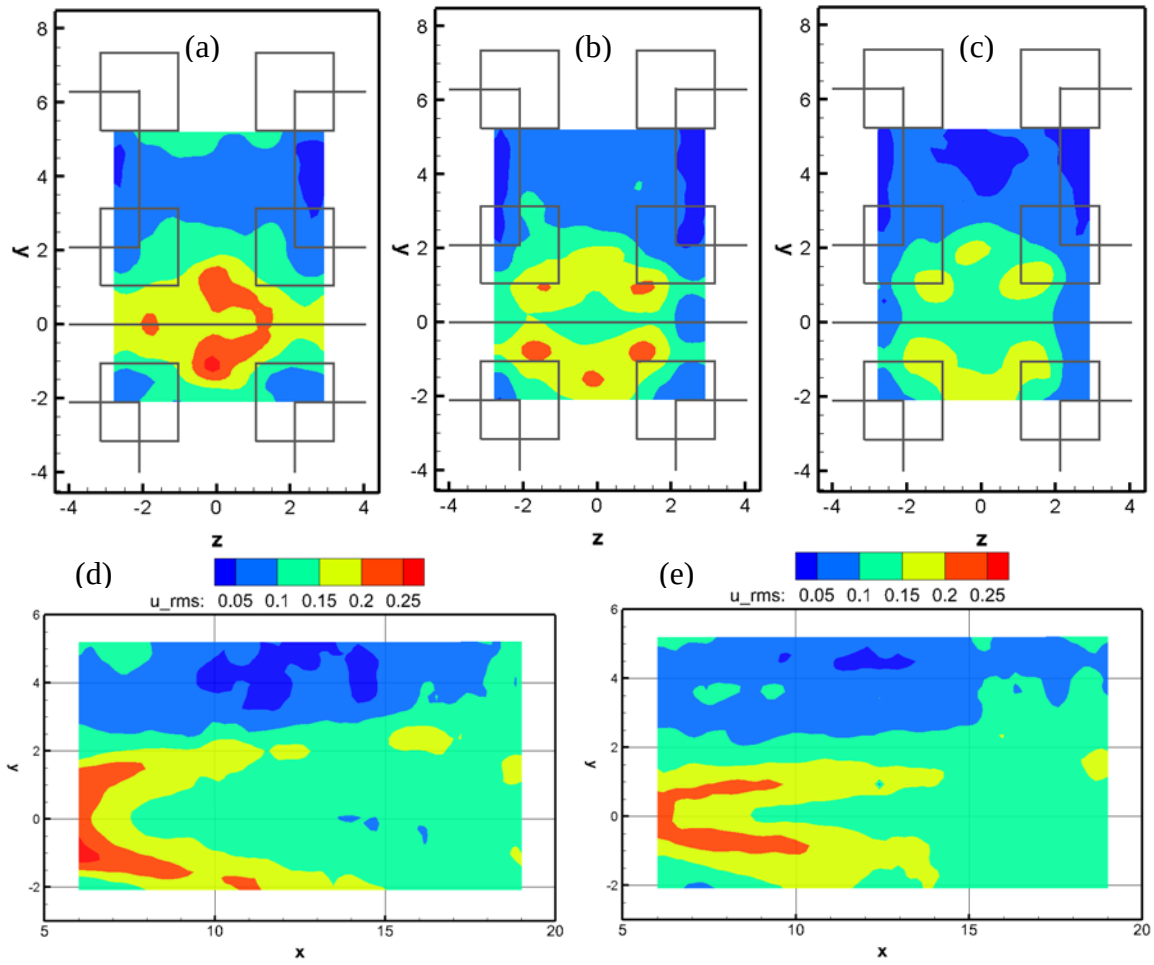

Figure 3-12: $\frac{u_{rms}}{U_0}$ for FG305 at (a) x=6.5, (b) x=9, (c) x=12, (d) z=0, and (e) z=1

Streamwise velocity fluctuations are shown in Figure 3-12, where again larger velocity fluctuations are seen in the near wake and propagated downstream. From Figure 3-12 (d) and (e), symmetry over y=0 is present, but in Figure 3-12 (b) and (c), symmetry is also seen across z=0. This shows that the smaller iterations give fluctuations of similar magnitude which is seen by the clear geometrical imprint in Figure 3-12 (b). Streamwise velocity fluctuations from SPIV shown in Figure 3-8 (a) are very similar to results observed in Figure 3-12 (d).

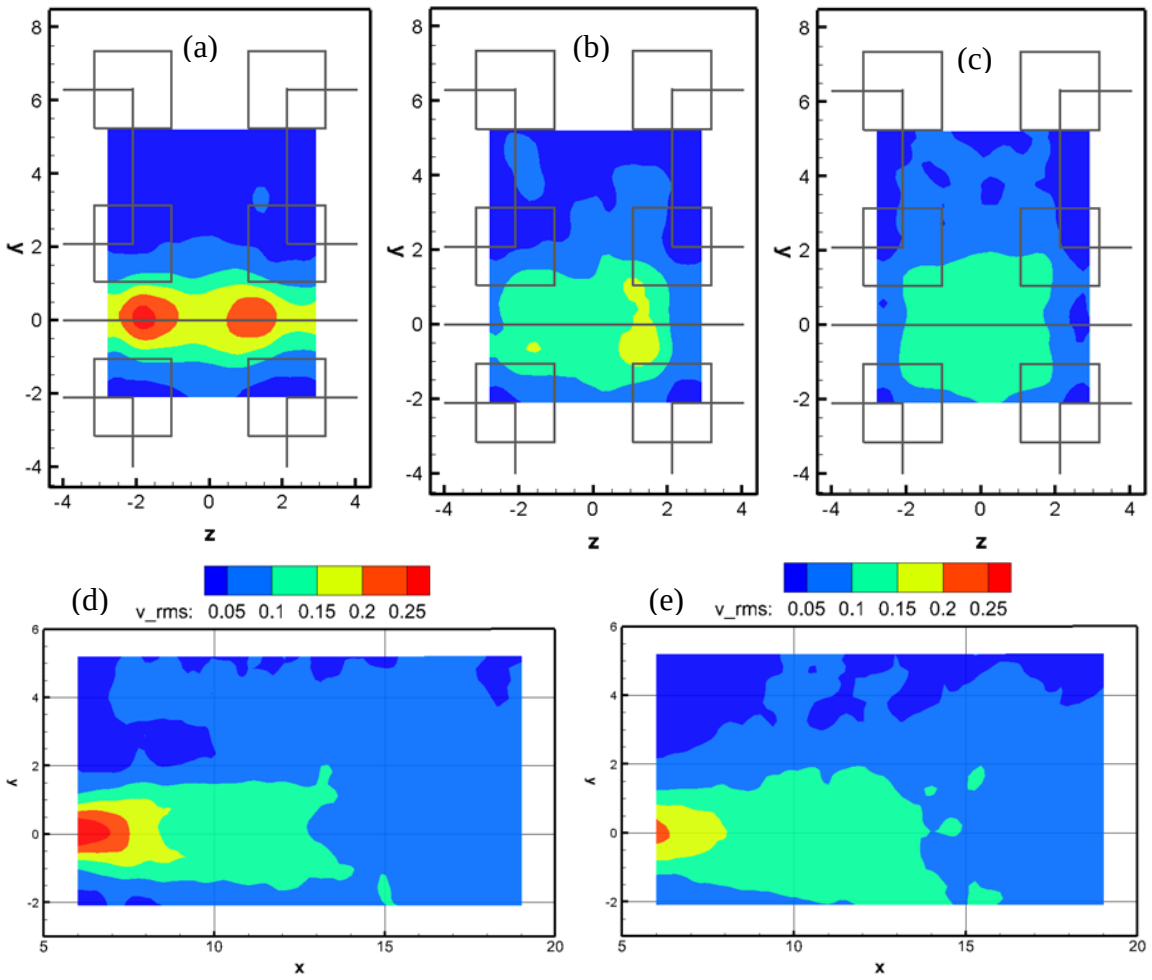

Figure 3-13: $\frac{v_{rms}}{U_0}$ for FG305 at (a) x=6.5, (b) x=9, (c) x=12, (d) z=-1.8, and (e) z=0

Figure 3-13 shows wall-normal velocity fluctuations. As previously seen, the largest fluctuations occur in the near wake of iteration 0 where V/U_0 is converging back to zero. However, these fluctuations seem to be amplified by the interaction of the smaller iterations. This is seen in Figure 3-13 (a) where larger v_{rms}/U_0 values are present downstream of smaller iterations which gives symmetry over z=0. Again, similar results from TPIV are observed at z=0 as seen in Figure 3-8 (b) from SPIV.

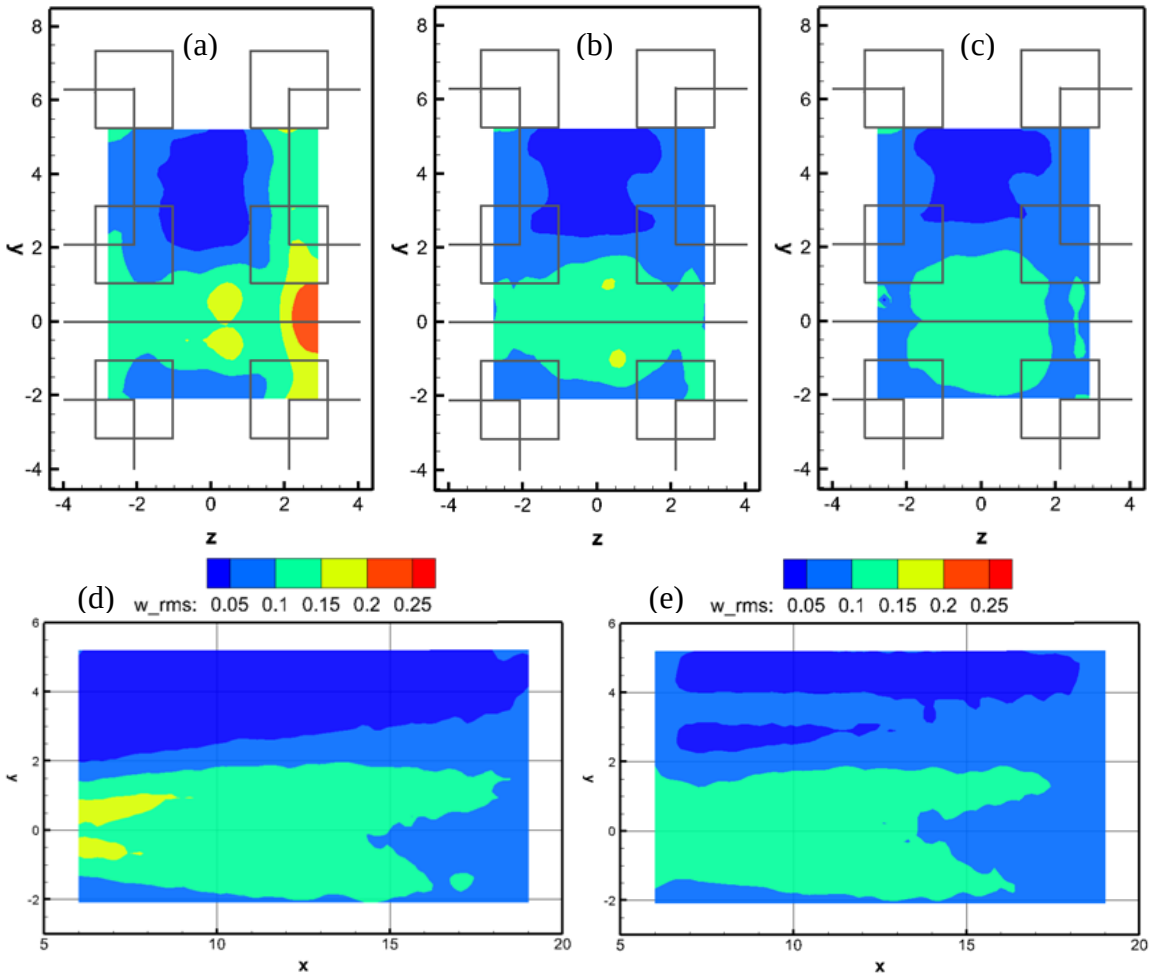

Figure 3-14: $\frac{w_{rms}}{U_0}$ for FG305 at (a) x=6.5, (b) x=9, (c) x=12, (d) z=0, and (e) z=1

Spanwise velocity fluctuations are found in Figure 3-14. Again, larger fluctuations are initiated in the near wake and are propagated downstream, and there are increased fluctuations from smaller iterations. w_{rms}/U_0 values are smaller than u_{rms}/U_0 or v_{rms}/U_0 values. The results in Figure 3-14 from TPIV show smaller spanwise fluctuations compared with SPIV in Figure 3-8 (c). This is an artifact of higher random uncertainty for w in SPIV due to the camera arrangement as discussed in Section 2.5.1. Therefore, the results observed from TPIV in Figure 3-14 are more accurate. These small fluctuations imply that the converging and diverging behavior witnessed in W/U_0 of Figure 3-11 is consistent.

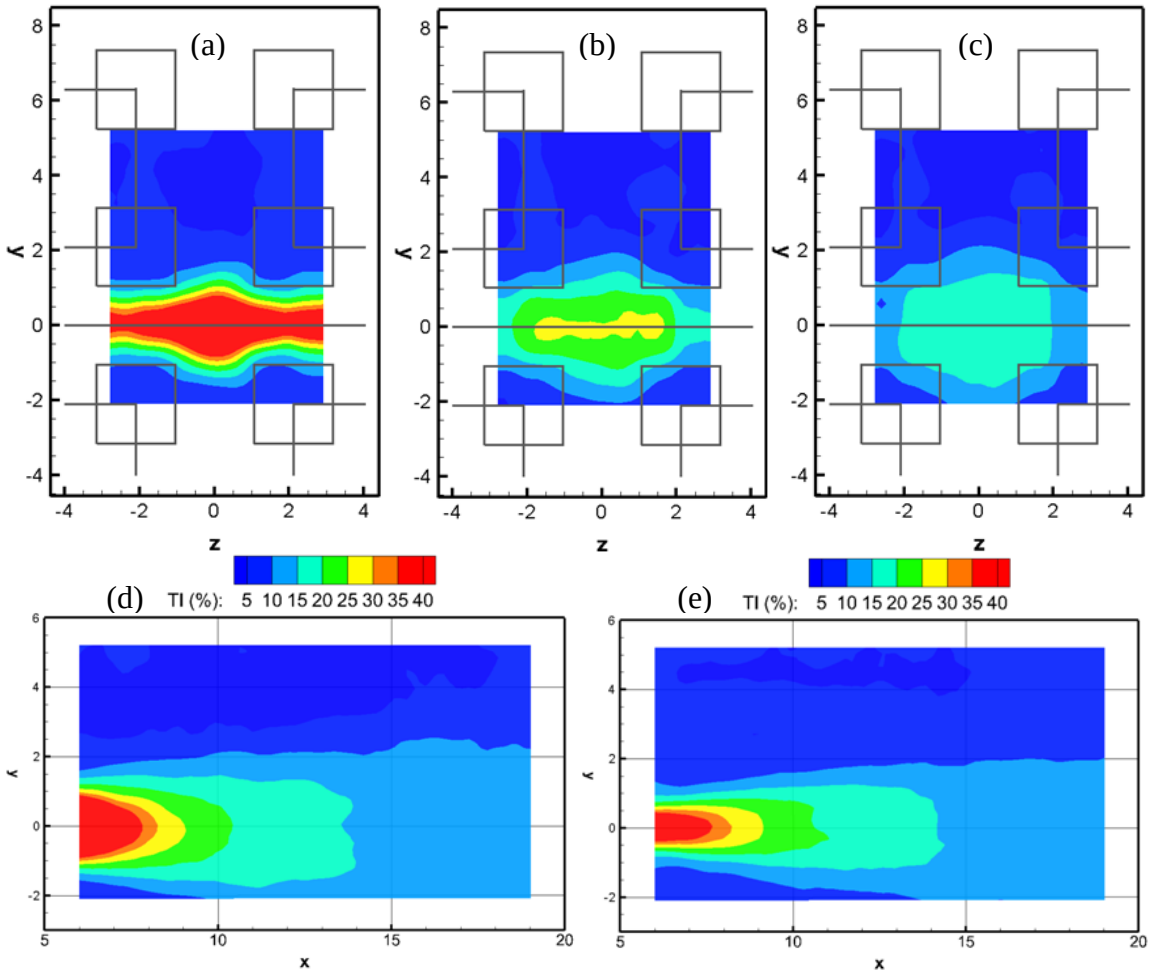

Figure 3-15: *TI* as percentage for FG305 at (a) x=6.5, (b) x=9, (c) x=12, (d) z=0, and (e) z=1.4

The results of the turbulence intensity are found in Figure 3-15. Symmetry over y=0 and z=0 is observed. *TI* is largest in the near wake of the iteration 0 as observed previously and was found to exceed 95%. In Figure 3-15 (a)-(c), clear geometrical imprints from higher grid iterations are less distinct than for individual components. For further insight, the results of FG305 in Figure 3-9 through Figure 3-15 can be compared to results of FG105.

3.2.1.3. 3D flow field comparison

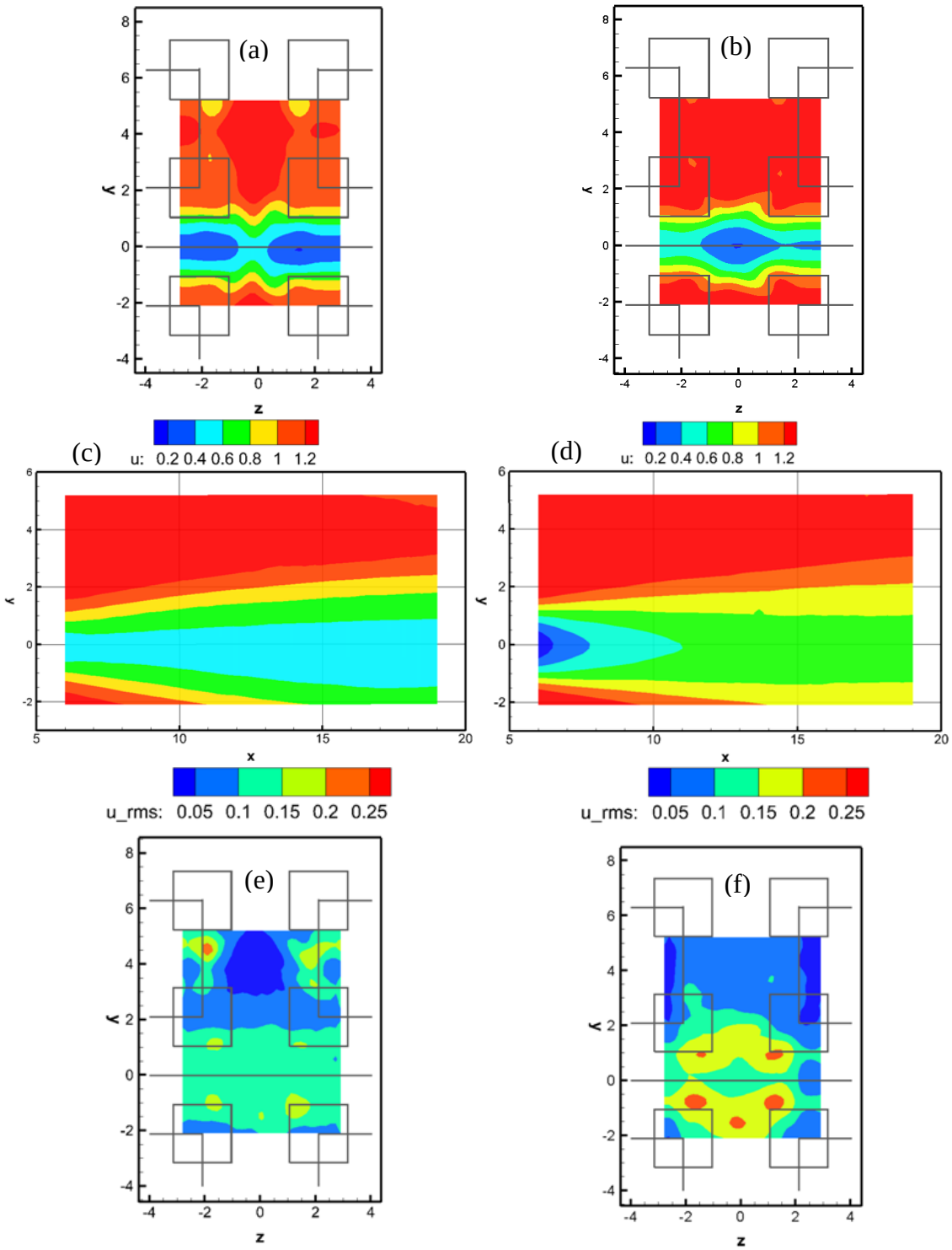

Figure 3-16: $\frac{U}{U_0}$ at x=6.5 for (a) FG105 and (b) FG305. $\frac{U}{U_0}$ at z=0 for (c) FG105 and (d) FG305. $\frac{u_{rms}}{U_0}$ at x=9 for (e) FG105 and (f) FG305

Important differences in the flow fields of FG105 and FG305 are shown in Figures 3-16 through Figure 3-19. Results from FG105 and FG305 are non-dimensionalised by freestream velocities of 0.039m/s and 0.115m/s, respectively. The results in this section have x, y, and z non-dimensionalised by d_0 (bar thickness of iteration 0). Note, more complete results from TPIV of FG105 are shown in Appendix A. Figure 3-16 shows differences in the streamwise velocity component. Comparison of Figure 3-16 (a) and (b) show that the largest deficits in the wake (dark blue contours) occur at opposite spanwise locations. Figure 3-16 (a) shows U/U_0 is lower in the wake of iterations 2 and 3 but again symmetry is observed over y=0 and z=0. In Figure 3-16 (d) of U/U_0 at z=0, the flow deficit is smaller than in Figure 3-16 (c). For FG105, U/U_0 remains smaller further downstream as seen by the light blue contours spanwise across the field. In both cases, the shear layer is seen in the region where U/U_0 contours vary from yellow to red in y. In Figure 3-16 (e), smaller u_{rms}/U_0 values are seen at the corners of iteration 3 near z=0 than for FG305. However, larger fluctuations are observed downstream of iteration 2 for y greater than 2. This suggests flow interactions between the smaller iterations away from the thickest beam are propagated further downstream for a slower freestream velocity.

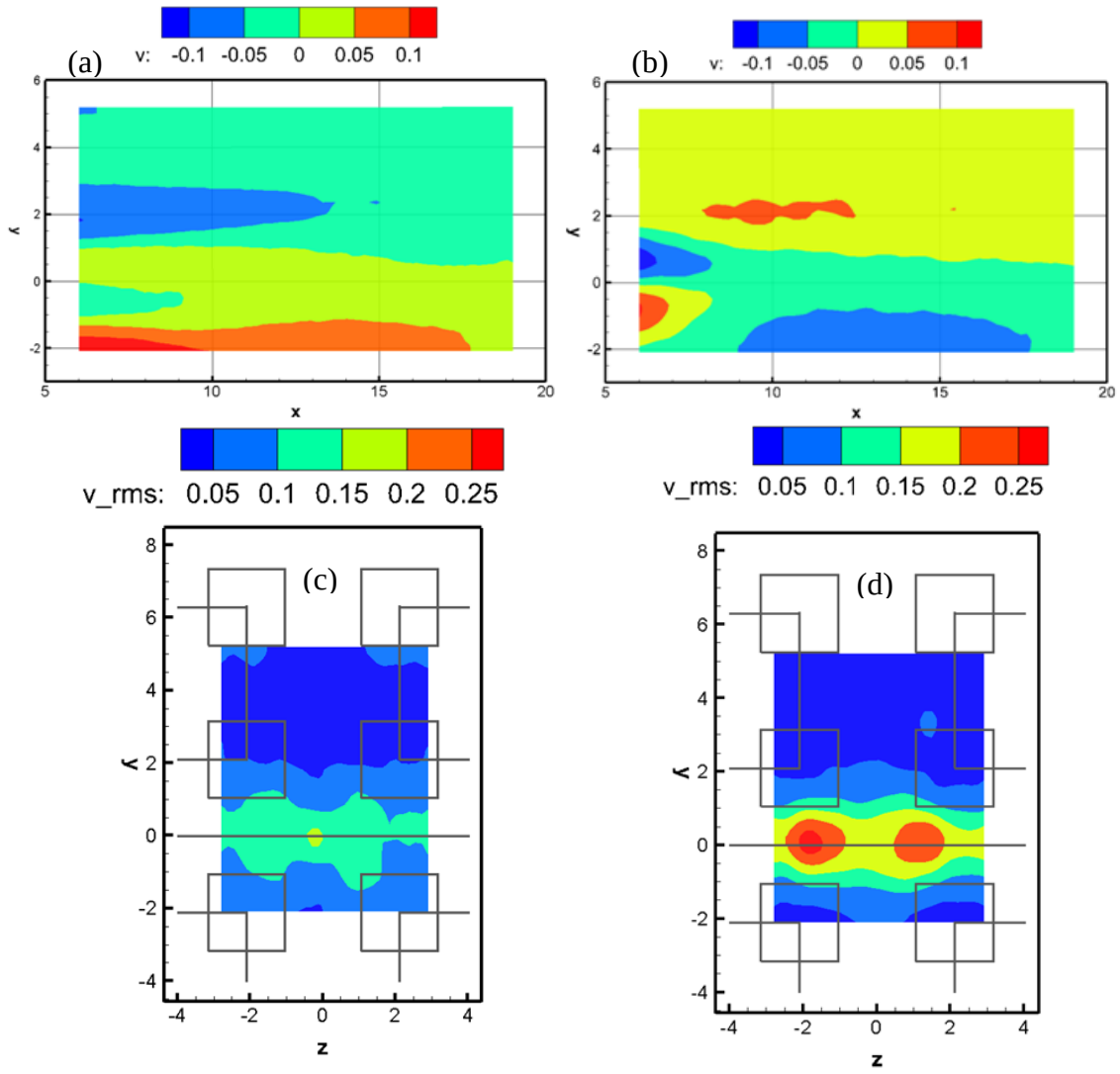

Figure 3-17: $\frac{V}{U_0}$ at z=0 for (a) FG105 and (b) FG305. $\frac{v_{rms}}{U_0}$ at x=6.5 for (c) FG105 and (d) FG305

In Figure 3-17 (a) and (b), almost opposite behavior is observed in V/U_0 for FG105 and FG305. In the near wake for FG305, the flow converges in the wall normal direction to zero, but for FG105 the flow is opposite in direction although less in magnitude. V/U_0 for y greater than 1.5 is positive for FG305 but negative for FG105, and for y less than 0, V/U_0 is positive for FG105 but negative for FG305. Figure 3-17 (c) and (d) compares v_{rms}/U_0 for FG105 and FG305 and show that higher fluctuations occur for FG305. However, FG105 has slightly higher fluctuations downstream of the smaller iterations.

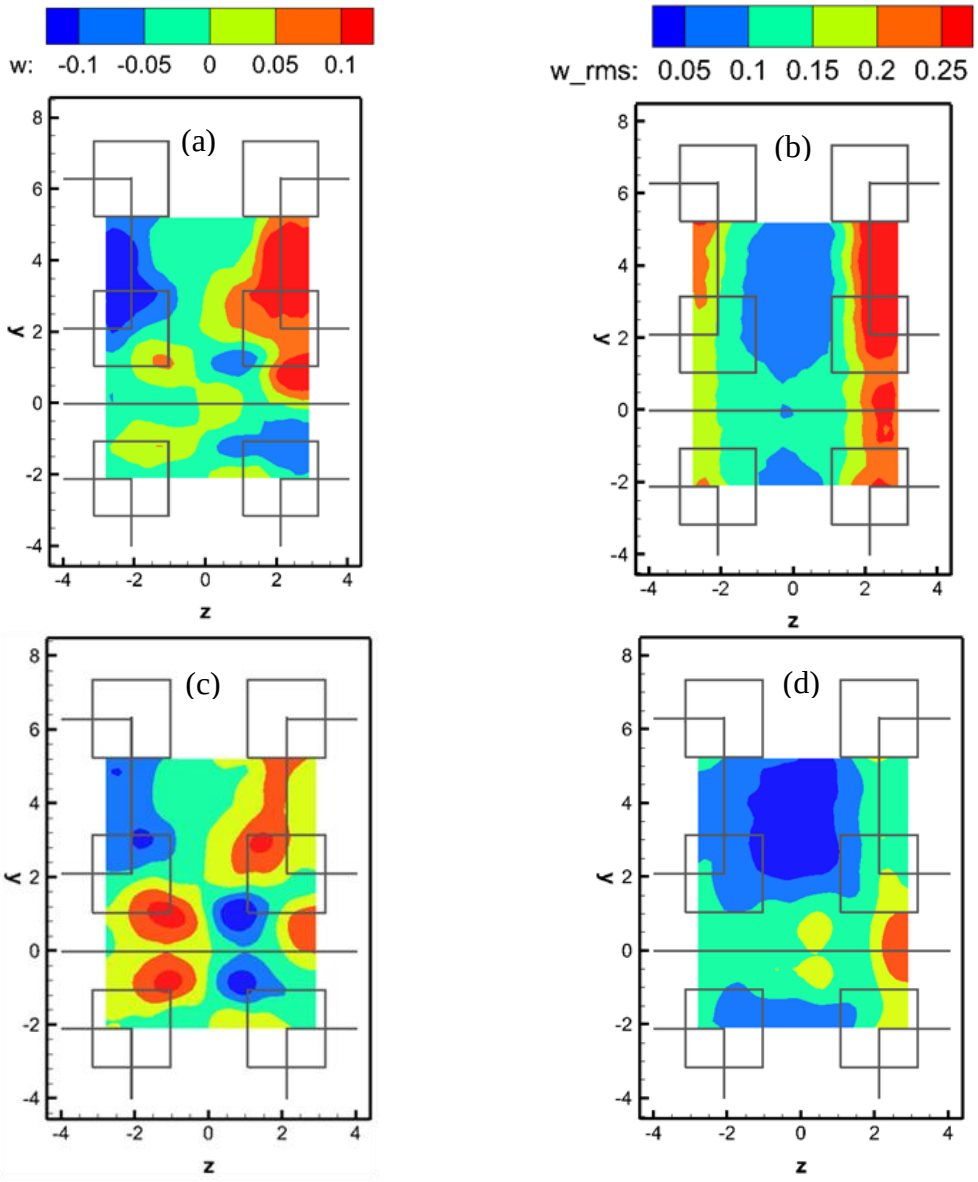

Figure 3-18: $\frac{W}{U_0}$ at x=6.5 for (a) FG105 and (c) FG305. $\frac{w_{rms}}{U_0}$ at x=6.5 for (b) FG105 and (d) FG305

In Figure 3-18 (a) and (c), W/U_0 is shown for FG105 and FG305, respectively. For FG305 at y less than 2, W was found to converge strongly towards z=0 which is observed in FG105 but not as strong. For y greater than 2, W is observed to diverge stronger in FG105 than FG305. In Figure 3-18 (b), w_{rms}/U_0 for $|z|$ greater than 2 is found to be greater for FG105 than FG305. The results from Figure 3-18 show that away from iteration 0 the thinner bars have larger affect.

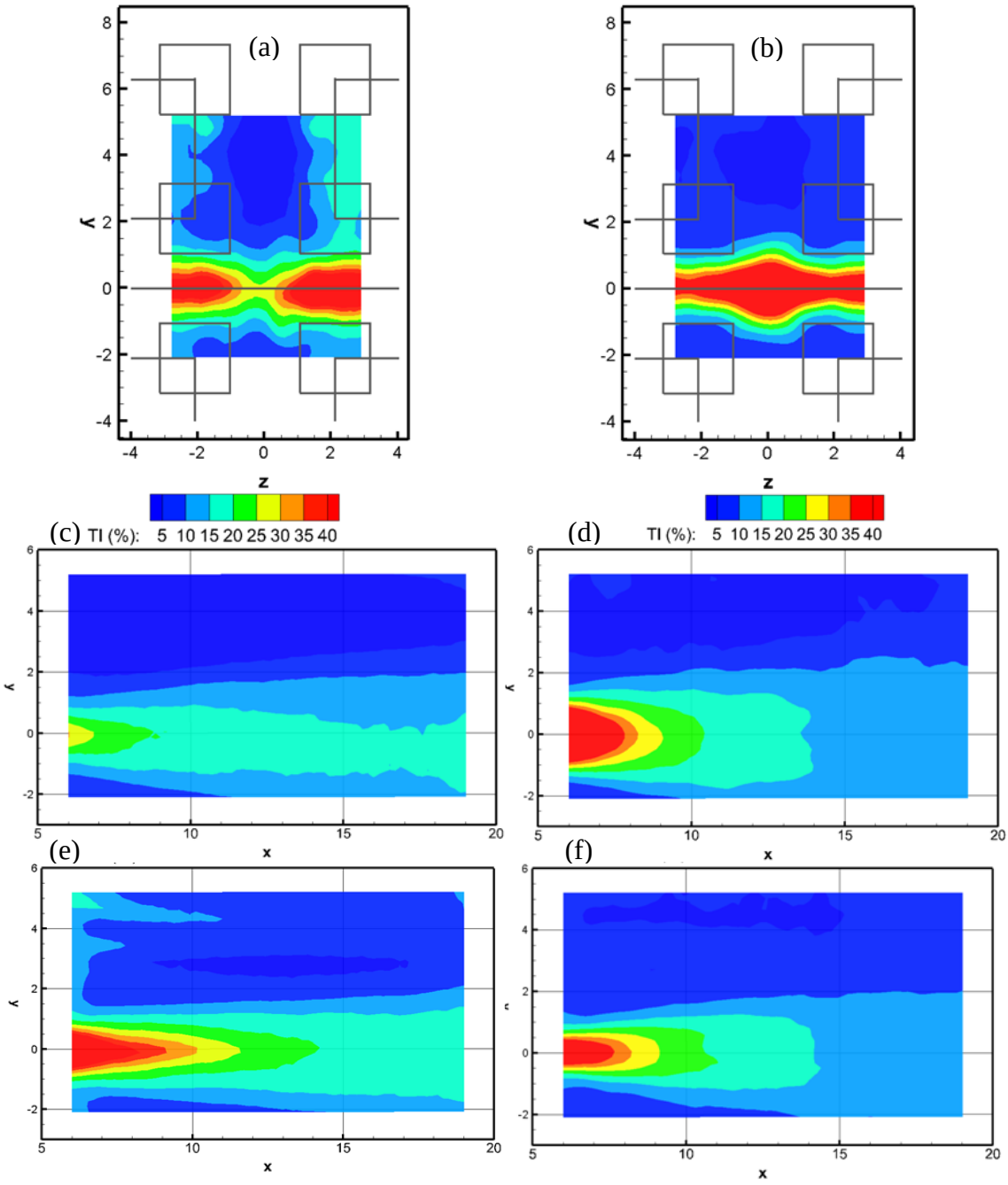

Figure 3-19: TI as percentage at x=6.5 for (a) FG105 and (b) FG305, at z=0 for (c) FG105 and (d) FG305, and at z=1.4 for (e) FG105 and (f) FG305

In Figure 3-19, TI is compared for FG105 and FG305. Figure 3-19 (a) and (b) show larger TI downstream of iterations 2 and 3 for FG105 than FG305 and much smaller TI at z=0 for FG105. This result is confirmed by Figure 3-19 (c) and (d) where

in the near wake larger TI are found for FG305 but further downstream along y=0 larger TI are actually observed for FG105. Turbulence intensities were found to exceed 95% for FG305 while only reaching 65% for FG105. Overall from the comparison of FG105 and FG305, it appears that the smaller iterations in FG105 create larger relative velocity fluctuations. Also, FG305 has larger flow deficit in the wake of iteration 0 but FG105 has a longer streamwise length of the wake.

For further insight into the flow downstream of the fractal grid, the Reynolds number of each iteration can be calculated by $Re_i = U_0 d_i/\nu$. Although the bars have rectangular geometries, these Reynolds numbers can be compared to known regimes of a cylinder in cross flow from Blevins (1990). For FG305, iteration 0 has a Reynolds number of ~500 which is in the turbulent regime where strong and periodic vortex shedding occurs. For FG105, iteration 0 has a Reynolds number of ~175 which is in the transitional regime where vortex shedding occurs but with occasional irregular disturbances. This explains the larger turbulence observed in the wake of iteration 0 for FG305 (see Figure 3-19). For FG305, iteration 2 and 3 have a Reynolds number of ~125 and ~75, respectively, which are both in the laminar regime where periodic staggered vortices of opposite signs occur (von Karman vortices). For FG105, iteration 2 has a Reynolds number of ~45 where flow is laminar and von Karman vortices begin to shed. For FG105, iteration 3 has a Reynolds number of ~25 where flow separates from the trailing edge and vortices are present in the near wake but not shed. Therefore, the nature of the shedding is likely different in the two flows. From Figure 3-19, larger relative turbulence levels are observed downstream of iterations 2 and 3 in FG105 although Reynolds numbers are larger for FG305. For FG305 with iterations 2 and 3, the laminar vortices that are shed must dissipate quicker due to the faster freestream. For FG105, the slower freestream must allow the shed vortices to propagate further downstream. The differences in U/U_0 are observed in Figure 3-16 where FG305 had larger values of U/U_0 throughout the measurement volume. However, this basic model does not account for flow interactions between bars which could be the source of the higher turbulence observed downstream of iterations 2 and 3 for FG105. Moreover, iteration 1, which is

not directly upstream, could also interact with the other iterations and contribute to the results observed for FG105 and FG305.

3.2.1.4. MPSR of FG305 flow field

As previously discussed, large values of MPSR have been shown to elicit escape behavior in copepods. Therefore, MPSR values generated downstream of the fractal grid were investigated. The MPSR probability distributions for TPIV and SPIV are shown in Figure 3-20. Experiments with copepods were performed with SPIV at the center plane so gradients in z could not be calculated. Therefore, the relationship between 2D MPSR and 3D MPSR was investigated. This means the deformation rate tensor in Equation (1-1) becomes a 2x2 matrix where only gradients of u, v, x, and y are considered. This implies that local values of 3D MPSR will be larger than 2D MPSR. In Figure 3-20, the blue line shows the probability distribution of 3D MPSR for the entire measurement volume. The green line is the 3D MPSR calculated at the center plane. Both 3D MPSR distributions have similar shape. The full volume MPSR shows larger populations in the range of 2.5-10s^{-1} which are a result of the flow interactions downstream of iterations 1, 2 and 3. 2D MPSR values were calculated at the center plane for TPIV (black line) and SPIV (red line) results. These probability distributions show similar results as expected since the spatial resolutions were very similar in the two data sets.

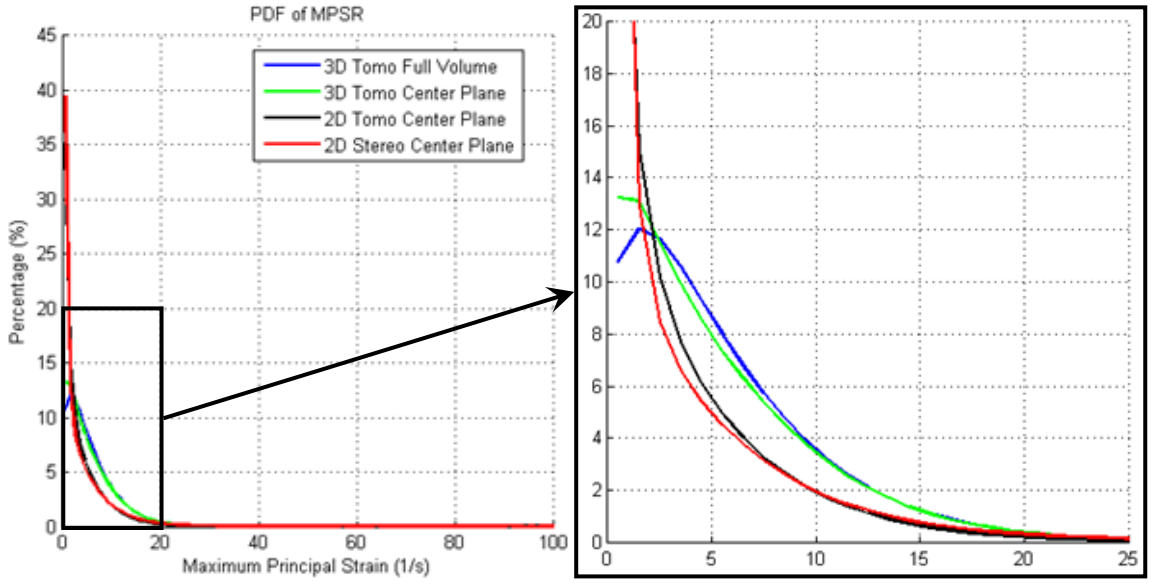

Figure 3-20: The MPSR probability distribution from FG305 of 3D full volume (blue), 3D center plane (green), 2D center plane from tomographic PIV (black), and 2D center plane from stereo PIV (red)

Only instantaneous 2D MPSR for copepods near the center plane can be found. Therefore, finding a relationship between 3D MPSR and 2D MPSR at the center plane would be beneficial. For TPIV results, 2D MPSR and 3D MPSR values are found at each data point in the center plane. A portion of this data is plotted as black dots in Figure 3-21 (a). In green, the average 3D MPSR is found for a given 2D MPSR value. In magenta, a second order polynomial fit of the averaged data was found for 2D MPSR values less than $50s^{-1}$. The 3D MPSR to 2D MPSR relation is

$$MPSR_{3D} = 0.005(MPSR_{2D})^2 + 0.83MPSR_{2D} + 2.62. \quad (3\text{-}2)$$

Note all data is above the red dashed line in Figure 3-21 (a) which shows all 3D MPSR values are larger than or equal to their corresponding 2D MPSR values. A probability distribution contour is seen in Figure 3-21 (b). This shows that almost all of the 2D MPSR and corresponding 3D MPSR values are less than $15s^{-1}$. In this range, the average 3D MPSR value is about 50% larger than the average 2D MPSR value.

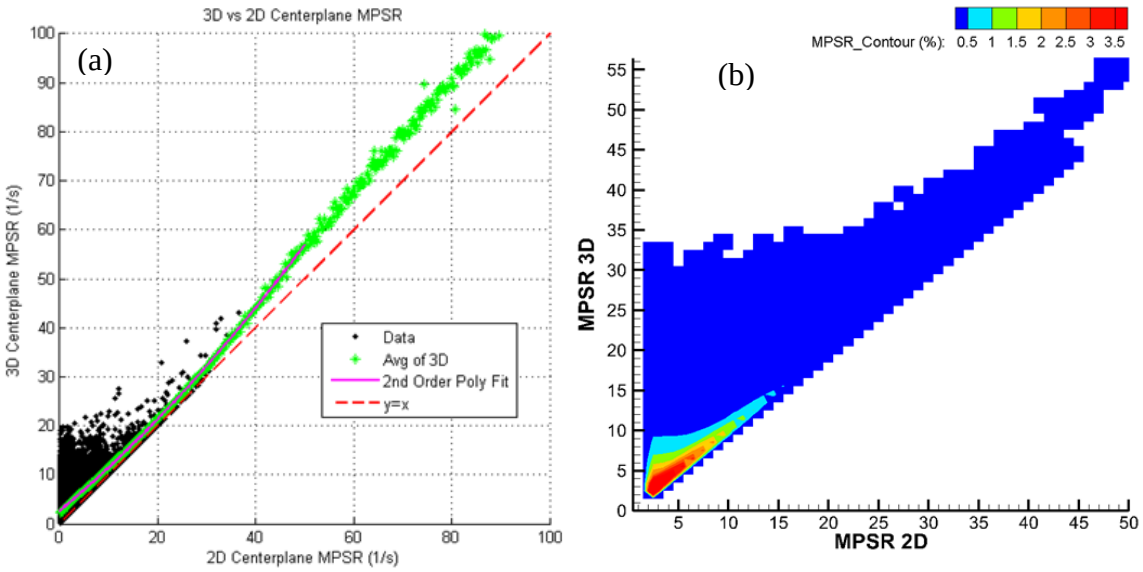

Figure 3-21: From FG305, the 3D vs 2D MPSR for the center plane of the same data are plotted in (a) with partial data (black), average of 3D MPSR (green), and second order polynomial fit (magenta). In (b), the probability distribution of the 3D vs 2D MPSR is shown

To gain a better understanding of the strain rate downstream a fractal grid, 2 fields of instantaneous 3D MPSR results at x=6.5 and x=9 are examined in Figure 3-22 (a)-(d). From these results, we see instantaneous values exceeding 25s^{-1}occurring in the near wake of iteration 0 and dissipating further downstream. We also see higher MPSR in the wake of iterations 2 and 3 but the strong MPSR locations fall within $|y|$<2 at these x locations. From these instantaneous fields in the wake of iteration 0, it is observed by the green contours that at most locations the instantaneous MPSR exceeds 10s^{-1}, which is greater than thresholds previously found to elicit copepod escape (Kiørboe *et al*. (1999), Buskey *et al*. (2002), etc.). Figure 3-22 (e) and (f) show the mean 3D MPSR for these x locations. At x=6.5 in the wake of iteration 0, the mean 3D MPSR is found to be greater than 10s^{-1} which means a large amount of copepod response is expected in this region. In the wake of iteration 2 and 3, the average 3D MPSR is found to be greater than 4s^{-1} which is also greater than some thresholds previously found to cause copepod escape (Adhikari (2013)). From this analysis, it is expected that FG305 will be successful in eliciting copepod escape. From Figure 3-22 (a)-(d), it is observed that the instantaneous MPSR can vary across the spanwise direction. Therefore, when looking at the instantaneous MPSR at the center plane near the copepod location, limitations in the

spanwise direction of the copepod location must be considered. These limitations will be discussed in Section 3.6 with discussion of MPSR during copepod escape.

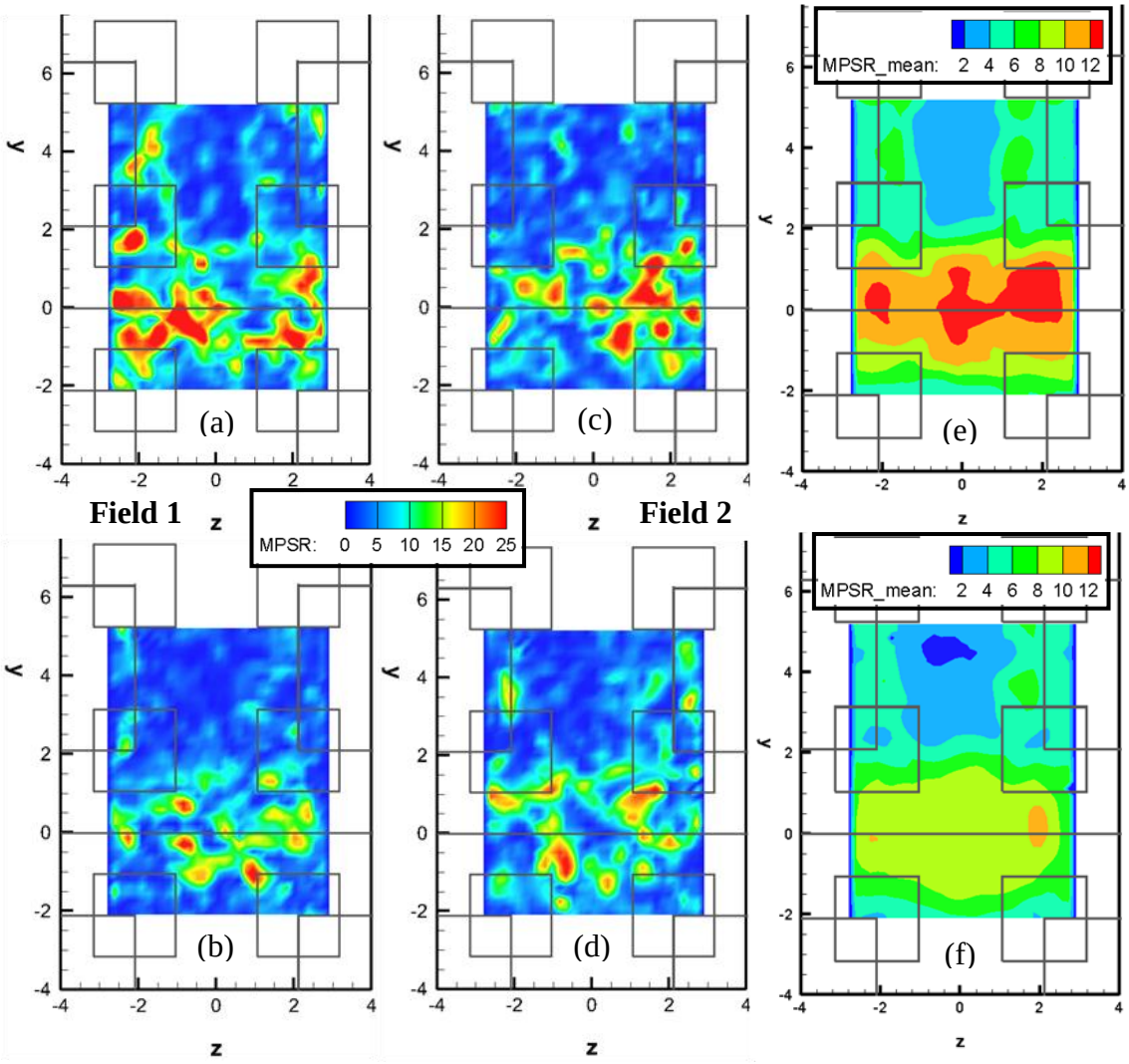

Figure 3-22: From FG305, x cross sections of instantaneous fields of 3D MPSR (1/s) for field 1 at x=6.5 (a) and x=9 (b) and field 2 at x=6.5 (c) and x=9. For FG305, x cross sections of mean 3D MPSR (1/s) at x=6.5 (e) and x = 9 (f)

3.2.2. Downstream horizontal cylinder

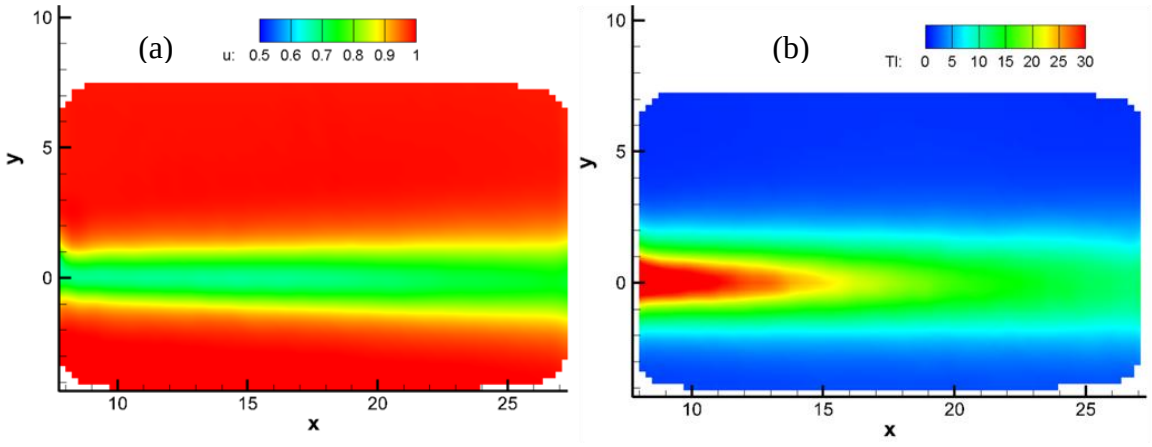

Figure 3-23: (a) $\frac{U}{U_0}$ and (b) TI as percentage for HC305

Experiments were performed downstream of a wall mounted horizontal cylinder for comparison to downstream the fractal grid. The results from 1000 independent samples are found in Figure 3-23 where x and y are non-dimensionalised by the cylinder diameter, d_c, which matches the bar thickness of iteration 0. x=0 is the trailing edge of the cylinder and y=0 is the center of the cylinder. The Reynolds number based on cylinder diameter for HC105 is about 125. In this regime, Blevins (1990) predicts laminar von Karman vortices which were observed. For HC305, the Reynolds number is about 360 where fully turbulent vortex shedding is observed. Figure 3-23 (a) shows streamwise flow is not accelerated to a speed greater than U_0, as was the case for the fractal grid. Figure 3-23 (b) shows that turbulence is only seen downstream of the cylinder where turbulence intensities were found to be a maximum of 40%. This is much lower than downstream the fractal grid for the same freestream speed where turbulence intensities were found to exceed 95%. This shows that the fractal grid generated more turbulence. For the same freestream speed from SPIV results, the mean 2D MPSR downstream of the horizontal cylinder was found to be about 50% of the mean 2D MPSR downstream the fractal grid at z=0. Therefore, it is expected that there will be a lower copepod escape frequency downstream the horizontal cylinder.

3.3. Escape criteria

To quantitatively determine if a copepod has jumped, criteria based off of copepod position and velocity must be set. As discussed in Section 2.3.4, there is an inherent amount of noise in the z direction of the 3D-PTV measurement system from changing copepod shape. Therefore, several criteria will be used to accurately identify copepod jumps. First, DaVis outputs velocity vectors of the copepod for a given location. Then code was implemented to assign an identification number to each individual copepod track. In Adhikari (2013), escape was considered when there was more than a 15% change in copepod speed between two consecutive time steps. This will be the first escape criterion used. For FG305, a track of one copepod that exhibits two jumps is seen in Figure 3-24. Figure 3-24 (a) shows the position of the copepod where the location of the first jump is identified in red and the second in green. Figure 3-24 (b) shows the velocity magnitude, $\|\overrightarrow{v_c}\|$, of the copepod versus time where $\overrightarrow{v_c} = u_c\hat{\imath} + v_c\hat{\jmath} + w_c\hat{k}$. There are two large spikes corresponding with the first and second jumps. The jump is determined when $v_{diff} = \|\overrightarrow{v_{c,n+1}}\| - \|\overrightarrow{v_{c,n}}\| > 0.15\|\overrightarrow{v_{c,n}}\|$. This is plotted in Figure 3-24 (c) where the exact escape time is considered once $v_{diff}/\|\overrightarrow{v_{c,n}}\| > 0.15$. In Figure 3-24 (b), there is some noise in $\|\overrightarrow{v_c}\|$. This noise is amplified when a derivative is taken, as seen in Figure 3-24(c). Therefore, this should not be the only criterion used to determine copepod jumps.

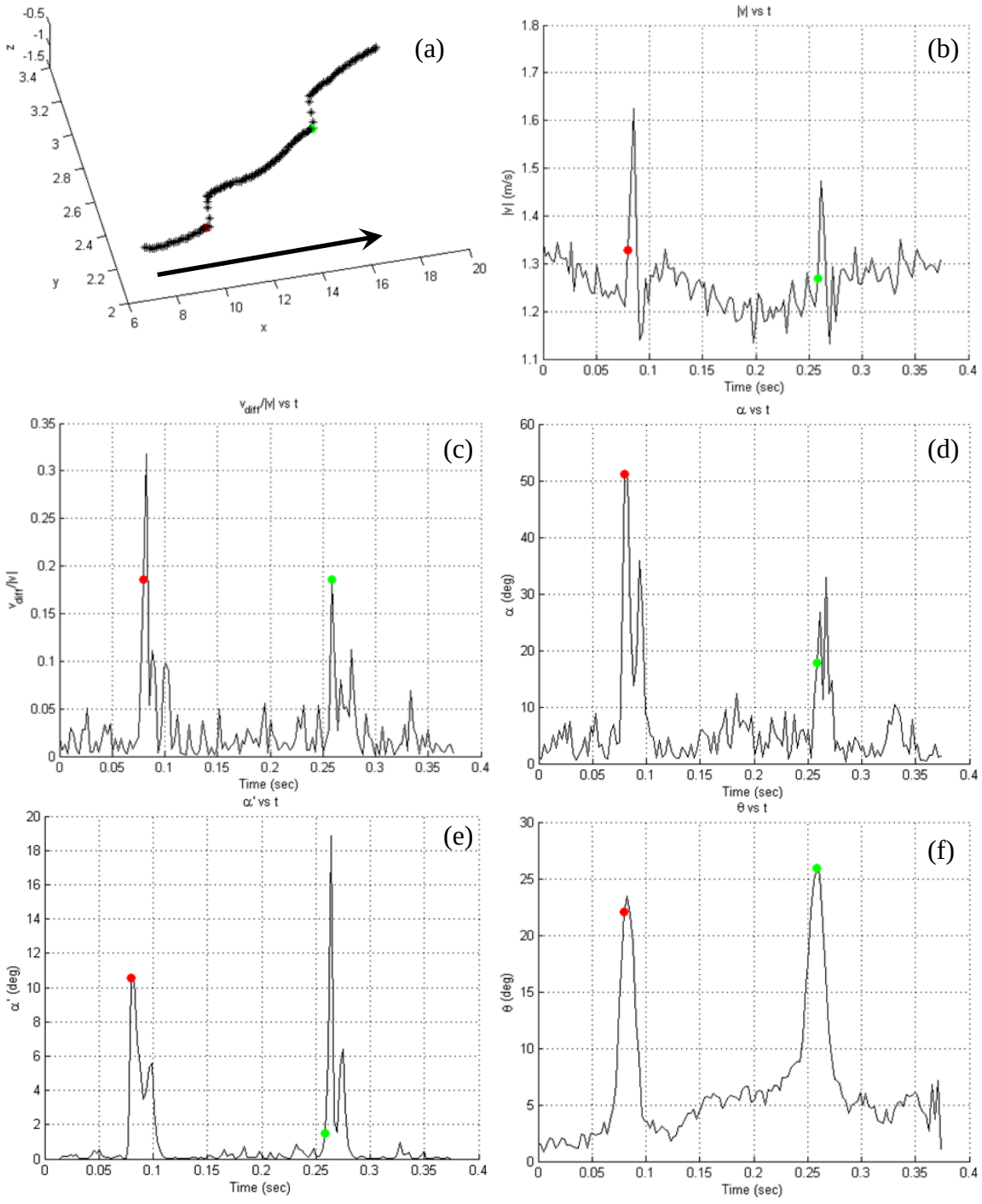

Figure 3-24: Track of single copepod for FG305 exhibiting two escapes. (a) shows the spatial locations of the track where the black arrow shows the flow direction and the red dot is the first escape and the green dot is the second escape. (b) shows $|v|$, (c) shows the velocity difference with forward difference, (d) shows α, (e) shows α', and (f) shows θ

In addition to copepods having a change in velocity magnitude, they also have a change in direction during a jump. This can be determined using a dot product between two consecutive time steps, which is seen by

$$\overrightarrow{v_{c,n+1}} \cdot \overrightarrow{v_{c,n}} = \left\|\overrightarrow{v_{c,n+1}}\right\| \left\|\overrightarrow{v_{c,n}}\right\| \cos\alpha. \tag{3-3}$$

The resulting angle, α, can be seen in Figure 3-24 (d). This result shows large peaks during escape but with a considerable amount of noise. For example, between jumps the angle exceeds 10°. Although the flow can be turbulent, this noise results from inaccuracies in the 3D-PTV measurement system, and it is not physical for the copepod to have that large of a direction change during drift. Therefore, it is beneficial to use an averaging technique to smooth noise. This was done by using a quantity α' which can be seen in Figure 3-24 (e). In this quantity, each component in $\overrightarrow{v_{c,n}}$ and $\overrightarrow{v_{c,n+1}}$ is averaged over 5 previous time steps and then a dot product is taken. This reduces noise during drift, but α' still retains peaks during escape behavior. $\alpha' > 5°$ within 0.02s of the escape instance as determined from the $v_{diff}/\left\|\overrightarrow{v_{c,n}}\right\| > 0.15$ criterion was the threshold used.

From Figure 3-24 (a), it is observed that there can be a sharp change in y and z location during escape. A third criterion to capture this was

$$\begin{aligned}\theta &= \sin^{-1}\left(\frac{\sqrt{dy^2 + dz^2}}{\sqrt{dx^2 + dy^2 + dz^2}}\right) \\ &= \sin^{-1}\left(\frac{\sqrt{\left(y_{n+p} - y_n\right)^2 + \left(z_{n+p} - z_n\right)^2}}{\sqrt{\left(x_{n+p} - x_n\right)^2 + \left(y_{n+p} - y_n\right)^2 + \left(z_{n+p} - z_n\right)^2}}\right)\end{aligned} \tag{3-4}$$

where dx, dy, and dz are the copepod position change in the x, y, and z directions, respectively. p, the forward time step integer, was chosen to be 6 time steps as this gave large θ during escape but small θ during copepod drift. The third and final escape confirmation parameter was a threshold of $\theta_{max} > 14.5°$ where θ_{max} is the maximum θ within 0.02s of the escape instance. This final escape confirmation was effective as copepods were almost never found to jump in the positive streamwise direction. The results of these thresholds were visually confirmed.

To confirm the level of accuracy of the thresholds in the escape criteria, data runs for select sets were analyzed. This was done by visually confirming escapes predicted by

the code with observation of the copepod jumping in the raw video. The thresholds mentioned previously were selected to maximize this visual confirmation percentage. This was performed for one data run of FG105 (43.8s) where 39 of 43, or 90.7%, copepod jumps were visually confirmed. Also, confirmation of one data run of FG305 (14.6s) resulted in 69 of 75, or 92%, of copepod jumps being visually confirmed. This means the overall accuracy of the code was 91.5% downstream of the fractal grid. This means approximately 8% of the escapes identified by the code were not actual escapes. For some cases, this was a result of two copepod trajectories intersecting, which resulted in DaVis calculating erroneous vectors in the 3D-PTV algorithm. For other cases, this error came from different projections of the copepod on each camera as discussed in Section 2.3.4. The same code and thresholds were used to determine escape downstream of the horizontal cylinder.

3.4. Escape and track results

The previously discussed escape criteria were applied to all of the data sets in Table 3-1. These results for the freestream, upstream and downstream of the fractal grid, and downstream of the horizontal cylinder will be discussed in this section. For this section, a track refers to a consecutive time-series measurement of one copepod for a minimum of 20 consecutive images. However, tracks for one copepod could be up to 200 consecutive images. Many were around 100 consecutive images. This large range depended how long they were in the measurement volume. Copepods could drift into and out of the measurement volume due to the flow or jump in or out while exhibiting an escape response.

3.4.1. Uniform flow

Copepods were examined in freestream flow as a control for copepod response within the water channel. This is useful for comparison to downstream the fractal grid and horizontal cylinder. F1 had 8.3% escape response, and F3 had 0% escape response. Escape response is calculated from dividing the copepods that responded by total number

of copepods tracked within the measurement volume. These results were visually confirmed as previously discussed. As previously discussed, F1 has lower absolute levels of root mean square velocity fluctuations than F3 where both levels are small. Therefore, the higher copepod escape behavior for F1 is most likely a result of slower U_0. This copepod behavior is most likely not response to strain rate in the flow but is the copepod reorienting itself. This reorientation could be the copepod trying to feed on algae also within the channel. Feeding could be easier for the copepod at F1 as this slower flow resembles the conditions they have adapted to in a lake. In addition, the copepod may feel the need to reorient themselves due to not being a perfectly passive particle and wanting to counter the gradual sinking at a slower freestream speed. This reorientation behavior will be discussed in greater detail in Section 3.4.4 where the relative copepod Reynolds number is analyzed.

3.4.2. Fractal grid

The main focus of this study was downstream the fractal grid. However, it is important to take consideration of copepod behavior upstream of the fractal grid. While performing experiments, the majority of copepods were observed visually to jump less than 1cm before passing through the grid. Some copepods were even observed to exhibit multiple jumps. However, upstream of this region there was no copepod response. Due to the horizontal camera arrangement, this volume directly upstream could not be resolved as the grid blocked the views of the cameras placed at an angle to the spanwise direction. These upstream jumps appear similar to those observed upstream of a cylinder by Adhikari (2013).

The track and escape results downstream of the fractal grid for freestream speeds of 0.039m/s and 0.115m/s are found in Table 3-2 and Table 3-3, respectively. For both freestream speeds, a maximum of 5 jumps per copepod were observed. The escape percentage in the final column is the number of copepods that jumped (1st Jump) divided by the number of tracks. Comparing the results of both freestream speeds, similar track numbers are found at the same locations, but for normalized comparison, escape

percentage will be examined. For U_0 =0.039m/s, the escape percentage is largest immediately downstream of the grid and decreases going away from the grid until it reaches a minimum at FG112. Then the escape percentage increases for FG120 and FG140. The two highest escape percentages are for FG105 and FG108 which makes sense as these regions have higher turbulence and therefore larger strain rates. Further downstream at FG120 and FG 140, it is expected that the escape percentage would decrease, but this is not the case. Instead, the escape percentages at FG120 and FG140 are similar to results from F1 (escape percentage of 8.3%). This implies that jumps at FG120 and FG140 are most likely the copepods reorienting themselves and not in response to strain rate.

Table 3-2: Track and escape results downstream fractal grid where U_0 =0.039m/s

Data Set	**Tracks**	**1st Jump**	**2nd Jump**	**3rd Jump**	**4th Jump**	**5th Jump**	**Total Escapes**	**Escape %**
FG105	929	123	43	21	7	2	196	13.24
FG108	401	47	12	5	4	1	69	11.72
FG112	100	4	1	0	0	0	5	4
FG120	109	9	3	1	0	0	13	8.25
FG140	363	27	5	2	1	0	35	7.44
TOTAL	**1902**	**210**	**64**	**29**	**12**	**3**	**318**	**11.04**

In Table 3-3 for U_0 =0.115m/s, we see the highest escape percentage closest to the grid and decreasing values further downstream. This follows the expected trend of fewer escapes at smaller strain rates. The highest escape percentage for all experiments is at FG305, which is expected as this location and condition has the largest MPSR values. The other locations for U_0 =0.115m/s have much lower escape percentage. This is expected as the escape percentage was zero for F3, so the small number of escapes for FG308 through FG340 is copepod response to the smaller turbulence.

Table 3-3: Track and escape results downstream fractal grid where U_0 =0.115m/s

Data Set	Tracks	1st Jump	2nd Jump	3rd Jump	4th Jump	5th Jump	Total Escapes	Escape %
FG305	1192	182	54	15	6	2	259	15.27
FG308	408	25	3	0	0	0	28	6.13
FG312	99	4	1	0	0	0	5	4.04
FG320	157	5	0	0	0	0	5	3.18
FG340	273	5	0	0	0	0	5	1.83
TOTAL	**2129**	**221**	**58**	**15**	**6**	**2**	**302**	**10.38**

Comparing Table 3-2 and Table 3-3, the escape percentage is larger at FG108 than at FG308. This might be a result of turbulence decaying quicker for U_0 =0.115m/s as seen from Figure 3-19. In Figure 3-19, TI decays quicker in the streamwise direction for FG305 than FG105 in the wake of the thickest beam (iteration 0). For both FG112 and FG312, the escape percentage is 4%. This may not accurately represent copepod response in this region as there was not much data collected at this location. Overall, there is a slightly larger escape percentage at U_0=0.039m/s which is most likely a result of copepod reorientation further downstream of the grid. However, as expected, the escape percentage is greater at FG305 than FG105 as strain rates are larger. The escape percentage shows only the ratio of copepods that responded to the total number of copepods. It is important to note that for U_0=0.039m/s there was a larger percentage of second, third, fourth and fifth jumps than for U_0=0.115m/s. This suggests that for a slower freestream, copepods are more likely to exhibit multiple jumps.

3.4.3. Downstream horizontal cylinder

The escape and track results downstream the horizontal cylinder are seen in Table 3-4 and Table 3-5. For comparison, Adhikari (2013) performed several experiments with U_0 of 0.038m/s, 0.077m/s, and 0.115m/s where the cylinder diameter was 6.35mm or 12.7mm. Adhikari (2013) found lower copepod populations downstream of a wall-normal cylinder in cross flow compared with spanwise locations outside the cylinder

diameter. This was most likely a result of copepod response to MPSR and sudden deceleration upstream of the cylinder, which resulted in the copepods jumping away from the cylinder in the spanwise direction. Adhikari (2013) also found that few copepods responded in the wake of a cylinder even when MPSR values far exceeded those that created response upstream of the cylinder. Both HC105 and HC305 were found to have low escape percentages and small copepod populations in the wake of the cylinder. It was observed that for HC105 the escape percentage is similar to F1. Therefore, the response at HC105 is most likely not due to higher MPSR values seen in the wake of the cylinder but is copepod reorientation at the slower freestream speed which will be discussed in greater detail in Section 3.4.4. For HC305, a very small escape percentage was found (1.5%) which is very similar to F3 (0%). This is most likely due to the copepods jumping away from y=0 upstream of the cylinder, which results in a smaller copepod population in the cylinder wake. The small escape percentage seen at HC305 shows that some copepods jumped in the cylinder wake, but the escape percentage was much lower than for FG305. As previously mentioned in Section 3.2.2, the mean 2D MPSR calculated for HC305 was about 50% of FG305. In addition, the wake thickness (wall-normal length) was slightly smaller for HC305 than FG305. This resulted in much lower copepod escape frequency for HC305 than FG305. The results of Table 3-5 are consistent with low copepod response in the wake of a cylinder found by Adhikari (2013).

Table 3-4: Track and escape results for HC105

Data Set	Tracks	1st Jump	2nd Jump	3rd Jump	4th Jump	5th Jump	Total Escapes	Escape %
HC105	120	9	2	2	1	0	14	7.5
TOTAL	**120**	**9**	**2**	**2**	**1**	**0**	**14**	**7.5**

Table 3-5: Track and escape results for HC305

Data Set	Tracks	1st Jump	2nd Jump	3rd Jump	4th Jump	5th Jump	Total Escapes	Escape %
HC305	391	3	2	1	0	0	6	1.53
TOTAL	**391**	**3**	**2**	**1**	**0**	**0**	**6**	**1.53**

3.4.4. Reynolds number scaling

It was found at U_0=0.039m/s (F1) that copepods executed jumps not necessarily in response to MPSR but to reorient themselves. To further analyze this behavior, the Reynolds number from a magnitude of slip velocity and copepod length can be calculated by $Re = \|\overrightarrow{v_{c,slip}}\|L_c/\nu$ as discussed in Section 1.2.1. For this study, the slip velocity is calculated by subtracting the mean flow of each component from the copepod velocity at that copepod location. Catton *et al.* (2006 and 2012) examined two different swimming modes, cruise and escape, in different species of Euchaeta. PPIV experiments were performed in still water where escape response was initiated with visible laser pulses. During cruise, the second antennae are used for propulsion, while the first antennae and swimming legs are used for propulsion during escape. For L_c=4.6mm, Catton *et al.* (2006) found a cruising Reynolds number of 12 and escape Reynolds number of 105. This shows the copepod is in a more viscous dominated regime during cruise and inertia dominated regime during escape. For an average copepod length of 2.4mm, Catton *et al.* (2012) found a cruising Reynolds number of 25 and escape Reynolds number of 680. This shows that for different species, the Reynolds number can vary for each swimming mode. However, during escape copepods are in an inertia dominated regime while during cruise viscosity has a larger effect.

To compare the results of this study to these two swimming modes from Catton *et al.* (2006 & 2012), the Reynolds number was investigated. This was done by finding the maximum $\|\overrightarrow{v_{c,slip}}\|$ immediately after escape. To investigate the reorientation jumps, this maximum $\|\overrightarrow{v_{c,slip}}\|$ for escapes of F1 and HC105 (not in wake of cylinder) was found. The corresponding averaged Reynolds number was ~40, where the copepod length was assumed to be 1mm. The minimum and maximum Reynolds numbers found for this data were 5 and 120, respectively. The average copepod slip velocity found was 0.04m/s. The escapes in FG305 are likely copepod response to turbulence. Therefore, the maximum $\|\overrightarrow{v_{c,slip}}\|$ for each escape at FG305 was found, where the average was 0.14m/s. This corresponds to a Reynolds number of ~140, where the minimum and maximum were 35 and 315, respectively. In comparison to results from Catton *et al.* (2006 &

2012), the reorientation jumps (Re ~40) appear to be in cruise behavior, while jumps in regions of higher turbulence and MPSR match escape behavior (Re ~140).

3.5. Copepod results downstream of fractal grid for FG305

All analysis for this section is for FG305 as this data set had the largest escape percentage and there is three dimensional knowledge of the flow in this region. In this section, the spatial copepod track and escape distribution, escape direction, and escape magnitude will be discussed.

3.5.1. Copepod track and escape distribution

Figure 3-25 shows the probability distribution of the copepod tracks versus x, y, and z non-dimensionalised by d_0 where all figures had a bin width of $0.5d_0$. As expected, Figure 3-25 (a) shows even distribution across the streamwise direction of the measurement volume. The smaller population on the ends is not physical and is a result of the 3D-PTV measurement system not being able to triangulate the copepods as well as the center. Figure 3-25 (b) where y is on the vertical axis and the probability distribution is on the horizontal axis, shows lower copepod populations downstream of the thickest bar and below iteration 0. The copepod population increases with increasing y. This means that either more copepods passed through the center of the fractal grid than below iteration 0, or that the copepods that jump, jump in the positive y direction. This will be investigated more in Section 3.5.2 when the escape direction is analyzed. Figure 3-25 (c) shows the copepod probability distribution with respect to z. There is a slightly larger copepod population seen in z greater than zero. This is interesting as the grid and resulting flow are symmetric over the z axis. Overall, knowledge of where copepods are is necessary in analyzing where they escape.

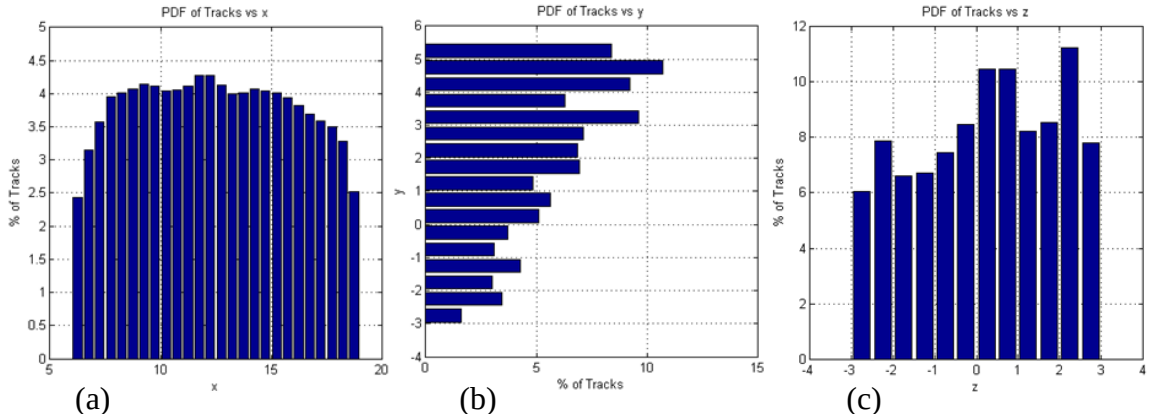

(a) (b) (c)

Figure 3-25: Probability distribution of copepod tracks versus (a) x, (b) y, and (c) z where x, y, and z are non-dimensionalised by d_0 (bar thickness of iteration 0)

Figure 3-26 shows all 259 escape locations for FG305 with U/U_0 plotted in the background. The red dots are the location of first jumps, green for second jumps, yellow for third jumps, blue for fourth jumps, and purple for fifth jumps. The first and second jumps are evenly distributed throughout the measurement volume, but slightly more second jumps occur at larger x. This is a result of the copepods drifting after the first jump. The third, fourth, and fifth jumps almost entirely occur in the wake of iteration 0 and in the shear layer caused by this thickest bar. These multiple escapes show that the copepods must be responding to larger levels of MPSR in this region.

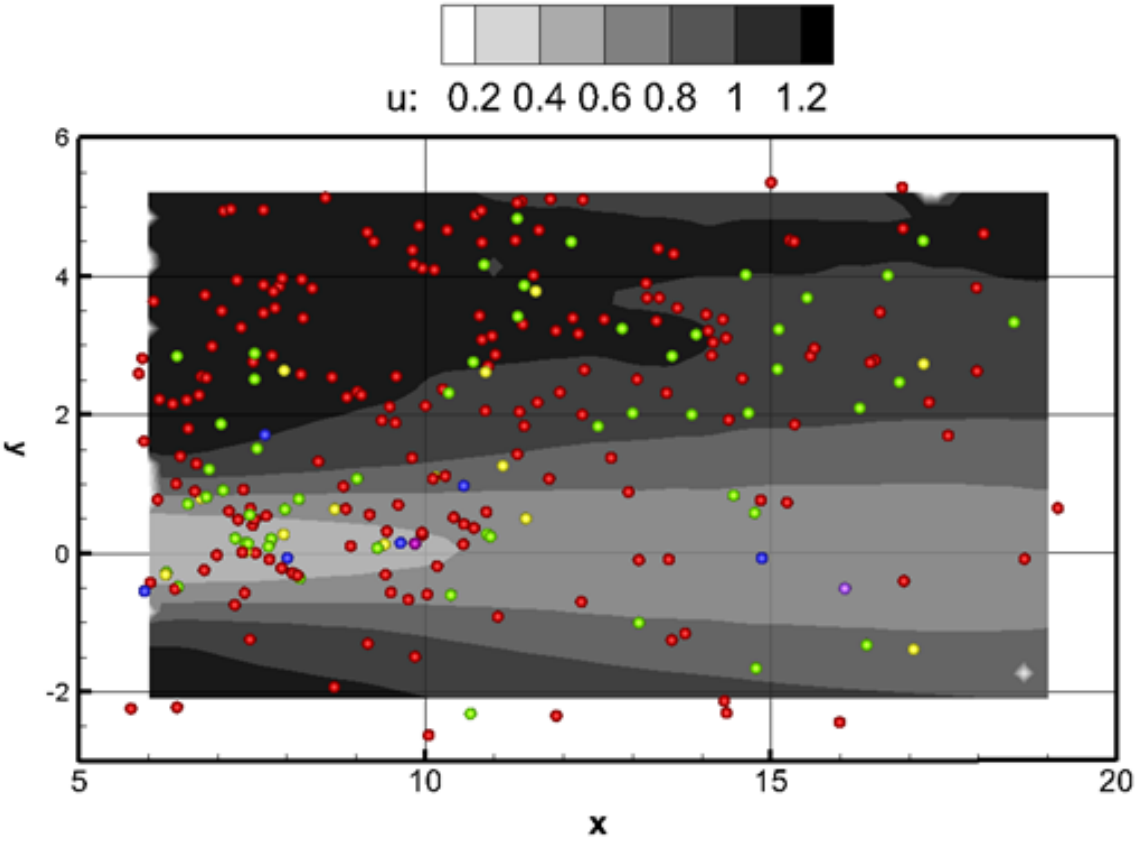

Figure 3-26: Copepod escape locations with U/U_0 in grayscale where x and y are non-dimensionalised by d_0. For each copepod track, the red dot is the location of first escape, green second escape, yellow third escape, blue fourth escape, and purple fifth escape

Figure 3-27 shows the probability distribution of copepod escapes as a percentage of the total escapes versus x, y, and z. Again, the bin width was $0.5d_0$. Figure 3-27 (a) shows the escape percentage versus x. This probability distribution shows many more escapes occurring at smaller x. This agrees with Figure 3-26 where more dots of any color are seen at smaller x. Further downstream in Figure 3-27 (a), the escape percentage decreases as turbulence is dissipated which is to be expected. Figure 3-27 (b) shows the escape distribution as a percentage of the total escapes on the horizontal axis and y on the vertical axis. Here the largest amount of escapes are seen at $-1 < y < 1$ and $2 < y < 4$. $-1 < y < 1$ is in the wake of iteration 0 and is the region with the largest turbulence intensity. In this region, the large escape percentage can be attributed to an increase in multiple jumps as seen in Figure 3-26. In the $2 < y < 4$ region, the large escape

percentage can be attributed to the large amount of first and second jumps as seen from Figure 3-26. In Figure 3-27 (c), the escape distribution with respect to z is shown. Here larger escape percentages are seen for positive z. However, the largest escape percentages occur in the $-1 < z < 1$ region which makes sense as this region had larger values of TI.

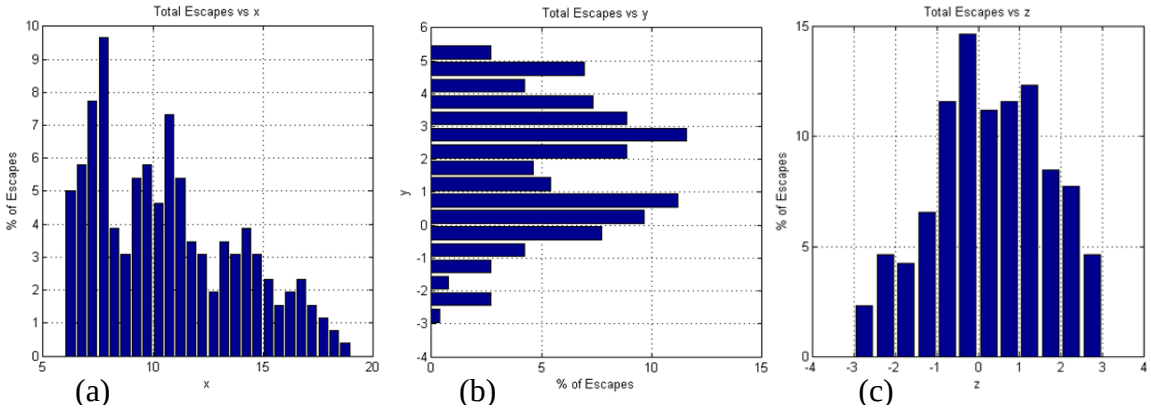

(a) (b) (c)

Figure 3-27: Probability distribution of copepod escapes versus (a) x, (b) y, and (c) z

To better understand spatially the relationship between copepod jumps and copepod populations, we can normalize copepod escape probability by the drift location of the copepods. The results of this normalization are shown in Figure 3-28 where again the bin widths are $0.5d_0$. Drift location was determined from the streamwise mid-point for a copepod track. Therefore, the percentage results in Figure 3-28 will not add to 100% for the given data set, but instead, show how many copepod jumps occurred for the number of copepods in the region. In Figure 3-28 (a), the largest escape probabilities were found in the wake of iteration 0. Here, the copepod escapes per track were found to exceed 40%. This shows that not only were there more copepods jumping in this region but also the copepods that did jump had multiple jumps. This is confirmed with the results in Figure 3-26. However, as compared to Figure 3-27 (b), in the $2 < y < 4$ region where the overall escape percentage was as large as in the wake region, the escapes per track is lower in this region than the wake region for Figure 3-28 (a). In the $2 < y < 4$ region, it was found that the copepod escape probability was at least 20%. Generally, the results in Figure 3-28 (b) are similar to the escape percentage results seen in Figure 3-27 (c) which follows as the track distribution was relatively uniform in z. In Figure 3-28 (b),

there appear to be fewer escapes per track near the edges of the measurement volume as seen in Figure 3-27 (c). There are fewer escapes per track in the $0 < z < 1$ region than in the $-1 < z < 0$ which is a result of more tracks in this region as seen from Figure 3-25 (c).

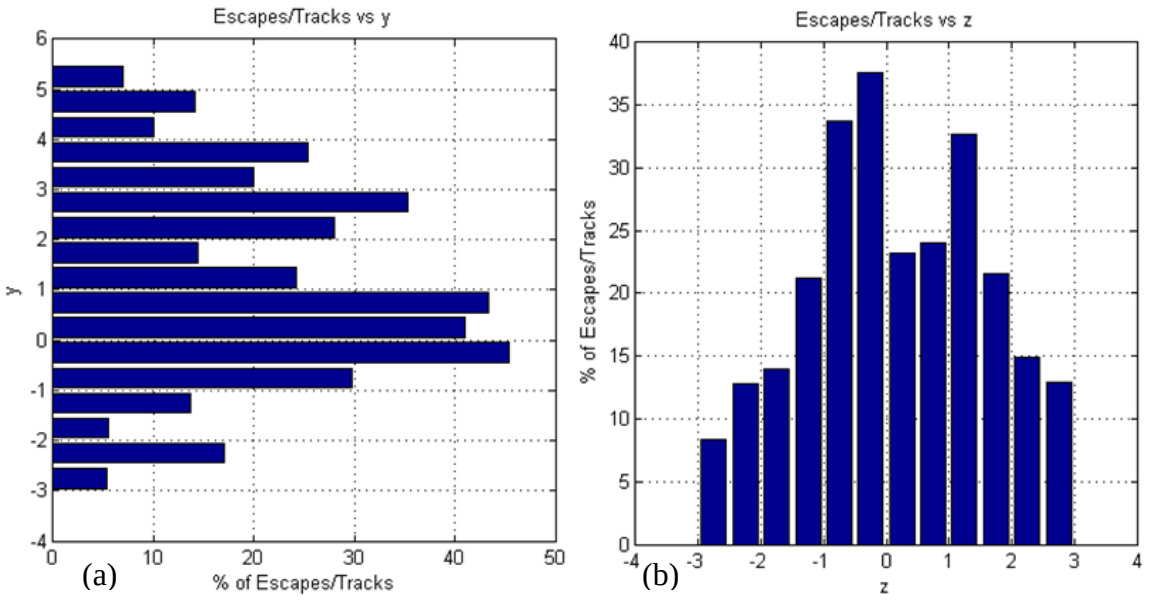

Figure 3-28: Probability distribution of copepod escapes per track versus (a) y and (b) z

As was discussed in the flow field results of Section 3.2, there is symmetry in the flow over the y and z axis. To make trends in jump direction and magnitude more clear, it is advantageous to mirror the escape and track results over the y and z axis. The track and escape probability distributions mirrored over the axis they are plotted against are seen in Figure 3-29 where the bin width is $0.75d_0$. In Figure 3-29 (a), the probability distribution of copepods versus y is shown to be relatively uniform when mirrored over y=0. The lower population percentage at the largest y is a result of fewer copepods being triangulated at the top of the measurement volume. In Figure 3-29 (b), the copepod probability distribution is very uniform when mirrored over z=0. In Figure 3-29 (c) where data is mirrored over y=0, the maximum escapes per track (~45%) occurs at $y <$ 0.75. This is expected as this is the wake region of iteration 0. In Figure 3-29 (d) where data is mirrored over z=0, the escapes per track is much greater (up to 30%) near the center plane. At $z >$ 1.5, the escapes per track are about half (~15%). These results

present the copepod populations and escapes for mirrored data, which improves statistics when examining escape direction trends.

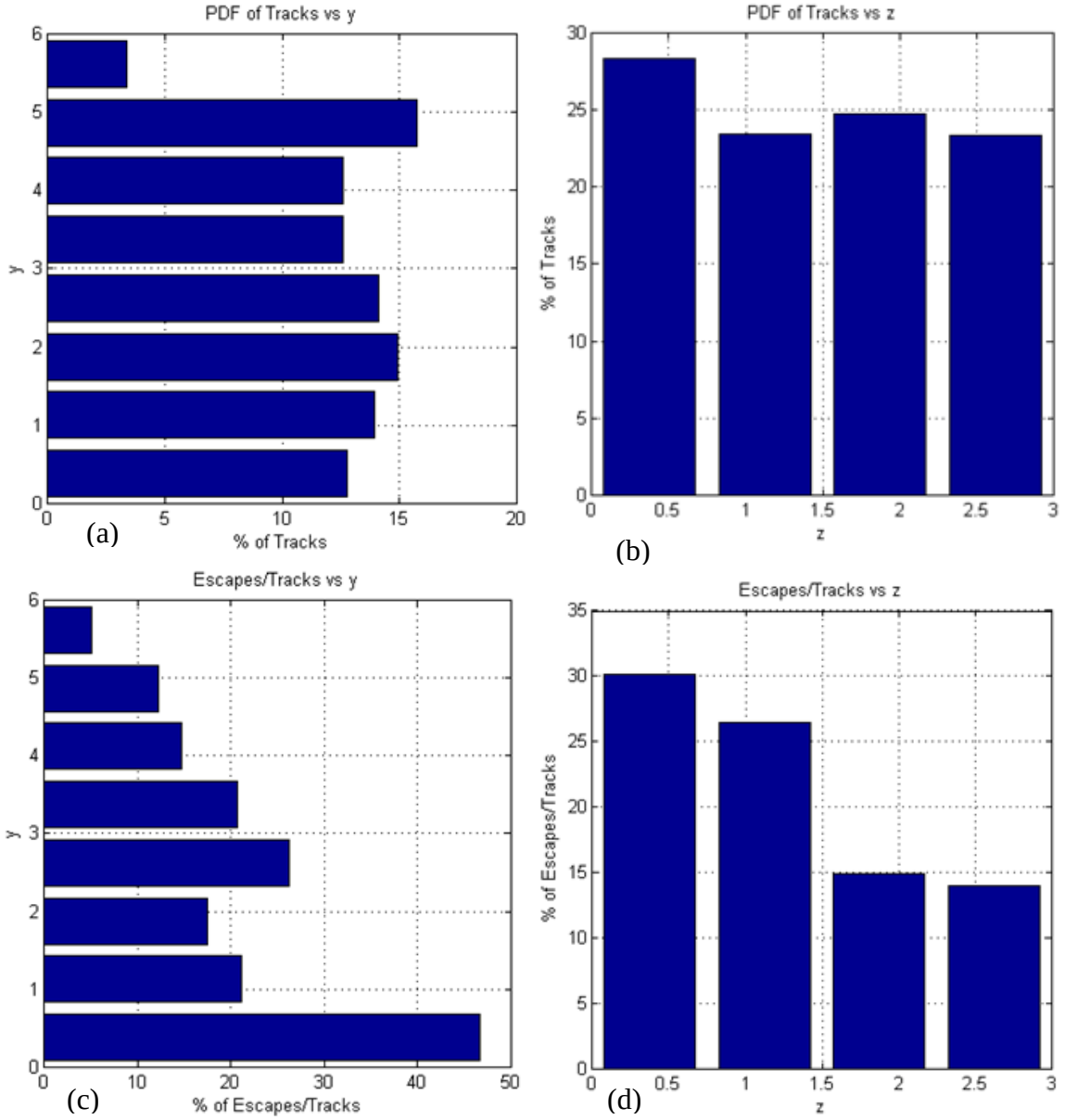

Figure 3-29: The probability distribution is mirrored over the respective axis for copepod tracks versus (a) y and (b) z and copepod escapes per track versus (c) y and (d) z where x, y, and z are non-dimensionalised by d_0

3.5.2. Escape direction

To analyze how copepods respond in a given flow, the averaged direction of copepod escape was examined. Figure 3-30 shows the average of u_{diff} versus y and z where data is mirrored over the respective axis. u_{diff} is defined as

$$u_{diff} = \frac{u_c - U}{U_0}, \tag{3-5}$$

where u_c is the streamwise copepod velocity component and U is the mean streamwise velocity component from TPIV at the copepod escape location. Figure 3-30 has the same bin width as Figure 3-29 which is $0.75d_0$. For each bin, the average u_{diff} is calculated for a given region. When u_{diff} is negative it implies that on average in that region the copepod is jumping back into the freestream. Error bars are calculated from uncertainty of each measurement (Section 2.5) and the statistical variation of u_{diff} for that region based on a student t distribution with a 95% confidence interval. The statistical variation was the largest source of the error bars as some regions had smaller populations and larger variation. Figure 3-30 (a) shows u_{diff} plotted versus y for data being mirrored over y=0. These results show that at all locations on average the copepod is jumping backward into the freestream. The further the distance in y from iteration 0 the stronger the copepod jumped in the negative x direction. From Figure 3-9, we see that U is a minimum in the wake of iteration 0 and increases with increasing y. This implies from the results in Figure 3-30 (a) that the u_c is greater in the negative streamwise direction for larger U. From Figure 3-9, it is observed that U does not vary much over $y > 2$ and Figure 3-30 (a) has fairly consistent u_{diff} for $y > 2$. This shows that u_c exhibited by the copepod scales with the flow. In other words, the escape response is stronger in faster moving flow. Figure 3-30 (b) also shows the copepod jumping toward the freestream for all z regions. This means on average for all regions in the measurement volume the copepod is jumping back into the freestream flow.

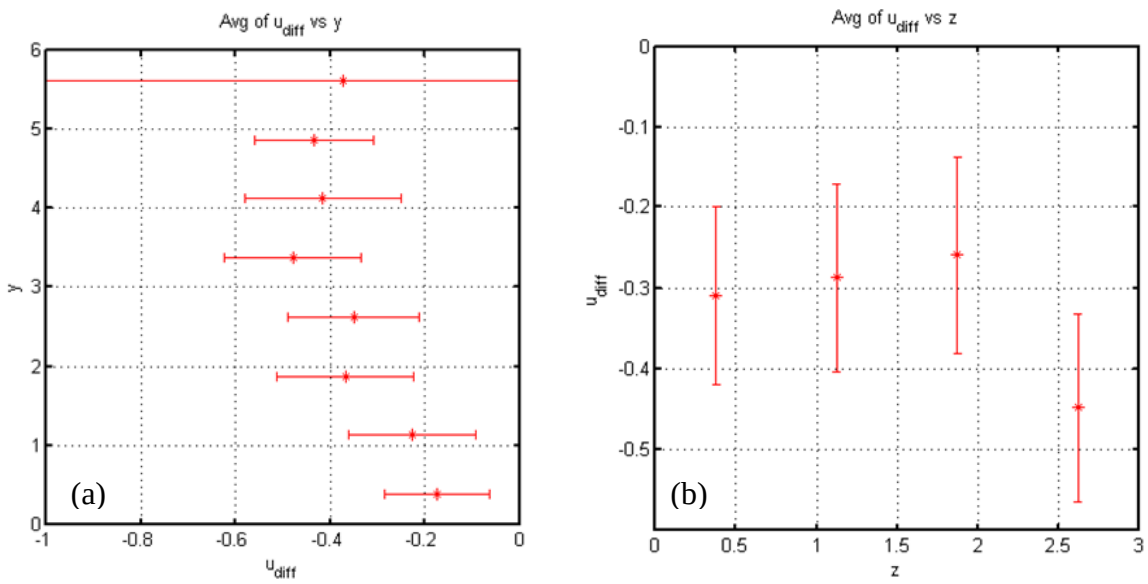

Figure 3-30: Average of u_{diff} with data mirrored over respective axis versus (a) y and (b) z

To examine the wall-normal directional component during copepod jump, a new angle must be defined. This is defined as

$$\phi = \tan^{-1}\frac{dy}{dx} = \tan^{-1}\left(\frac{y_{n+p} - y_n}{x_{n+p} - x_n}\right) \tag{3-6}$$

where dx and dy are the change in position in the x and y directions, respectively. As previously, n denotes the time step at escape, and p is the forward time step integer which was 6. The average ϕ at escape versus $|y|$ is shown in Figure 3-31 (a). From symmetry, the data at y less than zero is given the opposite sign of ϕ when mirrored. This means positive ϕ is away from the y axis and iteration 0. Figure 3-31 (a) shows that in most regions ϕ is greater than zero. However, ϕ is negative in the shear layer ($0.75 < y < 1.5$). This means in most regions copepods jumped away from the thickest beam but in the region of high shear copepods tended to jump towards the wake. The error bars in Figure 3-31 are found in the same way as Figure 3-30. Results in Figure 3-31 (b) are mirrored over z=0 and the sign is reversed for data less than y=0. Therefore, positive ϕ is a jump away from the y axis or iteration 0. Figure 3-31 (b) shows on average copepods closer to the center plane (z=0) tended to jump away from the thickest beam and appeared to not have a wall-normal directional preference further from the center plane (small ϕ). This shows that the positive trend observed in Figure 3-31 (a) is from

copepods near the center plane. From Figure 3-29 (d), it is noted that more copepod escapes occur closer to the center plane which explains the positive trend in ϕ if Figure 3-31 (a). Overall, copepods on average jumped away from iteration 0 except for in the shear layer.

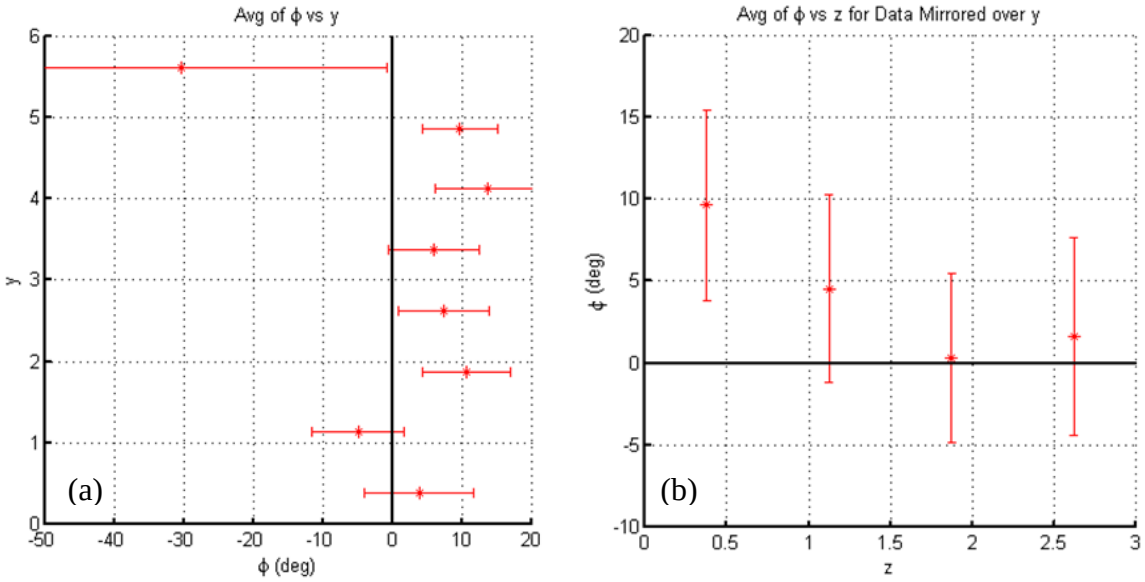

Figure 3-31: Average of ϕ with data mirrored over respective axis versus (a) y and (b) z with data mirrored over y

Similarly to ϕ, an angle showing the change in the spanwise direction, dz, can be calculated. This is defined as

$$\psi = \tan^{-1}\frac{dz}{dx} = \tan^{-1}\left(\frac{z_{n+p} - z_n}{x_{n+p} - x_n}\right) \tag{3-7}$$

where again n is the current time step, and p is the forward time step integer which was 6. For data less than z=0, the opposite sign of ψ is taken. Therefore, positive ψ implies a copepod jump away from the z axis. From Figure 3-11, it was observed that W converges towards the z axis in the region of $-2 < y < 2$ and W diverges from the center plane at y greater than 2. Figure 3-32 (a) shows ψ for data mirrored over y=0. In most regions, ψ is negative which means copepods are jumping towards the center plane. ψ is positive at $2.25 < y < 3$, which is the location where the flow changes from converging towards z=0 to diverging from z=0. In Figure 3-32 (a) for $y < 2.25$, copepods are jumping in the same direction of W (towards z=0) but are jumping in the opposite direction of W for $y > 3$. In Figure 3-32 (b), ψ is plotted against z for $-2 < y < 2$ where

again negative ψ is a jump towards the center plane. Near z=0, copepods appeared to have low directional preference in the spanwise direction (ψ small). Further away, copepods on average jumped towards z=0 which agrees with the results seen in Figure 3-32 (a) for $y < 2.25$.

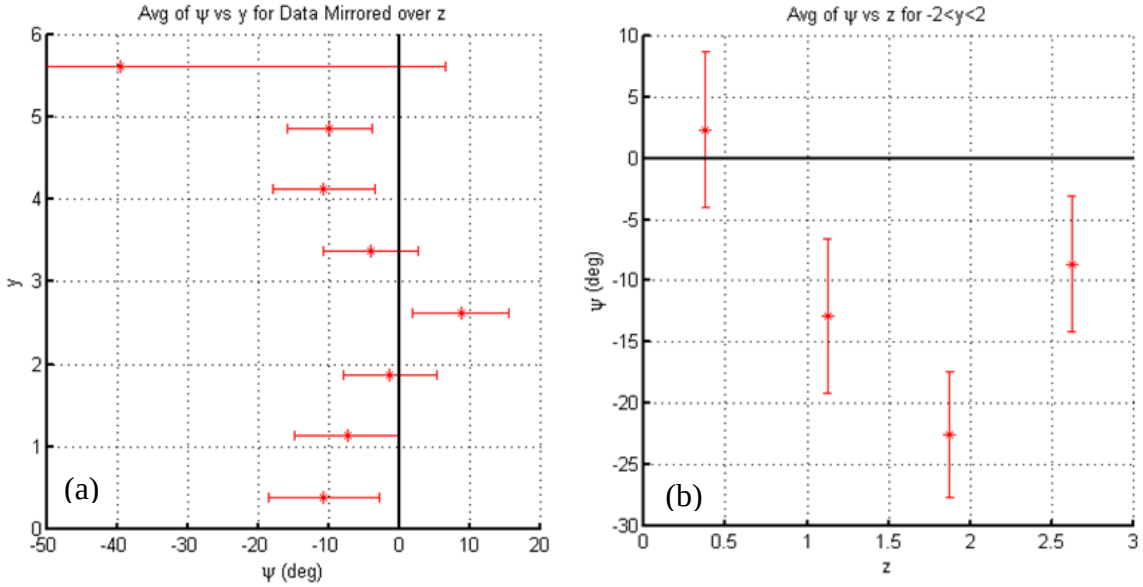

Figure 3-32: Average of ψ with data mirrored over respective axis versus (a) y with data mirrored over z and (b) z for -2 $< y <$ 2

Overall, copepods were found to have directional preferences in their jumps. Copepods were found to jump in the negative streamwise direction which gave increased wall-normal and spanwise position change angles because dx decreased. Generally, copepods were found to jump away from the wake of iteration 0. Copepods were also found to jump towards the center plane even in regions where the flow was going away from z=0.

3.5.3. Escape magnitude

The escape criteria that determined copepod escape were defined in Section 3.3, but further investigation into jump magnitude could provide more insight into copepod response behavior. Jump magnitude can be determined from analysis of θ in Equation (3-4). First, the probability distribution of θ is examined in Figure 3-33 (a) where the red crosses are the probability distribution of all copepod tracks and the blue stars are the probability distribution of tracks where copepod escape was found. Figure 3-33 (a) shows larger populations for $\theta > 15°$ of copepods exhibiting escape behavior as expected. This shows that θ was a good check of escape. Recall, the threshold was $\theta_{max} > 14.5°$ within 0.02s of the escape incident. For all escapes of FG305, the probability distribution of θ_{max} is found in Figure 3-33 (b). In this plot, the red dashed line shows the jump threshold and the black dashed line at 45° shows the separation of what is considered a small jump and large jump. This small and large criterion was based off of the separation seen in the probability distribution of Figure 3-33 (b). 63.7% of the jumps are small and 36.3% of the jumps are large.

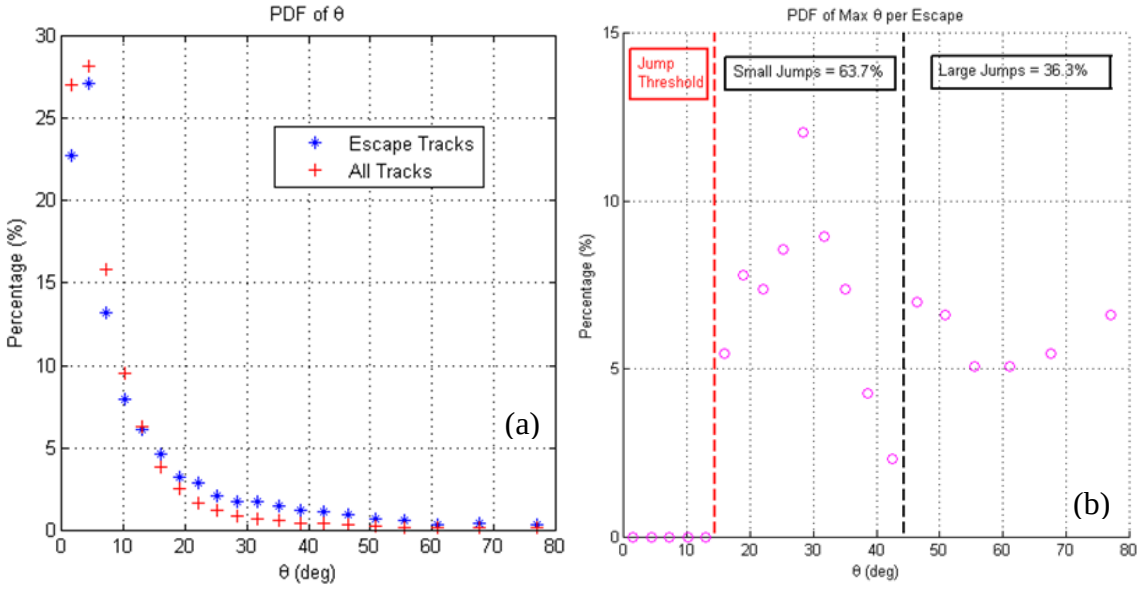

Figure 3-33: Probability distribution for (a) escape tracks (blue) and all tracks (red) and (b) θ_{max} for each escape with jump magnitude criteria

As discussed in Section 3.4.4, the Reynolds number from the copepod slip velocity can be calculated by $Re = \left\|\overrightarrow{v_{c,slip}}\right\| L_c/\nu$ and for all escapes of FG305 the mean was ~140. This slip velocity and Reynolds number can be examined to confirm the jump magnitude criterion of $\theta_{max} = 45°$. For small jumps, the mean slip velocity is 0.13m/s, and the corresponding mean Reynolds number is ~130. Again, a copepod length of 1mm was assumed. For large jumps, the mean slip velocity is 0.16m/s, and the corresponding mean Reynolds number is ~160. Although the difference is small, the large jumps have a larger slip velocity and Reynolds number which shows that θ_{max} criterion is effective at distinguishing jump magnitude.

Similar to Figure 3-29 (c) and (d), the probability distribution of the escapes per track can be plotted to compare the spatial distribution of the small and large jumps. These results are shown in Figure 3-34. The bin width is again $0.75d_0$, so adding the escapes per track percentages of the small and large jumps will give the total results seen in Figure 3-29 (c) and (d) for y and z, respectively. As previously mentioned, there are more small jumps than large jumps so it is expected to see larger probability distributions for small jumps rather than large jumps. In Figure 3-34 (a), where data is mirrored over y=0, generally there are larger populations of small jumps. Except at $y < 0.75$, where there is a slightly larger population of larger jumps. This shows that in the wake of iteration 0, copepods are more likely to make a large jump. This makes sense as flow is more turbulent in this region and will be analyzed in more depth in Section 3.6 when MPSR during escape is analyzed. Figure 3-34 (b) shows the probability distribution of escapes per track versus z for data mirrored over z=0. Here larger distributions of small jumps are seen, but at $z < 0.75$ the amount of small and large jumps is closer. This shows copepods larger jumps occur more frequently near the center plane.

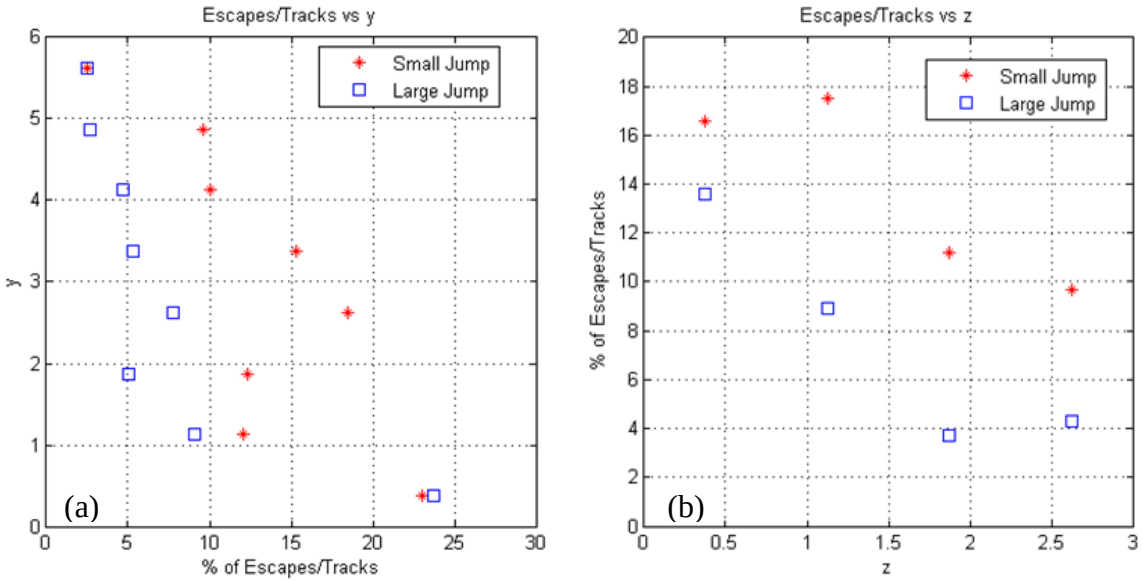

Figure 3-34: Probability distribution for escapes per track for small (red) and large (blue) escapes versus (a) y and (b) z where y and z are non-dimensionalised by d_0

The average of θ_{max} versus x is shown in Figure 3-35 (a). As expected, averages of θ_{max} for large jumps will be greater than small jumps. There are some larger values observed in both the large and small jumps but do not appear to follow a trend. Therefore, these larger values can be attributed to fewer escapes for the respective jumps occurring in that region which leads to less data being averaged. In Figure 3-35 (b), the average θ_{max} for small and large jumps versus y with data mirrored over y=0. The data for both small and large jumps is found to be uniform, but the small jump has a maximum in the wake of iteration 0. In Figure 3-35 (c), the average of θ_{max} for small and large jumps versus z with data mirrored over z=0. The results for the small and large jumps are uniform. In Figure 3-35, almost all averages of θ_{max} for the small jumps lie between 25° to 30° and has a maximum in the wake of iteration 0. Figure 3-35 (b) and (c) show the average θ_{max} for the large jumps is around 60° and does not have a clear geometrical trend.

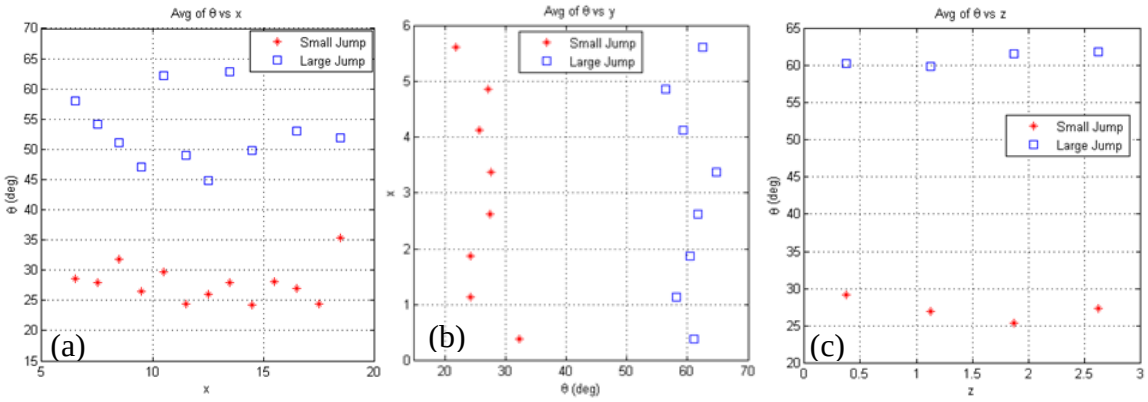

Figure 3-35: Average of θ_{max} for small (red) and large (blue) escapes with data mirrored over respective axis versus (a) x, (b) y, and (c) z

Figure 3-36 (a) and (b) show the average u_{diff} versus y and z, respectively. In Figure 3-36 (a) where data is mirrored over y=0, the large jump averages show copepods jumping with a higher velocity in the negative streamwise direction than for small jumps. The averages of small and large jumps appear to be closest in the wake of iteration 0. This could be an artifact of lower U in this region or the copepod responding to the slower streamwise flow. In Figure 3-36 (b), the average of u_{diff} versus z with data mirrored over z=0 for small and large jumps is found. Again the smaller jumps have larger u_{diff}. The results of Figure 3-36 confirm that when copepods have a larger jump as defined by θ_{max} they will have greater jump magnitudes in the negative streamwise direction (smaller u_{diff}).

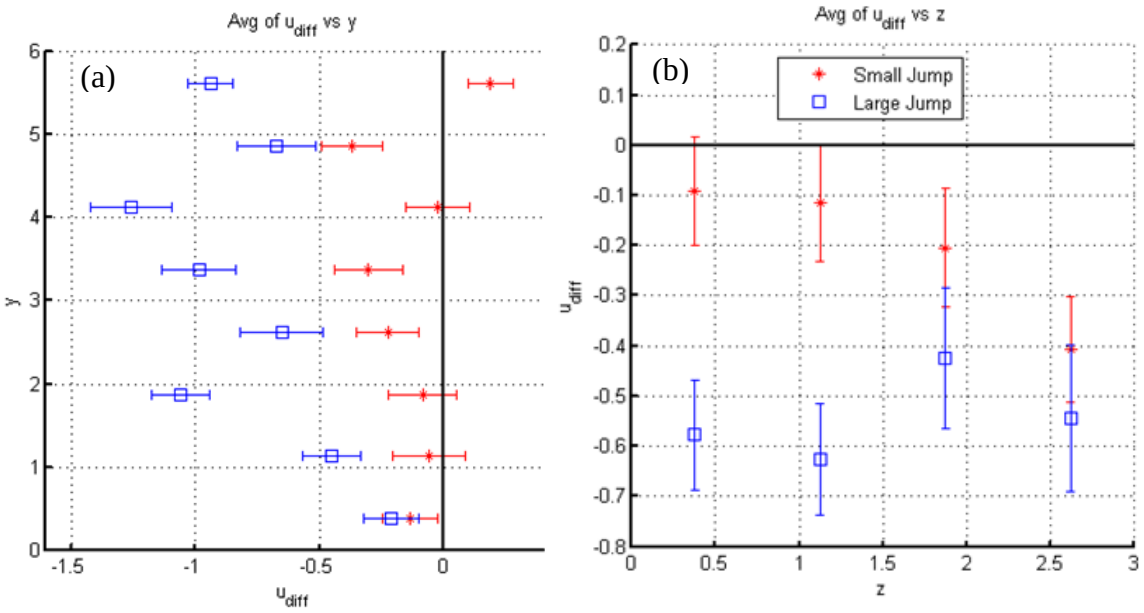

Figure 3-36: Average of u_{diff} for small (red) and large (blue) escapes with data mirrored over respective axis versus (a) y and (b) z

3.6. MPSR during escape for FG305

One of the main focuses of this study was to quantify hydrodynamic signals that elicited escape in copepods. It has been found that copepods respond to MPSR. Therefore, this section analyzes copepod response to MPSR. As for Section 3.5, all analysis in Section 3.6 will be for FG305. In this section, analysis includes 3D MPSR as compared to escape statistics, instantaneous 2D MPSR seen by the copepod, and statistics of 2D and 3D MPSR during escape.

3.6.1. 3D MPSR compared to escape statistics

Figure 3-37 (a) shows the probability distribution of 3D MPSR for three different sub volumes. All three sub volumes include $5 < x < 10$ and $-3 < z < 3$. As shown in Figure 3-37 (b), sub volume 1 is for $3 < y < 5$, sub volume 2 is for $1 < y < 3$, and sub volume 3 is for $-1 < y < 1$. The probability distributions are determined from 1000 independent samples from TPIV for FG305. The probability distribution shows the lowest MPSR values in sub volume 1 and the largest MPSR values occurring in sub volume 3. For sub volumes 1, 2, and 3, the escapes per track percentages were found to be 7%, 16.5%, and 55.2%, respectively. This shows that copepods exhibit higher jump frequency in regions of higher MPSR. Additionally, comparison of the three different sub volumes in Figure 3-37 (a) and (b) show a strong correlation between higher MPSR values occurring in regions with higher turbulence intensities.

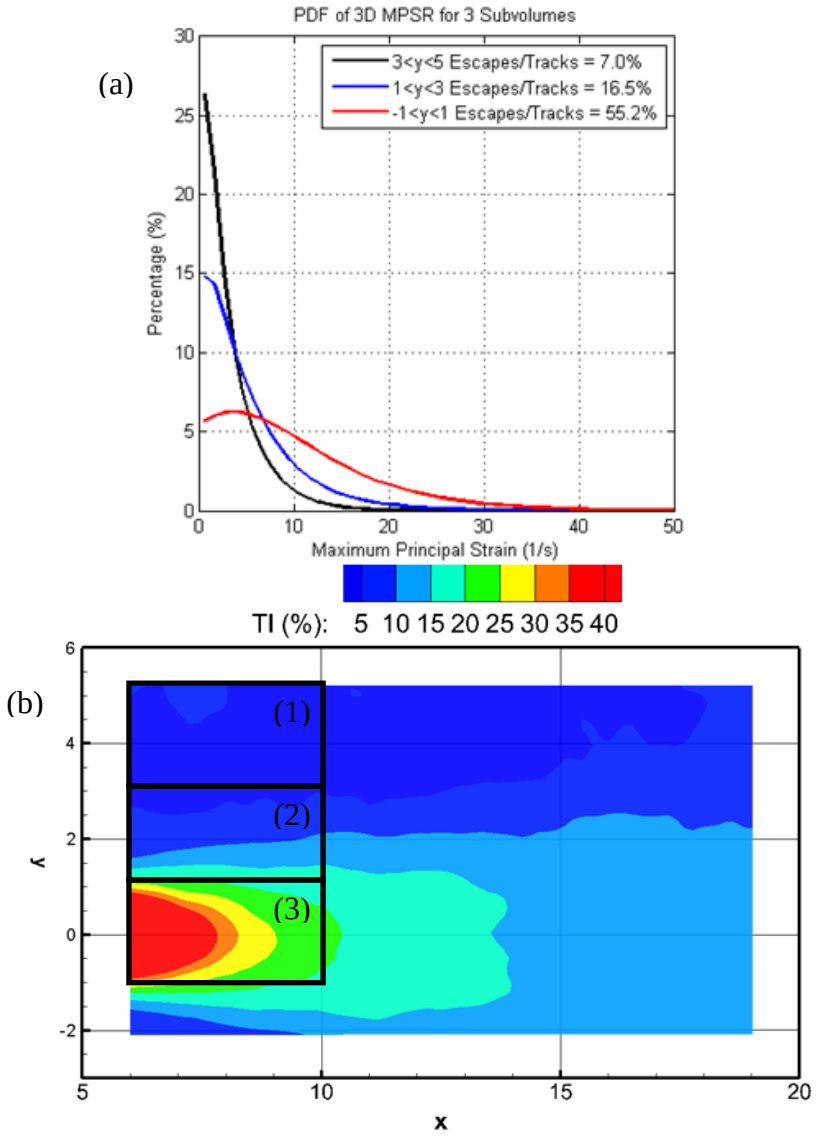

Figure 3-37: The 3D MPSR probability distribution is shown for three different sub volumes in (a). (b) shows the three different sub volumes in (a) with the TI at z=0 where x and y are non-dimensionalised by d_0

3.6.2. Instantaneous 2D MPSR

Only instantaneous 2D MPSR during a copepod track is available as only SPIV was performed during experiments with copepods. Figure 3-38 shows 2D MPSR at z=0 calculated at the (x, y) locations corresponding with three copepod tracks. All of the data for Figure 3-38 is for copepod tracks within -0.5 $< z/d_0 <$ 0.5. The MPSR values are calculated using a bilinear interpolation to the copepod location which is discussed in Appendix B. The dots in Figure 3-38 show when the copepod initiated escape. These three tracks show a large range in MPSR values seen by the copepod. The statistics of 2D and 3D MPSR during escape will be discussed in the next section. Also, as seen from all three tracks, the MPSR appears to be increased before the copepod initiated escape. This suggests the copepod has a response time which is larger than δt. Therefore, a basic experiment of copepods in a small rectangular volume with a cantilevered piece of plastic placed in the container was performed. While recording with a high speed camera and LED illumination, the cantilevered piece was disturbed. The reaction time for several copepods was averaged and found to be 0.0054s. This corresponds to $2\delta t$ for most of the data collected at FG305, therefore the MPSR value calculated two time steps previous to escape was used as the escape MPSR discussed in Section 3.6.3.

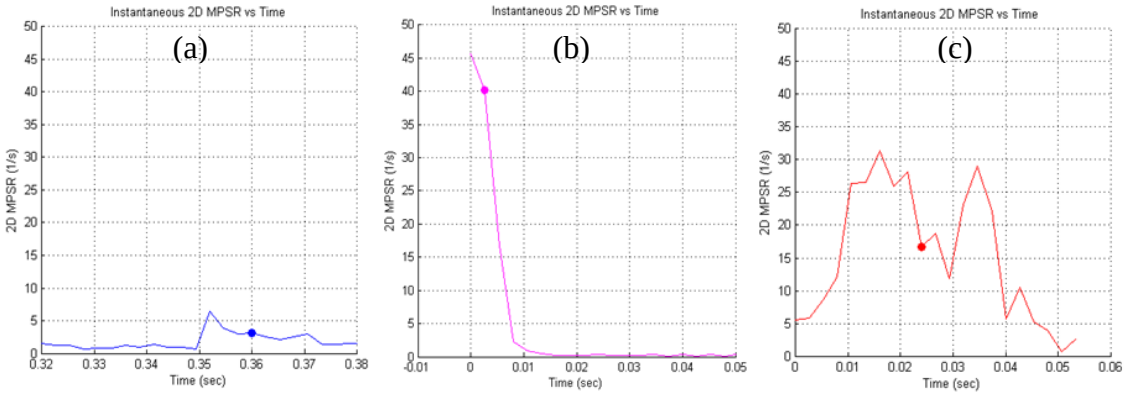

Figure 3-38: (a)-(c) show three different tracks with 2D instantaneous MPSR at center plane calculated with bilinear interpolation

3.6.3. Statistics of 2D and 3D MPSR during escape

The resulting 2D and 3D MPSR that initiate escape behavior will be discussed in this section. Only escapes for -1 $< z/d_0 <$ 1 will be considered as only instantaneous 2D MPSR at z=0 can be calculated, and the MPSR can vary across the spanwise direction as was discussed with instantaneous MPSR fields in Section 3.2.1.4. For FG305, this results in 99 escapes. The probability distribution of the 2D MPSR during escape is seen as black triangles in Figure 3-39 (a) where almost 60% of jumps occurred below $3s^{-1}$. Over 85% of jumps occurred below 2D MPSR values of $10s^{-1}$. Also plotted is the probability distribution of the 2D MPSR from SPIV found for the entire center plane which was the red line seen in Figure 3-20. For all results in this section, the bin width was $1s^{-1}$. For 2D MPSR less than $1s^{-1}$, there is a 15% lower percentage for MPSR during escape. For increasing MPSR, Figure 3-39 (a) generally shows larger populations for MPSR during escape. This is expected as an increase in MPSR has been shown to elicit copepod escape (Adhikari 2013), and this trend would be more definitive with more data. The average 2D MPSR found to initiate escape is $5.6s^{-1}$.

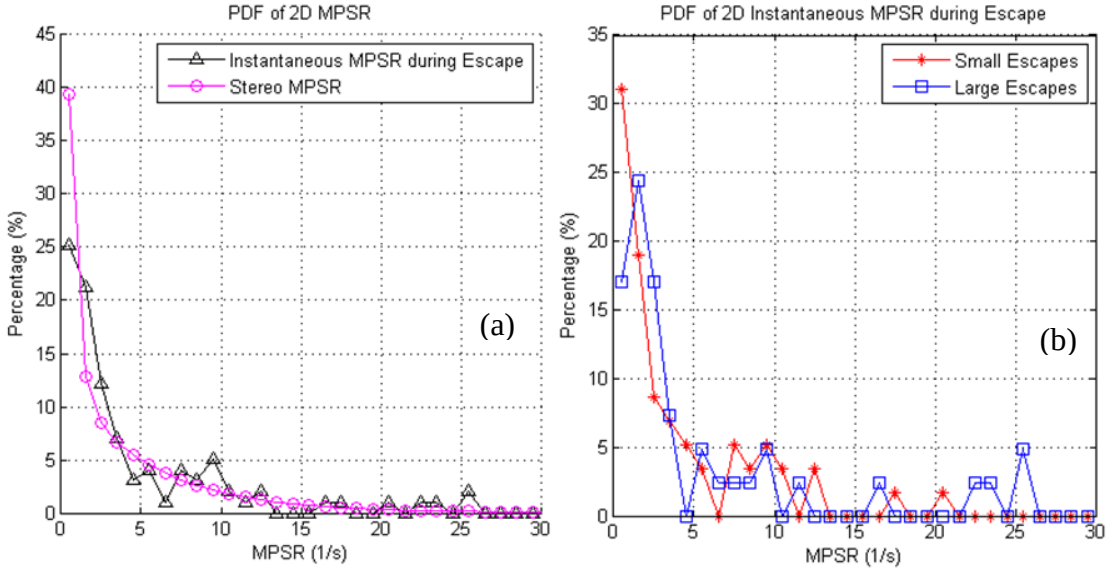

Figure 3-39: The probability distribution of 2D MPSR values sensed by the copepod during escape compared to the entire 2D MPSR at the center plane is shown in (a). (b) shows the probability distribution of 2D MPSR sensed by the copepod for small (red) and large (blue) escapes

For further analysis, the small and large jump criterion from Section 3.5.3 can be applied to the 2D MPSR escape values. The probability distribution of the small and large jumps with all jumps is found in Figure 3-39 (b). Here the percentages of the small and large jumps are normalized by the small and large jumps, respectively. Of the 99 total jumps, 58 were small jumps and 41 were large jumps. For 2D MPSR less than $1s^{-1}$, there are about 15% more small escapes than the relatively few large escapes that occurred here. In this region less than $1s^{-1}$, the small jumps occur nearly as often as in the flow distribution in Figure 3-39 (a). For 2D MPSR between $1s^{-1}$ and $4s^{-1}$, there are greater percentages of large jumps than small and also much greater populations of large jumps as compared against the flow MPSR in Figure 3-39 (a). Only large jumps are observed for 2D MPSR greater than $21s^{-1}$. These results show larger populations of large jumps at larger MPSR values. The average 2D MPSR for the small jumps was $4.7s^{-1}$, while the average for large jumps was $7.0s^{-1}$. This shows that on average a copepod will exhibit a larger jump for a larger sensed MPSR, as also observed from Figure 3-39 (b).

From Equation 3-2, 3D MPSR at the center plane can be approximated from 2D MPSR. In Figure 3-39 (a) for 2D MPSR, almost 60% of the jumps occurred below $3s^{-1}$ which correspond to 3D MPSR values below $5.2s^{-1}$. Kiørboe *et al*. (1999) and Adhikari (2013) both reported MPSR thresholds of $0.5 – 5s^{-1}$ to elicit copepod escape. As almost 60% of the escapes analyzed in this study where below 3D MPSR values of $5.2s^{-1}$, the MPSR thresholds found agree with Kiørboe *et al*. (1999) and Adhikari (2013). In Figure 3-39 (a), over 85% of the jumps occurred below 2D MPSR values of $10s^{-1}$ which correspond to 3D MPSR values below $11.5s^{-1}$. This is in agreement with Buskey *et al.* (2002) which reported MPSR thresholds of $0.4\text{-}12s^{-1}$. Over 85% of these escapes were found at thresholds that agree Buskey *et al.* (2002). The other 15% of escapes are a result of the square fractal grid generating higher values of MPSR than created by Buskey *et al.* (2002). The 3D MPSR mean for all jumps is $7.9s^{-1}$ which is within the reported threshold range of Fields and Yen (1996 & 1997), Buskey *et al.* (2002), and Viitasalo *et al.* (2001). The 3D MPSR means are $6.9s^{-1}$ and $9.3s^{-1}$ for small and large jumps,

respectively. Again, larger jump magnitudes are found for larger MPSR sensed during escape.

Chapter 4: Conclusions and Future Work

The objective of this thesis was to determine copepod response to turbulence generated by obstacles in cross flow. The main focus of this study was the flow downstream a square fractal grid and the corresponding copepod response. In this chapter, the conclusions and future work will be discussed.

4.1. Conclusions

Experiments with copepods used simultaneous time resolved measurements of 3D-PTV for copepod tracking within a measurement volume and SPIV at the center plane of the channel. To accurately determine a copepod escape from a copepods position and velocity, escape criteria were set. Three different escape criteria were set to account for noise and systematic error present in the 3D-PTV measurement system. The first is a 15% velocity magnitude difference between time steps. The second was a 5° difference in trajectory angle using an averaged dot product. The final criterion was a 14.5° difference in position in the non-streamwise direction over several time steps. This allowed for accurate prediction of copepod escape. As a control, experiments with copepods were performed for the two freestream flows of this study (U_0=0.039m/s and U_0=0.115m/s). It was found that copepods did not exhibit escape responses for the faster uniform flow speed but had about an 8% escape percentage at the slower speed which is a result of the copepod reorienting itself. These reorienting escapes had a mean slip velocity of 0.04m/s, where the slip velocity is the copepod velocity minus the mean fluid velocity at that location. The corresponding mean Reynolds number for these reorienting jumps was ~40 which was in close agreement to the cruise swimming behavior found by Catton *et al.* (2006 & 2012).

Experiments were performed downstream of a horizontal cylinder. The copepod escape percentages were 7.5% and 1.5% for U_0=0.039m/s and U_0=0.115m/s, respectively. Also, low copepod populations were observed downstream of the cylinder.

This suggests that the escape percentage for U_0=0.039m/s was copepod exhibiting cruise swimming behavior at the slower freestream. Also, results downstream the cylinder for U_0=0.115m/s are very similar to uniform flow at that speed. These results confirm those of Adhikari (2013) which found that low copepod populations downstream of the cylinder was a result of copepods jumping away from the cylinder upstream. Adhikari (2013) also found low copepod response in the wake of the cylinder even when thresholds exceeded those that elicited escape upstream of the cylinder. This was confirmed in the current study as almost no response was observed by copepods in the cylinder wake.

To gain insight to the copepod response downstream of the square fractal grid, TPIV was performed at both freestream speeds to resolve three dimensional velocity components within the measurement volume where copepods were tracked. Results of FG105 and FG305 (see Table 3-1) were normalized by their respective freestream speeds for comparison. FG105 showed that iterations 2 and 3 were more dominant in the relative root mean square velocity fluctuations than for FG305. For FG305, the velocity fluctuations were dominated by iteration 0 which was in a turbulent regime from a Reynolds number comparison to a cylinder in cross flow. FG105 had lower turbulence intensities than FG305 in the wake of iteration 0, where iteration 0 was in a transitional regime for FG105. FG305 had a larger flow deficit in the wake of iteration 0 than FG105. However, FG105 had a longer streamwise wake behind iteration 0 than FG305. Also, FG105 had larger streamwise deficits in the wake of iterations 2 and 3. Overall, the flow for FG305 was dominated more by iteration 0 while iterations 2 and 3 had a larger affect on flow for FG105.

MPSR, which has been shown to elicit escape in copepods (Fields and Yen 1996, Kiørboe *et al*. 1999, Viitasalo *et al.* 2001), was investigated for FG305. MPSR was found to be the highest behind iteration 0. A relationship between 2D and 3D MPSR at the center plane from TPIV was found (see Equation 3-2) where 3D MPSR was always higher. This allowed 3D MPSR to be approximated from 2D MPSR which was the only instantaneous MPSR available from experiments with copepods.

Experiments with copepods were performed downstream the fractal grid at many locations for both freestream speeds. The highest escape percentages where found directly downstream of the fractal grid (FG105 and FG305) where turbulence was the greatest. U_0=0.039m/s had a higher overall escape percentage than U_0=0.115m/s. For U_0=0.039m/s, closest to the grid the escape percentage was about 13%. Further downstream, this decreased to about 8% which matched the escape percentage of the freestream. This shows that further downstream the copepods may have been reorienting themselves (cruise swimming) rather than responding to disturbances created from the fractal grid. For U_0=0.115m/s, the highest escape percentage was closest to the grid which was about 15%. The escape percentage kept decreasing downstream until reaching a minimum of 2%. This shows as turbulence was decaying further downstream copepod response frequency decreased to that of uniform flow.

To avoid analysis of copepod reorientation at low speed, FG305 was used for in depth analysis as FG305 had the highest copepod escape percentage. These jumps were found to have a mean slip velocity of 0.14m/s and corresponding mean Reynolds number of ~140. As compared to Catton *et al.* (2006 & 2012), these jumps are in the escape swimming regime. Copepods exhibiting multiple jumps were concentrated in the wake of iteration 0 where high turbulence was observed for FG305. The escape direction of the copepods was analyzed, and it was found that in all regions of the measurement volume the copepods jumped against the freestream (negative x direction). During escape, copepods on average jumped away from the wake of iteration 0 in the wall normal direction in most regions. In addition, copepods on average were found to jump towards z=0 across the spanwise direction in most regions even where the mean flow was found to be diverging from z=0. Escape magnitude was also investigated. The difference between small and large jumps was a 45° difference in position in the non-streamwise direction. It was found that more large jumps occurred in the wake of iteration 0. In addition, larger jumps were observed to have a greater negative streamwise velocity component than smaller jumps. Large jumps were found to have a larger slip velocity (0.16m/s) than small jumps (0.13m/s). This escape magnitude

criterion gave interesting comparison when investigating MPSR that elicited copepod escape.

First, to gain insight of general escape frequency compared to MPSR probability distributions, three sub volumes for FG305 were analyzed. It was found that the region with the lower MPSR had the lowest escape percentage (7%) while the regions with the higher MPSR had the greatest escape percentage (55%). This proves that on average MPSR elicits copepod escape but instantaneous values of MPSR provide better correlation. Only escapes close to the center plane were considered for instantaneous MPSR as spanwise variation was observed in the instantaneous MPSR downstream of the fractal grid. From a probability distribution of the instantaneous 2D MPSR that created escape, it was found that 60% of the escapes occurred below $3s^{-1}$ and 85% of the escapes occurred below $10s^{-1}$. The mean 2D MPSR that elicited escape was $5.6s^{-1}$. For the small jumps, the mean 2D MPSR was $4.7s^{-1}$, while for the large jumps, the mean was $7s^{-1}$. This shows that on average the larger the MPSR sensed by the copepod the larger the escape. From the 2D to 3D MPSR relation, it was found that 60% of the escapes were below $5.2s^{-1}$ which closely match the threshold range found by Kiørboe *et al*. (1999) and Adhikari (2013). Over 85% of the escapes for 3D MPSR were below $11.5s^{-1}$ which matched the threshold range found from Buskey *et al.* (2002). The other 15% of escapes resulted from the square fractal grid generating higher values of MPSR than created by Buskey *et al.* (2002).

Overall, the fractal grid was shown to elicit copepod escape, specifically directly downstream with escape frequency decreasing further downstream where turbulence levels were much lower. There was almost no copepod response downstream of a cylinder where the mean 2D MPSR was found to be about 50% less than that of the fractal grid for the same freestream. It was also found that at a slower freestream speed copepods exhibited jumps not in reaction to disturbances in the flow but to reorient themselves (cruise swimming). In regions with high MPSR, copepods were observed to exhibit multiple escapes. Moreover, copepods were observed to jump towards regions of lower turbulence and into the freestream direction. Finally, it was found that on average larger sensed MPSR from the copepod created larger escapes.

4.2. Future work

This thesis has provided much insight into copepod response to turbulence, but to gain more information, improvements to the measurement system can be made and different experiments can be performed. To gain three dimensional instantaneous information of the flow surrounding the copepod, TPIV could be performed simultaneously with 3D-PTV. This would give instantaneous 3D MPSR at the exact copepod location which would be more accurate than 2D MPSR at the center plane. For this experiment, the 3D-PTV measurements were noisy especially during copepod escape. To reduce this noise, it would be beneficial to have three cameras or develop some sort of simultaneous combination of 3D-PTV and TPIV to more accurately track copepods. This noise could be reduced by having a larger field of view (measurement volume). This would decrease the size of the copepod to a more spherical shape and therefore help eliminate the noise associated with two cameras seeing different copepod shapes.

To gain other information about copepod response, more experiments for different conditions could be performed. This could include experiments with different grids or flow obstacles placed in the flow. For example, to mimic copepod behavior in drift across a coral reef, an array of cylinders could be placed into the test section. To fully understand the copepods role in the food chain, it would be useful to perform experiments with fish. These could also be combined with placing different obstacles into the flow. Whales and other large aquatic organisms feed on copepods as well. Therefore, it would be interesting to study copepod response in experiments representative of the flow created by large organisms during feeding. This could provide useful information into the predatory success rate for whales and other large organisms.

Bibliography

Adhikari D (2013) Volumetric Velocity Measurement of Aquatic Predator-Prey Interactions. *PhD Thesis*. University of Minnesota, Minneapolis, MN, USA.

Adrian RJ, Westerweel J (2011) Particle Image Velocimetry. *Cambridge University Pres.* New York, USA

Blevins RD (1990) Flow-Induced Vibration Second Edition. *Krieger Publishing Company.* Florida, USA

Buskey EJ, Lenz PH and Hartline DK (2002) Escape behavior of planktonic copepods in response to hydrodynamic disturbances: high speed video analysis" *Mar Ecol Prog Ser.* **235**: 135-146

Catton KB, Webster DR, Brown J, Yen J (2006) Quantitative analysis of tethered and free-swimming copepodid flow fields. *J Exp Biol.* **210**:299-310

Catton KB, Webster DR and Yen J (2012) The effect of fluid viscosity, habitat temperature, and body size on the flow disturbance of *Euchaeta*. *L&O:F&E.* **2**: 80-92

Fields DM and Yen J (1996) The escape behavior of *Pleuromamma xiphias* from a quantifiable fluid mechanical disturbance. *Zooplankton: sensory ecology and physiology*. Ed. Lenz PH, Hartline DK, Purcell JE, Macmillan DL. pp 323-339

Fields DM and Yen J (1997) The escape behavior of marine copepods in response to a quantifiable fluid mechanical disturbance. *J. Plankton Res.* **19**: 1289-1304

Gomes-Fernandes R, Ganapathisubramani B and Vassilicos JC (2012) Particle image Velocimetry study of fractal-generated turbulence. *J Fluid Mech.* **711**: 306-336

Jiang H and Kiørboe T (2011) The fluid dynamics of swimming by jumping in copepods. *J R Soc Interface*. **8**: 1090-1103

Kiørboe T, Saiz E and Visser A (1999) Hydrodynamic signal perception in the copepod *Acartia tonsa Mar Ecol Prog Ser.* **179**: 97-111

Kiørboe T, Jiang H, Colin SP (2010) Danger of zooplankton feeding: The fluid signal generated by ambush feeding copepods. *Proc R Soc B.* **277**: 3229-3237

Kundu P, Cohen I, and Dowling D (2012) Fluid Mechanics Fifth Edition. *Academic Press*. MA, USA.

Laizet S and Vassilicos J (2011) DNS of fractal-generated turbulence. *Flow Turbulence Combustion.* **87**, 673-705

Lenz PH, Hartline DK and Davis AD (2000) The need for speed. I. Fast reactions and muelinated axons in copepods. *J Comp Physiol.* **186**: 337-345

Lenz PH and Yen J (1993) Distal setal mechanoreceptors of the first antennae of marine copepods. *Bull Mar Sci.* **53**: 170-179

Marxen M, Sullivan PE, Loewen MR, Jahne B (2000) Comparison of Gaussian particle center estimators and the achievable measurement density for particle tracking velocimetry. *Exp in Fluids*. **29**: 145-153

Mauchline J (1998) Advances in Marine Biology Vol 33: The Biology of Calanoid Copepods. *Academic Press*. San Diego, California, USA

Murphy DW (2012) Planktonic propulsion: The hydrodynamics, kinematics, and design of metachrony. *PhD Thesis*. Georgia Institute of Technology, Atlanta, Georgia, USA.

Murphy DW, Webster DR and Yen J (2012) A High Speed Tomographic PIV System for Measuring Zooplankton Flow. *L&O: Methods.* **10**: 1096-1112

Schlichting H (1979) Boundary-Layer Theory. *McGraw-Hill Series in Mechanical Engineering*. New York, USA

Viitasalo M, Flinkman J, and Viherluoto M (2001) Zooplanktivory in the Baltic Sea: a comparison of prey selectivity by *Clupea harengus* and *Mysis mixta*, with reference to prey escape reactions. *Marine Ecology Progress Series*. **216**: 191-200

Yen J and Fields D (1992) Escape reponses of Acartia hudsonica nauplii from the flow field of Temora longicornis. *Arch. Hydrobiol. Beih. Ergebn. Limnol.* **36**: 123-134

Yen J (2000) Life in Transition: Balancing Inertial and Viscous Forces by Planktonic Copepods. *Biol Bull.* **198**: 213-224

Appendix A: 3D flow fields for FG105

Figures A-1 through A-7 show FG105 results from TPIV. x=0 is the trailing edge of the grid, y=0 is the center of the thickest beam (iteration 0), and z=0 is the center plane of grid. The results in this section are non-dimensionalised by d_0 for x, y, and z. For results plotted in the y-z plane, the centerlines of iterations 0, 2, and 3 of the fractal grid upstream are shown. The important results and differences between FG105 and FG305 are discussed in Section 3.2.1.3. The figures in this appendix are to give a more complete visual understanding of the flow field for FG105.

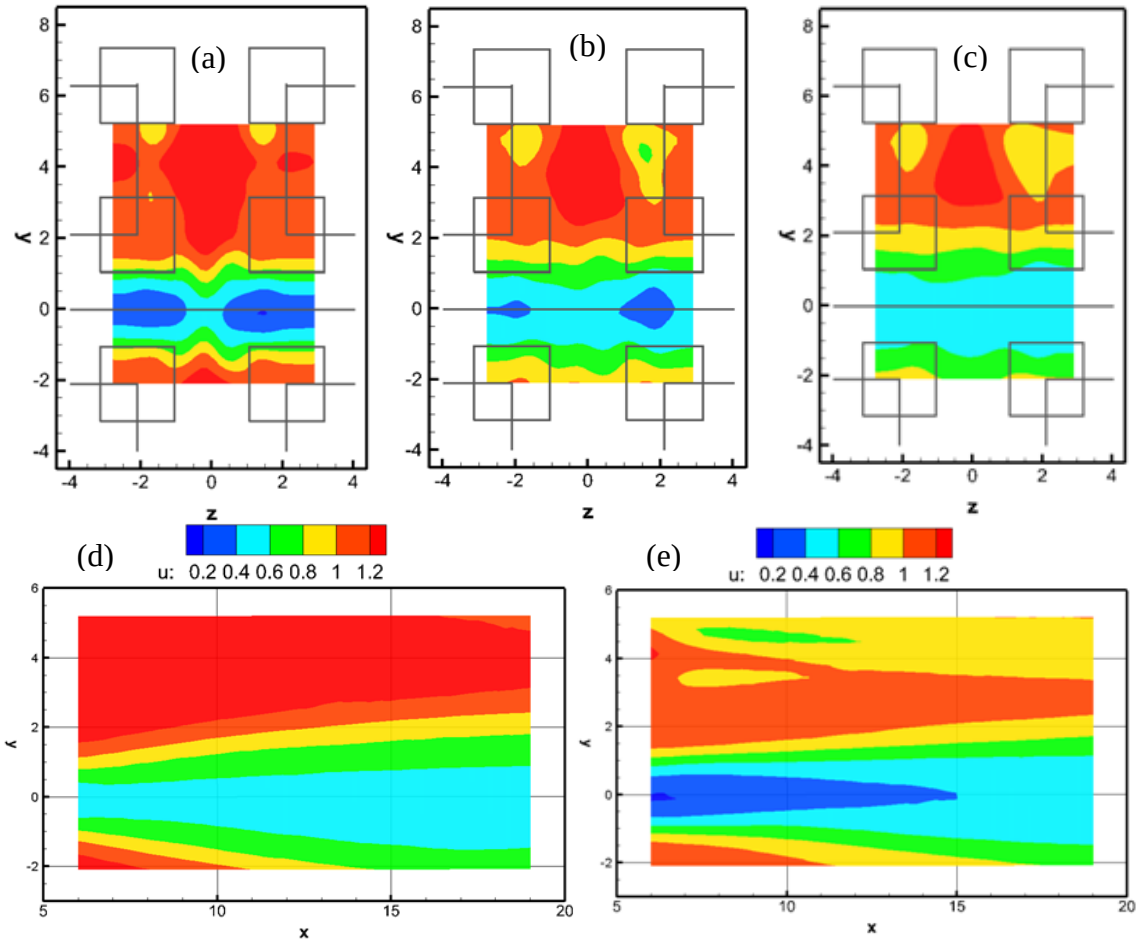

Figure A-1: $\frac{U}{U_0}$ for FG105 at (a) x=6.5, (b) x=11.5, (c) x=16, (d) z=0, and (e) z=1.4 where x, y, and z non-dimensionalised by d_0.

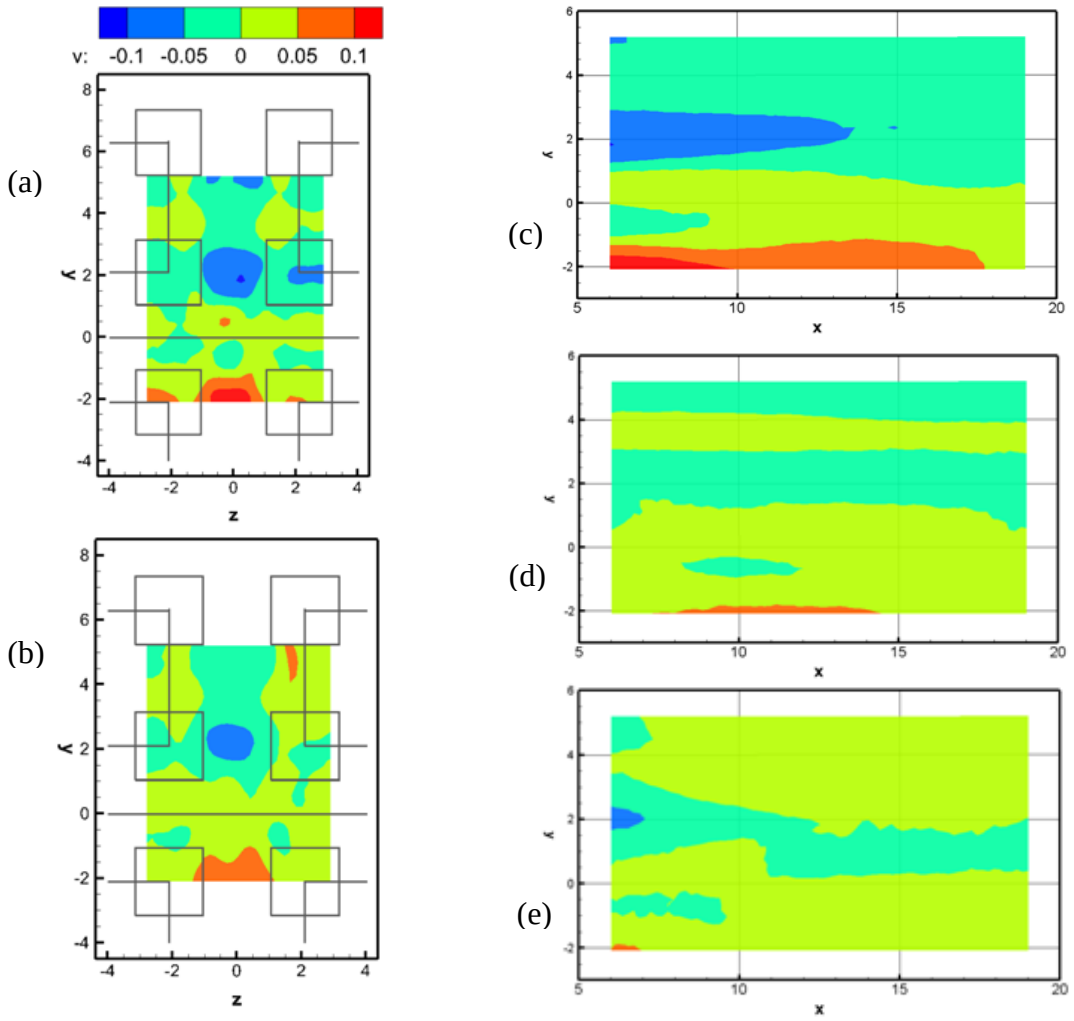

Figure A-2: $\frac{V}{U_0}$ for FG105 at (a) x=6.5, (b) x=11, (c) z=0, (d) z=1, and (e) z=2

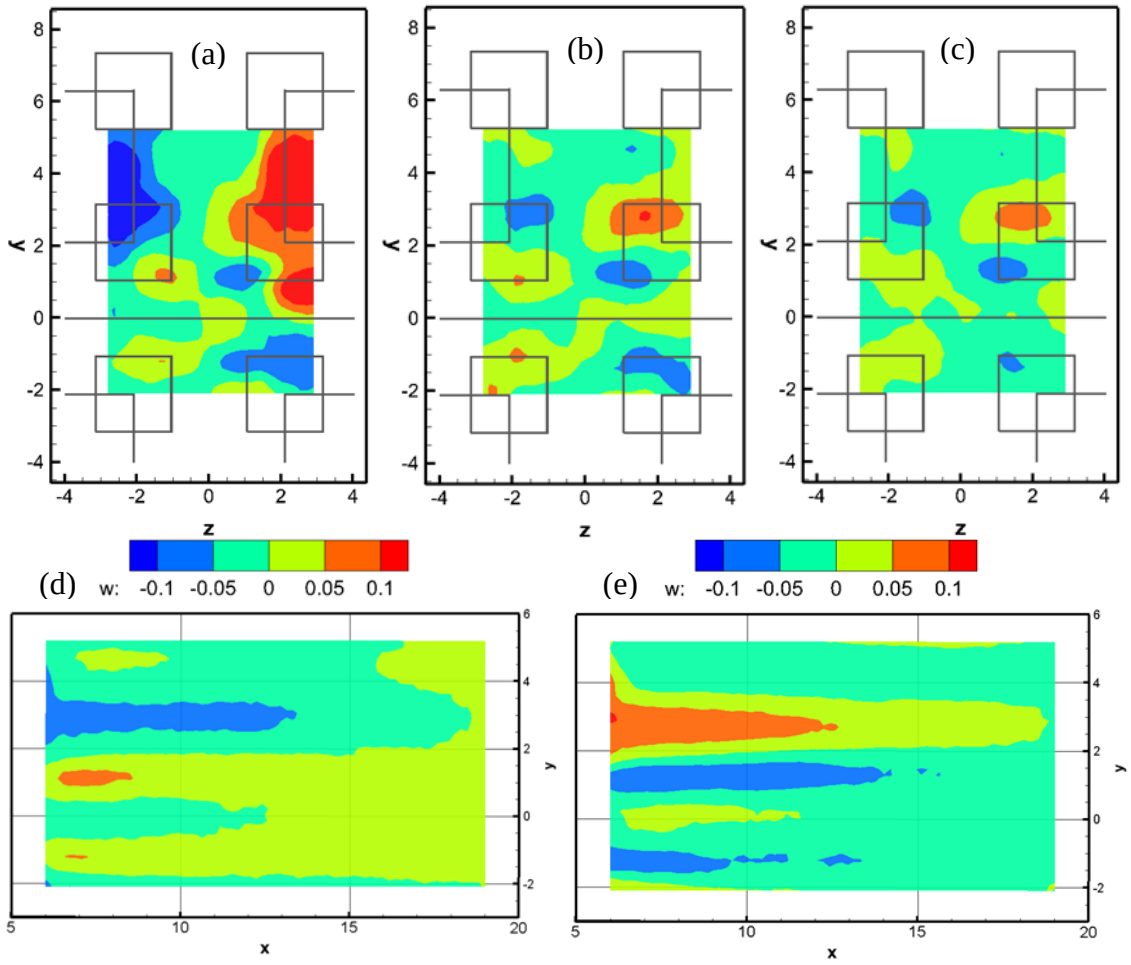

Figure A-3: $\frac{W}{U_0}$ for FG105 at (a) x=6.5, (b) x=9, (c) x=12, (d) z=-1, and (e) z=1

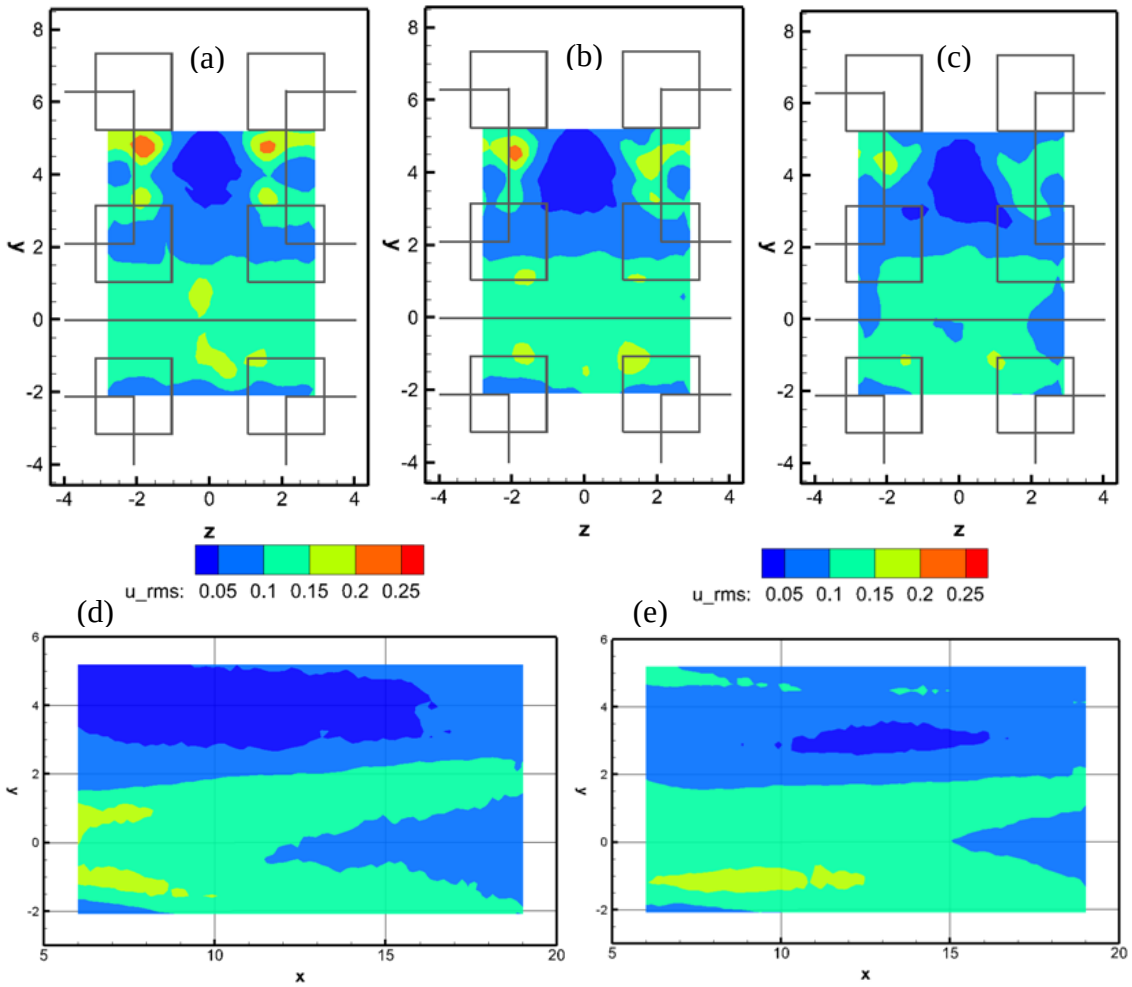

Figure A-4: $\frac{u_{rms}}{U_0}$ for FG105 at (a) x=6.5, (b) x=9, (c) x=12, (d) z=0, and (e) z=1

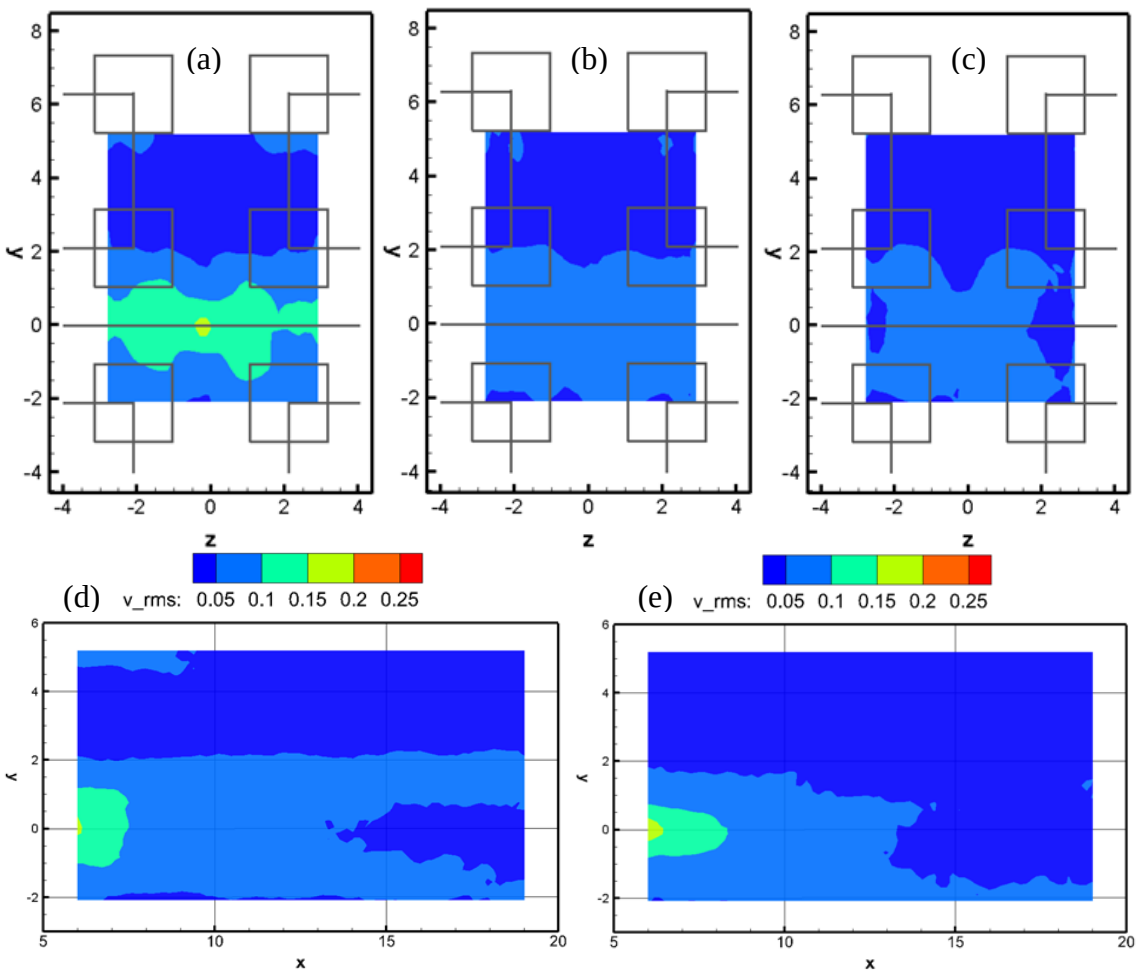

Figure A-5: $\frac{v_{rms}}{U_0}$ for FG105 at (a) x=6.5, (b) x=9, (c) x=12, (d) z=-1.8, and (e) z=0

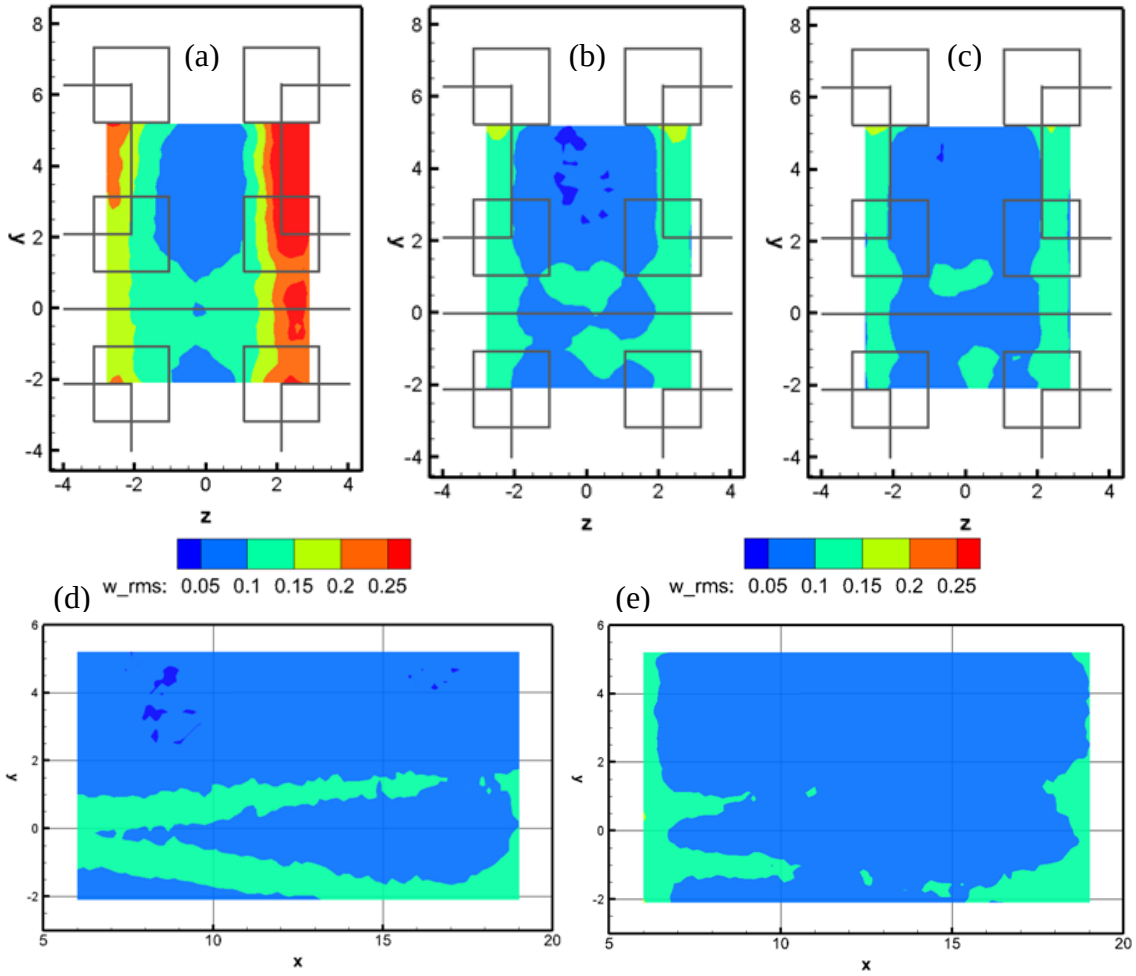

Figure A-6: $\frac{w_{rms}}{U_0}$ for FG105 at (a) x=6.5, (b) x=9, (c) x=12, (d) z=0, and (e) z=1

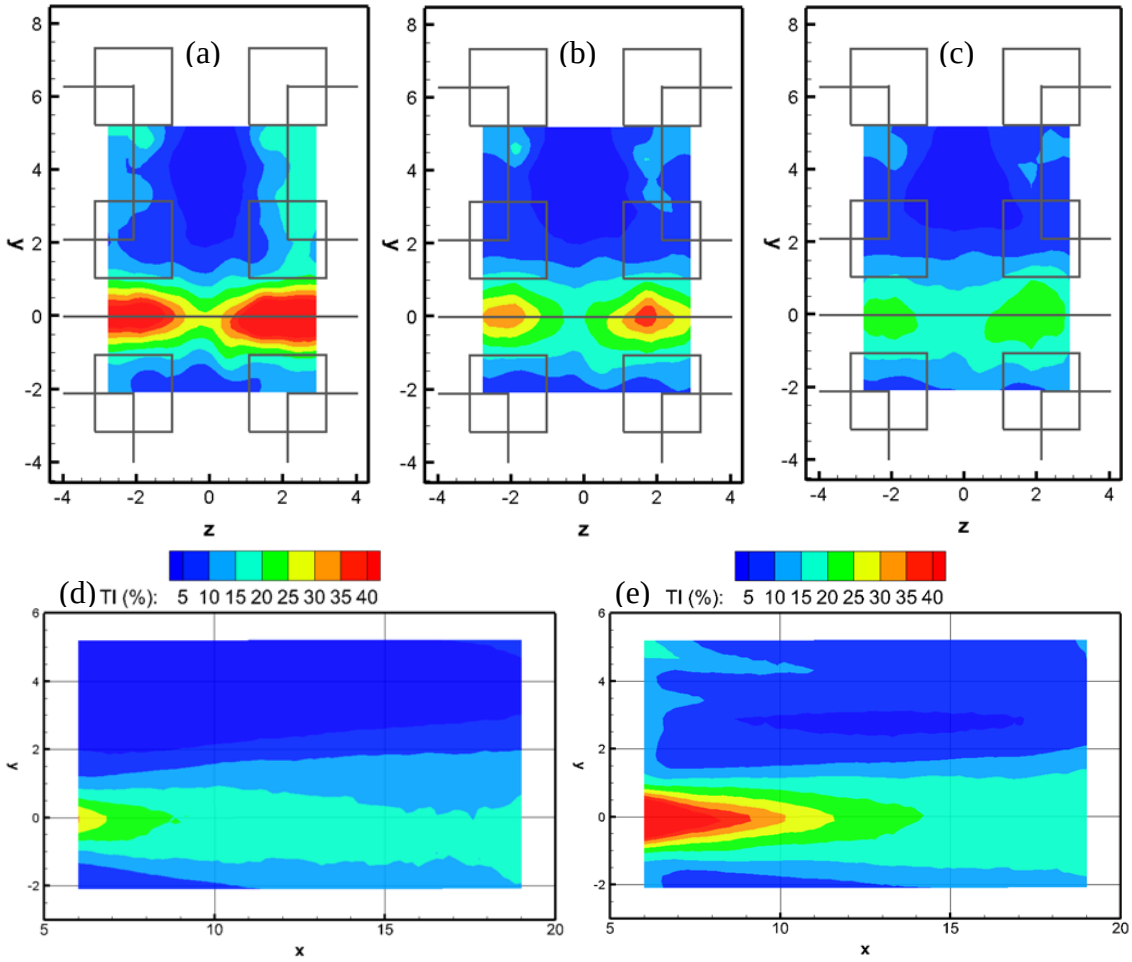

Figure A-7: *TI* as percentage for FG105 at (a) x=6.5, (b) x=9, (c) x=12, (d) z=0, and (e) z=1.4

Appendix B: Bilinear Interpolation

Using bilinear interpolation of the SPIV data will more accurately resolve the MPSR that surrounds the copepod. Copepods are typically around 1mm in length while the outputted vectors with a 50% overlap are approximately 0.75mm apart. In addition, only the centroid location of the copepod is known, but the orientation is unknown. Therefore, using a bilinear interpolation of the four nearest fluid vectors where MPSR is calculated will more accurately represent the sensed MPSR of the copepod. As mentioned in Chapter 3, bilinear interpolation will smooth data. Figure B-1 has a diagram that shows the copepod centroid and four surrounding grid points where MPSR is known. Here x and y are the streamwise and wall-normal locations of the copepod, respectively. x_1 and x_2 are two streamwise positions of the MPSR quantities used for bilinear interpolation, while y_1 and y_2 are the two wall-normal positions.

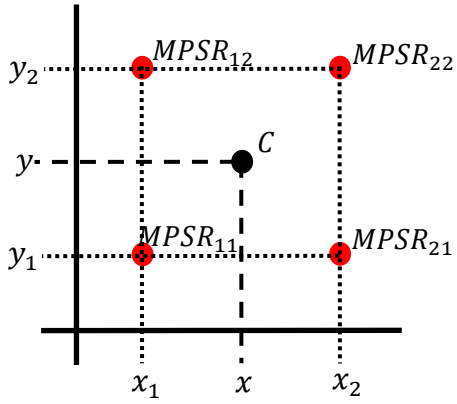

Figure B-1: Diagram of local vectors around copepod that are used to calculate the MPSR using a bilinear interpolation. C is the copepod centroid and $MPSR_{ii}$ is the location of the four surrounding vector locations where MPSR is known

Bilinear interpolation first approximates the desired quantity in one direction then resolves in the other direction. The final equation for the approximation is

$$MPSR(x,y) = \frac{1}{(x_2-x_1)(y_2-y_1)}[MPSR_{11}(x_2-x)(y_2-y) + MPSR_{21}(x-x_1)(y_2-y) + MPSR_{12}(x_2-x)(y-y_1) + MPSR_{22}(x-x_1)(y-y_1)]. \quad \text{(B-1)}$$

This will give a weighted result of $MPSR(x, y)$ depending on its location between x_1, x_2, y_1, and y_2.